SPACE SCIENCE AND ENGINEERING CENTER

UNIVERSITY of WISCONSIN – MADISON
1225 West Dayton Street
Madison, Wisconsin 53706-1695

23 February 1996

Dr. James J. DeCorpo
Scientific Officer, Code 32
Ballston Centre, Tower 1
Office of Naval Research
800 North Quincy Street
Arlington, VA 22217-5000

Re: N00014-90-J-4133 Final Report

Dear Dr. DeCorpo:

Enclosed are three copies of the final technical report for the referenced grant.

We apologize for the tardiness of this report. Thank you for your cooperation and assistance.

If you need additional information, please call me at 608-262-0985.

Sincerely,

John P. Roberts
Assistant Director

Enc: (3)

cc: Grants Officer, ONR
Director, NRL
DTIC
1192
144BX55
Dr. Eloranta

k:\admin\1192rpt.doc

Executive Director (608) 262-0544 Human Resources (608) 263-2348 Fax (608) 262-5974
Business Services (608) 263-3037 General Information (608) 263-6750 Telex 265452 UOFWISC MDS

Final report ONR Grant N00014-90-J-4133, "Collection of Statistics on the Frequency of Cloud Cover over North America"

This grant enabled us to complete work begun on ONR Grant N00014-87-K-0436 and to initiate a major upgrade to the University of Wisconsin High Spectral Resolution Lidar.

Two papers were presented at the 1991 Cloud Impacts on Defense Systems and Operations (CIDOS91) Conference. Abstracts of these papers: "The Three-Dimensional Spatial Structure of Cirrus Clouds Determined from Lidar and Satellite Observations" by E. Eloranta, D. Wylie and W. Wolf and "Measurement of Extinction Cross section by High Spectral Resolution Lidar" by C. Grund and E. Eloranta are included as part of this report. Final revisions on a paper published in Optical Engineering were completed under the support of this grant. This paper titled: "University of Wisconsin High Spectral Resolution Lidar" by C. Grund and E. Eloranta is also included in this report.

During November and December of 1991 the High Spectral Resolution Lidar (HSRL) was deployed as part of the FIRE cirrus experiment in Coffeyville, Kansas. In order to participate in this experiment it was necessary to convert the HSRL from a laboratory based instrument into a mobile semi-trailer mounted system. At the same time, a major redesign of the instrument was undertaken. The redesigned HSRL provides measurements of multiple scattering and depolarization in addition to the extinction and and backscatter cross section measurements made by the original instrument. In addition, the system sensitivity, the calibration accuracy and the operational reliability were improved. The HSRL redesign effort was initiated under the support of this grant. The new HSRL was described in a PHD thesis by Paivi Piironen. This thesis is included as part of this final report.

J:\home\johnr\msdoc\1192.doc

Final report ONR Grant N00014-90-J-4133, "Collection of Statistics on the Frequency of Cloud Cover over North America"

This grant enabled us to complete work begun on ONR Grant N00014-87-K-0436 and to initiate a major upgrade to the University of Wisconsin High Spectral Resolution Lidar.

Two papers were presented at the 1991 Cloud Impacts on Defense Systems and Operations (CIDOS91) Conference. Abstracts of these papers: "The Three-Dimensional Spatial Structure of Cirrus Clouds Determined from Lidar and Satellite Observations" by E. Eloranta, D. Wylie and W. Wolf and "Measurement of Extinction Cross section by High Spectral Resolution Lidar" by C. Grund and E. Eloranta are included as part of this report. Final revisions on a paper published in Optical Engineering were completed under the support of this grant. This paper titled: "University of Wisconsin High Spectral Resolution Lidar" by C. Grund and E. Eloranta is also included in this report.

During November and December of 1991 the High Spectral Resolution Lidar (HSRL) was deployed as part of the FIRE cirrus experiment in Coffeyville, Kansas. In order to participate in this experiment it was necessary to convert the HSRL from a laboratory based instrument into a mobile semi-trailer mounted system. At the same time, a major redesign of the instrument was undertaken. The redesigned HSRL provides measurements of multiple scattering and depolarization in addition to the extinction and and backscatter cross section measurements made by the original instrument. In addition, the system sensitivity, the calibration accuracy and the operational reliability were improved. The HSRL redesign effort was initiated under the support of this grant. The new HSRL was described in a PHD thesis by Paivi Piironen. This thesis is included as part of this final report.

J:\home\johnr\msdoc\1192.doc

The three-dimensional spatial structure of cirrus clouds determined from lidar and satellite observations.

E. W. Eloranta, D. Wylie, and W. Wolf

Cirrus cloud fields exhibit complex spatial structure; only infrequently does the standard homogenous plane-parallel description used by most modelers provide a reasonable picture of real cirrus structure. Simultaneous imagery from the University of Wisconsin Volume Imaging Lidar (VIL) and Meteorological Satellites have been used to quantify spatial structure of cirrus clouds. The VIL data includes 120 km by 220 km 3-dimensional maps of cirrus cloud fields with 60 m resolution. This data has been used to compute quantities such as the spatial distributions of cloud base altitude, cloud top altitude, and mid-cloud altitude. Two-dimensional autocorrelation functions describing the mean shape of cirrus clouds have been computed. Because cirrus clouds seldom have distinct edges, these correlation functions are derived as a function of a threshold value which defines the cloud edge.

The lidar data and ray tracing algorithms have also been used to synthesis images of the cirrus cloud fields as they would appear at a wavelength of 1.06 microns observed from the vantage point of the GOES satellite. These images will be presented and compared with the simultaneous GOES imagery.

The complex spatial organization of cirrus makes measurements of area-averaged mean cloud properties difficult with fixed location instrumentation. It also suggests that statistics on the occurrence of clear lines of sight through the cloud fields are difficult to collect. Figure 1 illustrates this problem using a top-down image of a cirrus cloud field derived from VIL data. This image depicts the cirrus cloud as a solid object with edges defined by a backscatter threshold value. Plotted on this image are a series of sloping lines; these show the path of clouds passing over 12 zenith-pointing sensors placed along a north south line at 10 km intervals. Numbers on the right of the plot show the one-hour-average percentage cloud cover in the first hour of the data period and those on the left show the one-hour-average for the second hour. Notice that during the first hour of observation one-hour-average cloud cover varies from 0 to 73%. Interestingly, the maximum cloud cover the minimum would be observed only 10 km apart. Even in the second hour of observation, where the average cloud cover has increased, the one-hour-average cloud cover varies from 36 to 87%.

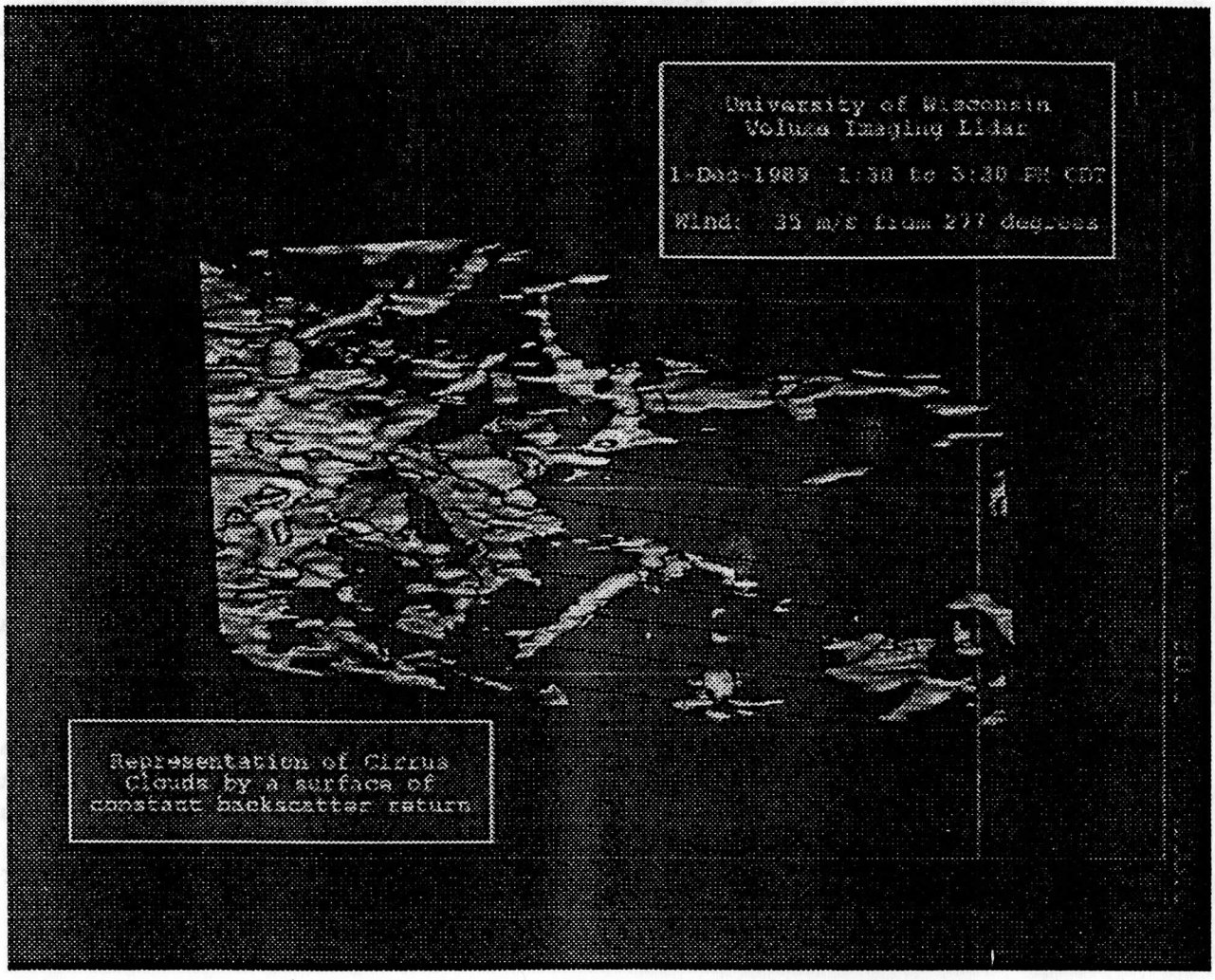

Figure 1:

A top-down view of the cirrus cloud field observed on Dec 1, 1989 with the Volume Imaging Lidar. The distance scale is given in kilometers. This image was constructed from two hours of VIL north-zenith-south image planes; the east-west dimension was constructed using loran-radiosonde winds. In the absence of temporal evolution of cloud elements this picture should be identical to a top-down picture of the cloud. The sloping black lines follow the cloud elements which would pass over 12 zenith-pointing radiometers placed at 10 km intervals along a north-south line. Figures at the right of the image represent the one-hour-average cloud cover seen by each radiometer in the first hour of observation and figures on the left for the second hour.

MEASUREMENT OF EXTINCTION CROSS SECTION BY HIGH SPECTRAL RESOLUTION LIDAR

Christian J. Grund and Edwin W. Eloranta

University of Wisconsin
Department of Meteorology
1225 W. Dayton St.
Madison, WI 53706

1. Introduction

At visible wavelengths, the distribution of extinction in the lower troposphere is primarily a function of aerosol loading and composition. Aerosols loosely include all non-gaseous matter present in the atmosphere, such as dust, cloud droplets, ice crystals, etc. Scattering and attenuation by aerosols largely determine atmospheric visibility (EPA, 1979). Adequate tools are needed for the long range, single ended assessment of visibility and for the identification of pollution sources.

In addition, attenuation and thermal emission from aerosols can either aid or hinder the operation of active and passive remote sensors. Measurements of aerosol optical properties are needed aid in the development and utilization of remote sensor systems.

Aerosols can also affect global and regional climates by altering the albedo of the atmosphere and modulating outgoing longwave radiation (Toon and Pollack, 1980). Measurements of the optical properties and distribution of naturally occurring and anthropogenic aerosols are needed to evaluate of the climate impacts of aerosols.

Because many aerosols contain hygroscopic salts, size distribution and composition can be strongly related to relative humidity. The optical properties of the aerosols can vary greatly depending on environmental conditions as well as upon local sources. Thus, it is difficult to obtain statistically valid samples of aerosol properties from surface based or airborne sensors. In situ samplers frequently require the rapid deceleration or acceleration of air samples through a detector chamber; both processes can alter the optical properties of the airborne aerosols. To overcome these difficulties, long path remote optical measurements are needed. Double ended systems have been used successfully but require careful field calibration; and, in many cases, only one end of the measurement range is accessible. Excellent spatial resolution and sensitivity suggest monostatic lidars as natural remote sensors for the assessment of visibility and the measurement of aerosol optical properties.

2. Background

Unfortunately, simple single channel lidars cannot produce unambiguous measurements of absolute scattering cross section or optical depth. These systems acquire only one measurement from each range, while the power received is a function of both the volume backscatter cross section and the optical depth between the lidar and the sensed volume. In tenuous media, single channel lidar backscatter measurements have been used to provide qualitative information about the structure and location of aerosol inhomogeneities. Tracking of aerosol inhomogeneities has been used to identify sources implicated in long range transport of pollutants. Aerosol backscatter structures have been tracked in time to provide measurements of turbulent velocities (Sroga and Eloranta, 1980) and have produced high quality spatially averaged measurements of mean winds (Hooper and Eloranta, 1986). As attenuation increases, correlating structural details in time series of single channel lidar backscatter profiles becomes more difficult.

Additional measurements or a priori knowledge of the scattering properties of the media must be available to independently establish the extinction and backscatter cross sections or to correct lidar profiles for attenuation. Bernoulli solutions to the lidar equation allow the determination of extinction cross section from single channel lidar data but require normalization by the extinction cross section somewhere within the profile (Klett, 1981) or by the optical depth across the measurement range (Weinman, 1987), and require an analytic form for the extinction to backscatter cross sections ratio (backscatter phase function). The extinction cross section and the optical depth are generally unknown, and the backscatter phase function depends in a complicated way on particle shape, size distribution, and composition which may vary spatially. These factors render direct application of Bernoulli solutions of uncertain value in most situations.

3. HSRL Instrumentation

The University of Wisconsin High Spectral Resolution Lidar (UW HSRL) has been specifically designed to overcome these ambiguities by interferometrically separating the backscatter return into a component due to aerosol scattering and a component due to scattering from air molecules. The molecular backscatter component is affected by extinction, but not by aerosol backscatter. Because the molecular backscatter cross section can be readily determined from a thermodynamic profile, the range derivative of the molecular backscatter signal is a direct and

unambiguous measure of the the aerosol extinction. The molecular backscatter cross section thus provides a known calibration target available at every range independent of the aerosol content of the atmosphere. The separation of aerosol from molecular scattering is possible because the backscatter component from air is Doppler-broadened by the thermal velocities of the molecules while the backscatter from more massive slower moving aerosols remains spectrally unbroadened. The UW HSRL produces direct measurements of cloud and aerosol optical depth, extinction cross section, backscatter cross section, and, when particle absorption is small, backscatter phase function. A brief description of the instrument will be given in our talk and a more complete description can be found in Grund and Eloranta (1991).

4. Data Examples and Discussion

For the past four years, the HSRL has been used extensively to measure the optical properties of cirrus clouds (Grund and Eloranta, 1991, Grund, et. al. 1990). Previous to the cirrus measurement activities, the HSRL had been employed to measure the aerosol extinction cross section and backscatter phase function in the lower atmosphere under a variety of conditions. The effects of relative humidity on aerosol optical properties had been observed during several experiments. For example, fig.'s 1 and 2 show humidigrams of aerosol extinction and backscatter phase function, respectively, for several summer, fall, and winter cases at Madison, WI. The data were acquired during late afternoon through early nighttime periods on days characterized by well mixed boundary layers. The apparent differences in optical property response to relative humidity suggest variations in the physical and chemical properties of the aerosols present on these days although changes in aerosol content due to advection cannot be rule out. The large variations in backscatter phase function observed on 1/4/84 evident in fig. 2 are coincident with the visual observation of freshly emitted coal burning heating plant smoke looping through the measurement range. Also note that on 10/4/84 very little change was observed in the backscatter phase function of the aerosols even though the relative humidity varied from 45% - 80% while the extinction cross section increased by a factor of ~4. On 8/28/84, the relative humidity and extinction cross section changes were similar to those observed on 1/4/84 while the backscatter cross section decreased by a factor of ~1.5. Fig. 3 shows the relationship between relative humidity and aerosol extinction cross section observed through a continuous evening-through-early-morning period. The hysteresis-like curve suggests the aerosols present on this day take up moisture more easily than they dry out.

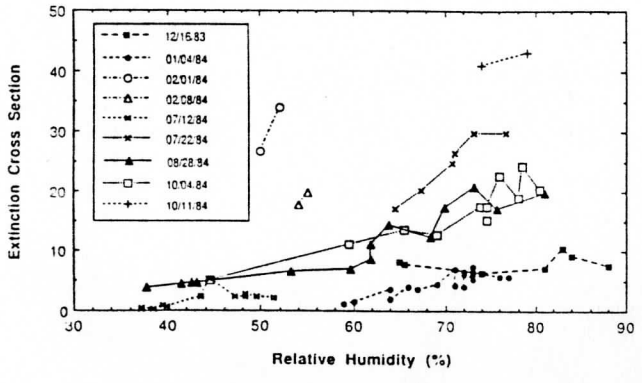

Fig. 1 Extinction cross section (10^{-5} m^{-1}) measured by the HSRL averaged over a ~2 km path and ~40 minutes as a function of relative humidity on the days indicated. Recent increases in transmitted power should decrease averaging requirements by ~10.

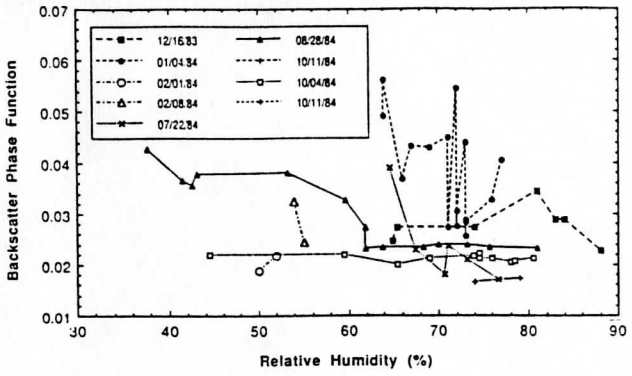

Fig. 2 Normalized backscatter phase function (sr^{-1}) measured by the HSRL averaged over ~2 km path and ~40 minutes as a function of relative humidity on the days indicated.

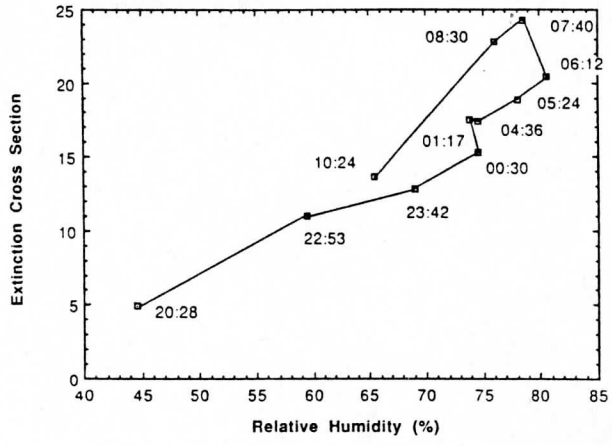

Fig. 3 Humidigram of aerosol extinction cross section (10^{-5} m^{-1}) acquired overnight within the same airmass suggesting these aerosols take up moisture more easily than they release it.

Statistical considerations required averaging times of ~40 minutes and an averaging range of ~2 km for these early measurements because of limited laser transmitter power. As a result, conclusions drawn from these data are subject to potential advection effects due to the limitations in time resolution. We have recently installed a new, more powerful laser transmitter (Grund and Eloranta, 1991) in the HSRL which has reduced time averaging requirements by a factor of ~10. It is expected that this transmitter will allow scanning of vertical slices within well-mixed cloud-capped boundary layers allowing observations of the relative humidity effects on aerosol optical properties while minimizing the influence of advected aerosols. In our talk, we will report on progress in these areas and on the HSRL capabilities as a remote optical property measurement system.

Acknowledgements. HSRL aerosol measurements reported here have been supported under ARO grant DAAG29-84-K-0069. Recent HSRL development and cirrus cloud measurements are supported under ONR contract N00014-87-K-0436.

6. References

EPA, 1979: Protecting Visibility: An EPA Report to Congress. EPA-450/5-79-008.

Grund, C.J., and E.W. Eloranta, 1990 : The 27-28 October 1986 FIRE IFO Cirrus Case Study: Cloud Optical Properties Determined by High Spectral Resolution Lidar. In pub. Nov. Mon. Weather Rev.

Grund, C.J., and E.W. Eloranta, 1991: The University of Wisconsin High Spectral Resolution Lidar. In pub. Jan. Optical Engineering.

Grund, C.J., S.A. Ackerman, E.W. Eloranta, R.O. Knutsen, H.E. Revercomb, W.L. Smith, and D.P. Wylie, 1990: Cirrus cloud characteristics derived from Volume Imaging Lidar, High Spectral Resolution Lidar, HIS radiometer, and satellite. preprints: 7th Conference on Atmospheric Radiation. AMS, 45 Beacon St., Boston, MA 02108, 357-362.

Hooper, W.P., and E.W. Eloranta, 1986: Lidar measurement of wind in the planetary boundary layer: The method, accuracy, and results from joint measurements with radiosonde and kytoon. J.Clim.Appl.Meteor. **25**, 991-1001.

Klett, J.D., 1981: Stable analytic inversion for processing lidar returns. Appl. Opt. **20**, 211-220.

Sroga, J.T., and E.W. Eloranta, 1980: Lidar measurement of wind velocity profiles in the boundary layer. J.Appl.Meteor. **19**, 598-605.

Toon, O.B., and J.B. Pollack, 1980: Atmospheric aerosols and climate. Amer. Scientist, **68**, 268-278.

Weinman, J.A., 1987: Derivation of atmospheric extinction profiles and wind speed over the ocean from a satellite-borne lidar. Appl.Opt. **27**, 3994-4001.

University of Wisconsin High Spectral Resolution Lidar

Christian J. Grund
Edwin W. Eloranta
University of Wisconsin
Department of Meteorology
1225 West Dayton Street
Madison, Wisconsin 53706

Abstract. The University of Wisconsin High Spectral Resolution Lidar (UW HSRL) produces direct measurements of cloud and aerosol optical depth, extinction cross section, backscatter cross section, and backscatter phase function. The HSRL uses a multietalon interferometer to separate the backscatter return into a component due to particle scattering and a component due to scattering from air molecules. The molecular backscatter component is affected by extinction but not by particle backscatter. Because the molecular backscatter cross section is determined by the known atmospheric density, the atmospheric extinction can be directly calculated from the measured decrease in molecular backscatter signal with range. The separation of aerosol from molecular scattering is possible because the backscatter component from air is Doppler-broadened by the thermal velocities of the molecules, while the backscatter from more massive, slower moving particles remains spectrally unbroadened. Although the HSRL was originally designed for airborne nadir observation of boundary layer aerosol optical properties, increases in transmitted power, receiver improvements, and modified calibration techniques have allowed it to measure cirrus cloud optical properties. A continuously pumped, Q-switched, 4 kHz pulse repetition frequency, injection seeded, frequency doubled Nd:YAG laser, still under development, has recently been installed and has reduced cirrus cloud measurement averaging times by a factor of ~10.

Subject terms: lidar; extinction cross section; backscatter phase function; cirrus cloud optical properties; aerosol optical properties; etalons; afterpulsing; continuously pumped seeded laser.

Optical Engineering 30(1), 6-12 (January 1991).

CONTENTS

1. INTRODUCTION

The power received by a monostatic lidar from each range is proportional to both the backscatter cross section of the scattering volume and the two-way path attenuation between the lidar and the backscattering volume. Thus, there is a fundamental ambiguity in the remote determination of absolute scattering cross section or optical depth by single-channel lidars; such systems can produce only one measurement of attenuated backscatter from each range. In tenuous media, lidar backscatter measurements can provide much information about the structure and location of clouds and aerosol inhomogeneities. As attenuation increases, interpreting structural details and locating cloud boundaries from single-channel lidar backscatter profiles becomes more difficult. Additional measurements or a priori knowledge of the scattering properties of the media must be available to independently establish the extinction and backscatter cross sections or to correct lidar profiles for attenuation. Bernoulli solutions to the lidar equation allow the determination of extinction cross section from single-channel lidar data but require normalization by the extinction cross section somewhere within the profile[1] or by the optical depth across the measurement range,[2] and require an analytic form for the extinction to backscatter cross section ratio (backscatter phase function). Unfortunately, the extinction cross section and the optical depth are generally unknown, and the backscatter phase function depends in a complicated way on particle shape, size distribution, composition, and orientation. These factors render direct application of Bernoulli solutions of uncertain value in most situations.

The University of Wisconsin High Spectral Resolution Lidar (HSRL) was specifically designed to overcome these ambiguities by interferometrically separating the backscatter return into a component due to particle scattering and a component due to scattering from air molecules. The molecular backscatter component is affected by extinction but not by particle backscatter. Because the molecular backscatter cross section is determined by the known atmospheric density, the atmospheric extinction can be calculated directly from the measured decrease in molecular backscatter signal with range. The molecular backscatter cross section thus provides a known calibration target available at every range, independent of the particle content of the atmosphere. The separation of aerosol from molecular scattering is possible because the backscatter component from air is Doppler-broadened by the thermal velocities of the molecules[3] while the backscatter from more massive, slower moving particles remains

Invited paper LI-102 received June 26, 1990; revised manuscript received Sept. 13, 1990; accepted for publication Sept. 17, 1990.

spectrally unbroadened. The HSRL produces direct measurements of cloud and aerosol optical depth, extinction cross section, backscatter cross section, and when particle absorption is small, backscatter phase function.

The HSRL was originally designed for airborne nadir observation of boundary layer aerosol optical properties.[4,5] The first HSRL transmitter used a nitrogen laser to pump a dye laser that developed ~1 mW at 467.8 nm with a 100 Hz pulse repetition frequency (PRF). Increased transmitted power and receiver improvements[6,7] have since enabled HSRL ground-based investigations of high altitude ice clouds (cirrus).[8] This configuration employed a CuCl laser that developed ~50 mW at 510.6 nm with an 8 kHz PRF, allowing eye-safe night and day measurements of boundary layer aerosol and cirrus cloud optical properties with ~15 min time resolution. Measurements of cirrus cloud optical properties are currently of great interest because these clouds strongly modulate atmospheric radiative properties, affecting both global climate and the operation of optical remote sensors. Measurements indicated that significantly improved time resolution was desirable for cirrus studies because the rapid variations in optical depth often observed in cirrus can lead to nonlinearities when averaging signals. Consequently, a continuously pumped, Q-switched, injection seeded, frequency doubled Nd:YAG laser has been installed and is under development in a joint effort with Quantronix Corp., Smithtown, N.Y. Increased power output and improved spectral and angular characteristics from the new transmitter have reduced cirrus cloud measurement averaging times to ~1 min (optical depth ~1, altitude ~8 km) while reducing calibration uncertainties. This paper presents the current UW HSRL instrument configuration, calibration and analysis techniques, and measurement capabilities.

2. HSRL THEORY

The basic principles inherent to all monostatic lidar systems are embodied in the lidar equation[9]:

$$P(R) = E_0 \xi R^{-2}\left[\beta_a(R)\frac{\mathbb{P}_a(\pi,R)}{4\pi} + \beta_m(R)\frac{\mathbb{P}_m(\pi)}{4\pi}\right] \times \exp\left[-2\int_0^R \beta_\varepsilon(r')dr'\right] + M(R) , \quad (1)$$

where $P(R)$ is the power incident on the receiver from range R, E_0 is the energy of the transmitted pulse, and $\xi = A_r c/2$, with A_r being the receiver area and c being the speed of light. The subscripts a and m denote aerosol and molecular scattering quantities. The term *aerosol* includes all particles (e.g., cloud droplets, ice crystals, dust, insects, hydrometeors) that by virtue of their mass have characteristic velocities that produce insignificant Doppler broadening of the scattered spectrum. $\beta_a(R)$ and $\beta_m(R)$ are the respective scattering cross sections per unit volume, $\mathbb{P}_a(\pi,R)/4\pi$ and $\mathbb{P}_m(\pi)/4\pi$ are the respective normalized backscatter phase functions, $\beta_\varepsilon(R)$ is the extinction cross section per unit volume, and $M(R)$ is the contribution from multiple scattering. The exponential term accounts for the two-way optical thickness between the lidar and the backscattering volume, where the optical thickness between range R_1 and R_2 is represented as

$$\tau = \int_{R_1}^{R_2} \beta_\varepsilon(r')dr' . \quad (2)$$

Equation (1) demonstrates that the lidar return depends on both the local value of the backscatter cross sections and on τ between the lidar and R. Only a single measurement of $P(R)$ is provided at each range by single-channel lidar systems, leading to ambiguities in the direct evaluation of either the backscatter or the extinction cross sections. It can be shown that there are an infinite family of $\beta_\varepsilon(R)$ profiles for which an increase in optical thickness with penetration depth is just canceled by an increase in backscatter with range, rendering the medium invisible to single-channel lidar systems of low sensitivity.[10]

In optically thicker media, the multiple scattering contribution $M(R)$ can further complicate matters by effectively increasing $P(R)$ in a way that depends on the unknown spatial distributions of the angular scattering phase function and optical thickness between the lidar and the sensed volume.[11] $M(R)$ can become large in distant returns from thick media but may be minimized by a narrow field of view (FOV) design for the lidar system. This solution is often difficult to achieve and is therefore not frequently implemented; however, a narrow FOV is a necessary requirement for the high resolution spectrometer employed in the HSRL. Thus, the uncertainties caused by the effects of multiple scattering processes are greatly reduced in the data acquired with this system.[7]

Because the HSRL separately measures molecular and particulate backscatter, two lidar equations may be written that are coupled by the common unknown integral of extinction. Assuming that $M(R)$ is negligible, the molecular and aerosol lidar equations may be written as

$$P_m(R)R^2 = E_0 \xi \beta_m(R)\frac{3}{8\pi}\exp\left[-2\int_0^R \beta_\varepsilon(r')dr'\right] , \quad (3)$$

$$P_a(R)R^2 = E_0 \xi \beta_a(R)\frac{\mathbb{P}_a(\pi,R)}{4\pi}\exp\left[-2\int_0^R \beta_\varepsilon(r')dr'\right] , \quad (4)$$

where the normalized molecular backscatter phase function $[\mathbb{P}_m(\pi)/4\pi]$ has been replaced with its analytic value, $3/8\pi$.

Because the molecular scattering cross section (β_m) is determined by the profile of atmospheric density calculated from radiosonde data (or from climatology), Eq. (3) is completely defined and may be solved explicitly for the extinction $\beta_\varepsilon(R)$ from the measured lidar return $P_m(R)$. The ambiguity in separating extinction from backscatter in single-channel lidar retrievals is eliminated by the HSRL technique since the system is effectively calibrated at each range with the return from the known molecular backscatter target.

The aerosol backscatter cross section is unambiguously determined from the ratio of Eq. (4) to Eq. (3):

$$\beta_a(R)\frac{\mathbb{P}_a(\pi,R)}{4\pi} = \beta_m(R)\frac{3}{8\pi}\frac{P_a(R)}{P_m(R)} . \quad (5)$$

By solving Eq. (3), the extinction cross section may be directly determined from the slope of the molecular backscatter return and a profile of molecular backscatter cross section calculated from the in situ density:

$$\beta_\varepsilon(R) = \frac{-1}{2}\left\{\frac{d\ln[P_m(R)R^2]}{dR} - \frac{d\ln[\beta_m(R)]}{dR}\right\} . \quad (6)$$

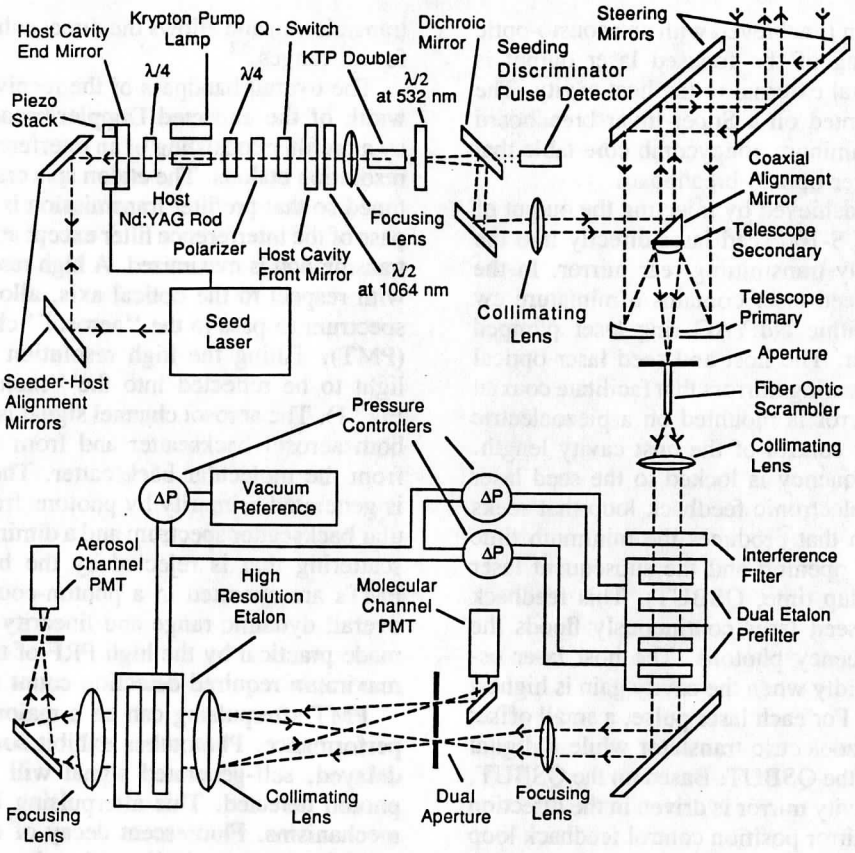

Fig. 1. HSRL transmitter/receiver.

Because the determination of $\beta_\varepsilon(R)$ from Eq. (6) depends on a derivative of measurements that are subject to noise, a finite difference formulation for the optical depth between two ranges (subscripted *1, 2*) is frequently employed:

$$\tau = \frac{1}{2}\ln\left[\frac{\beta_m(R_2)P_m(R_1)R_1^2}{\beta_m(R_1)P_m(R_2)R_2^2}\right]. \quad (7)$$

The width of the range interval required for a particular measurement is highly dependent on the signal amplitudes at each range and background light intensity. An analysis of the errors in optical depth measurements due to signal statistics may be found in Grund (1987).[7]

In the absence of aerosol and gaseous absorption, $\beta_a = \beta_\varepsilon - \beta_m$. Under these conditions, the normalized backscatter phase function is uniquely determined from Eq. (5) and the atmospheric density profile and is given by

$$\frac{\beta_a(\pi,R)}{4\pi} = \beta_m(R)\frac{3}{8\pi}\frac{P_a(R)}{[\beta_\varepsilon(R) - \beta_m(R)]P_m(R)}. \quad (8)$$

. HARDWARE IMPLEMENTATION

The HSRL transmitter employs an injection seeded, continuously pumped, Q-switched, frequency doubled, Nd:YAG laser operating at a 4 kHz PRF. The HSRL receiver spectrally separates the aerosol component from the molecular backscatter component using a pressure-tuned multietalon interferometer. The transmitter and receiver optic axes are coaxial and an alt-azimuth steering-mirror assembly allows computer-directed full sky coverage. Figure 1 shows the current system configuration and Table 1 outlines the current operating parameters.

Table 1. UW HSRL configuration.

Range Resolution:	Adjustable, 30 m - 135 m, by 15 m
Maximum Range:	256 X Range Resolution
Laser Wavelength:	532 nm (doubled Nd:YAG)
Pulse Repetition:	4 kHz
Pulse Width:	~130 ns
Transmitted Power:	~0.7 W average
Frequency Stabilization:	Injection seeding, <50 MHz/hr drift
Receiver Size:	0.35-m primary
Receiver Field of View:	320 μR
Receiver Bandwidth:	Aerosol channel: 0.5 pm (FWHM) Molecular channel: 2.5 pm (FWHM)
Detectors Used:	EMI 9863 B/100 PMT's
Signal Processing:	Photon counting
Computer:	LSI - 11/73
Plotting Format:	Real time, R^2 and log-corrected range-resolved A - Scope. Color enhanced time-height display.

3.1. Laser transmitter

The HSRL transmitter is presently based on a Quantronix model 116 laser modified by Quantronix to improve the mechanical and thermal stability of the cavity. A pressure regulator installed in the laser-head cooling water supply line reduces induced vibrations in the cavity, and augmented power supply filtering reduces krypton exciter lamp output fluctuations. Quarter-wave plates on either side of the Nd:YAG rod create counterrotating circular polarizations for waves traversing the cavity in opposing directions. This arrangement produces a smoother, more powerful output pulse by reducing the spatial hole burning associated with the formation of standing waves in TEM_{00} operation. High

repetition rate pulsed operation is achieved with an acousto-optic Q-switch. Frequency doubling of the focused laser output is accomplished by a KTP crystal external to the host cavity. The entire laser assembly is mounted on a Super-Invar breadboard supported by a 6 in. thick aluminum honeycomb core table that is comounted with the receiver optical breadboard.

Frequency stabilization is achieved by injecting the output of a modified Lightwave model S-100 seed laser directly into the host cavity through a partially transmitting rear mirror. In the standard configuration, the seed laser contains a miniature cw wavelength-stabilized monolithic Nd:YAG ring laser pumped continuously by a diode laser. The host and seed laser optical paths are linked by a pair of steering mirrors that facilitate coaxial alignment. The host rear mirror is mounted on a piezoelectric translator to allow electronic control of the host cavity length. The host cavity resonant frequency is locked to the seed laser oscillation frequency by an electronic feedback loop that seeks to maintain the cavity length that produces the minimum time delay between the Q-switch opening and the subsequent laser output pulse (Q-switch buildup time, QSBUT). This feedback scheme works because the seed laser continuously floods the host cavity with single-frequency photons. The host laser oscillation then builds most rapidly when the cavity gain is highest at the seed laser wavelength. For each laser pulse, a small offset voltage is applied to the piezoelectric translator while a digital circuit monitors the effect of the QSBUT. Based on the QSBUT, the average position of the cavity mirror is driven in the direction of minimum QSBUT. The mirror position control feedback loop has been modified from the standard configuration because the piezo stack cannot drive the mirrors at 4 kHz. A microprocessor-controlled feedback loop has been substituted for the original analog circuit to facilitate the independent control of loop parameters, the collection of QSBUT performance data, and the timely identification of unseeded pulses. The new controller also tracks slow drifts in the QSBUT due to pump lamp aging.

At present, QSBUT statistics are collected at the 4 kHz PRF but the mirror position is dithered at ~170 Hz. The observed difference in QSBUTs between seeded and unseeded conditions is typically ~200 ns and exhibits a strongly bimodal distribution. The observed average QSBUT is ~4.5 μs. In operation, spectral integrity of the received profiles is ensured by triggering the data system only for laser pulses that exhibit a QSBUT characteristic of the frequency locked condition. Recent counts of seeded pulses selected on the basis of QSBUTs over 100 s time intervals consistently suggest ~97% seeding efficiency. Spectral purity of these pulses has been verified by scans of the laser output accomplished with the HSRL receiver spectrometer.

3.2. Receiver

Backscattered light collected by the system telescope enters the receiver through a 1.23 mm core diameter, 100 mm long, rigid, step-index, 0.66 NA optical fiber. Both ends of the fiber are polished to ~1 wave and the fiber core is composed of MIL-G-174 type 620363 glass. With respect to the aperture positions of rays entering the fiber, internal reflections within the fiber spatially scramble the aperture positions of rays exiting the fiber. Ray position in the exit aperture of the fiber translates into ray angle after subsequent collimation. Thus, the ensemble of ray angles present in the collimated beam passing through the etalons is largely independent of the range from which the backscatter is received. This reduces the range dependence of the receiver spectrometer bandpass due to the angular sensitivity of etalon transmission and allows the direct calibration of the spectrometer for all ranges.[12]

The overall bandpass of the receiver is set to ~1.5 times the width of the expected Doppler-broadened molecular spectrum by a prefilter consisting of an interference filter and two moderate resolution etalons. The etalon spacers are chosen and the etalons tuned so that prefilter transmission is minimized aross the bandpass of the interference filter except at the laser wavelength where transmission is maximized. A high resolution etalon, tilted slightly with respect to the optical axis, allows the center of the return spectrum to pass to the "aerosol" channel photomultiplier tube (PMT). Tilting the high resolution etalon allows the rejected light to be reflected into the "molecular" channel PMT (see Fig. 1). The aerosol channel signal is generated by photons from both aerosol backscatter and from the center of the spectrum from the molecular backscatter. The molecular channel signal is generated primarily by photons from the wings of the molecular backscatter spectrum and a diminished component of aerosol scattering that is rejected by the high resolution etalon. The PMTs are operated in a photon-counting mode, yielding wide overall dynamic range and linearity. Operation in this mode is made practical by the high PRF of the laser, which reduces the maximum required detection count rate.

PMT afterpulsing can be a major limitation on lidar system performance. Phototubes exhibit some probability that a time-delayed, self-generated signal will be produced for each real photon detected. This afterpulsing is caused primarily by two mechanisms. Fluorescent decay of excited states in the photocathode occurs typically with a time constant shorter than 1 μs. Afterpulses can also be created when accelerated electrons dislodge ions from the anode, dynode chain, and support structures. Accelerating backward through the dynode chain, the ions dislodge additional electrons from the photocathode. Time constants for this mechanism are typically ~1 μs. The magnitude and time history of afterpulsing is highly dependent on tube construction. Because lidar signals decay rapidly, the integrated effect of afterpulsing from near-range returns can substantially disturb far-range measurements. It is possible to characterize the afterpulse distribution from each tube used and remove the effect by a deconvolution of the recorded signals[5]; however, this procedure mixes noise generated by large near-range returns with the weaker far-range signals.

Figure 2 shows the afterpulse probability distributions measured for one of the RCA C31024 PMTs used in the original system configuration and for one of the currently employed EMI 9863B/100 PMTs. The distributions were measured by averaging the PMT response to ~2×10^7 highly attenuated pulses from a CuCl laser (10 kHz PRF, 15 ns pulse width, 510.6 nm wavelength) as a function of time in 200 ns wide time intervals and smoothing the result. The mechanism for generating the secondary afterpulse at ~60 μs in the RCA tubes is not understood. The EMI tubes have significantly lower afterpulse probabilities and are currently used without correction.

4. TUNING AND CALIBRATION

The signals $S_a(R)$ and $S_m(R)$ observed from the atmosphere in the aerosol and molecular channels may be represented as follows:

$$S_a(R) = C_{aa}P_a(R) + C_{ma}(R)P_m(R) + B_a \,, \tag{9}$$

$$S_m(R) = C_{am}P_a(R) + C_{mm}(R)P_m(R) + B_m \,, \tag{10}$$

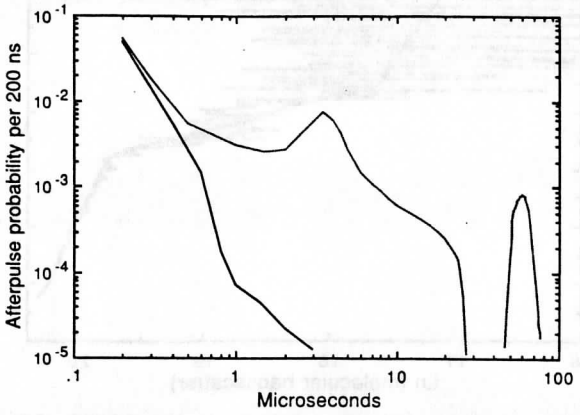

Fig. 2. Probability per photon count at 0 μs of observing a photomultiplier tube afterpulse (AP) per 200 ns interval. The distribution or one of the previously used RCA C31024 PMTs (dashed line) is ompared with one of the currently used EMI 9863B/100 PMTs (solid ine). The distributions were obtained by summing over ~2 × 10^7 highly attenuated pulses from a CuCl laser (10 kHz PRF, 15 ns pulse ·idth, 510.6 nm wavelength).

where B_a and B_m are the background light contributions measured in each channel, C_{aa} is the fraction of aerosol backscatter neasured in the aerosol channel, $C_{ma}(R)$ is the fraction of molecular backscatter measured in the aerosol channel, C_{am} is the fraction of aerosol backscatter measured in the molecular channel, and $C_{mm}(R)$ is the fraction of molecular backscatter measured in the molecular channel. C_{ma} and C_{mm} are functions of range because the width and shape of the molecular backscatter spectrum depends on the temperature and pressure of the scattering volume. Thus, after subtracting the background contributions, each channel observes a different linear combination of aerosol and molecular backscattered photons. In practice, the background contributions to each channel are estimated for every profile by observing the average signal level between 200 and 40 μs after the laser pulse.

Once mechanical alignment of the receiver optical elements has been performed, the spectral tuning and the determination of the calibration coefficients are accomplished by a fully automated procedure. Initially, the receiver aperture is filled with white light from an f/11 incandescent source. While holding the high resolution etalon chamber pressure fixed, the pressure in each prefilter etalon chamber is then scanned while observing the signal in the aerosol channel. Scans are performed alternately up and down in pressure to account for short time constant pressure sensor hysteresis. Each etalon is set to the average of the up and down scan pressures that produce the maximum signal responses. The procedure is iterated until convergence is achieved. This ensures the proper spectral alignment of the prefilter elements with the high resolution etalon.

Solving Eqs. (9) and (10) for $P_a(R)$ and $P_m(R)$ requires determination of the coefficients C_{aa}, C_{am}, $C_{mm}(R)$, and $C_{ma}(R)$. The coefficients are obtained by uniformly filling the receiver telescope with diffuse laser light while pressure scanning the receiver etalons across the laser output spectrum. To facilitate calibration scans, the system is constructed so that the prefilter etalon chamber pressures are slaved to the high resolution etalon chamber pressure. The high resolution etalon chamber pressure is referenced to a vacuum and set by the computer. Thus, coordinated spectral scans of the etalons only requires direct control of the high resolution etalon chamber pressure. The aerosol and molecular channel signals are normalized by the laser energy and recorded as a function of high resolution etalon pressure while scanning across the laser output spectrum. When the receiver bandpass is centered on the laser wavelength, coefficients C_{aa} and C_{am} are directly determined by the measured signal in the aerosol and molecular channels, respectively. C_{ma} and C_{mm} are determined from convolutions of the aerosol and molecular channel spectral scans with the expected spectral distribution of molecular backscatter calculated from a model that includes the effects of Brillouin scattering.[13] An extensive analysis of measurement sensitivity to errors in the determination of the calibration coefficients can be found in Grund (1984).[6]

To allow electronic rejection of unseeded pulses that would contaminate tuning and calibration scans, the laser output is delayed ~450 ns by a 100 m long solid core glass optical fiber before scattering into the receiver. This time delay is sufficient to allow comparison between the QSBUT and a threshold time between the known QSBUT's characteristic of seeded and unseeded laser operation. For calibration scans and atmospheric data acquisition, the receiver data system is triggered only on seeded-laser output pulses. When the calibration scan is complete, the high resolution etalon is returned to the pressure that produced the maximum response in the aerosol channel.

Ensuring that the transmitted laser beam is completely within the receiver field of view requires accurate alignment of the receiver and transmitter optic axes. This is accomplished by blocking the receiver at the collimating lens and jogging the transmitted beam into the receiver telescope with a high accuracy 5 in. aperture corner cube. The coaxial alignment mirror is then adjusted until the focused laser spot is centered on the fiber optic scrambler at the input aperture.

Because good separation of the aerosol and molecular scattering requires excellent knowledge of the bandpass shapes of the two channels, thermally induced spectral drift between etalons needs to be minimized. Therefore, the etalons are operated near the pressure that allows optical path length variations between the etalon plates, caused by density changes of the N_2 tuning gas, to cancel physical variations of the distance between the etalon plates, caused by fused silica spacer thermal expansion.[14] Further compensation for differential spectral drifts between etalons is accomplished by periodically filling the receiver aperture with laser light and then dithering the N_2 pressure in each etalon chamber while observing the ratio of aerosol to molecular channel signals. The pressure in each etalon is adjusted in the direction that produces the maximum ratio by an amount smaller than the dither width. This ensures the maximum rejection of the aerosol signal in the molecular channel. To account for small drifts in the etalon bandpass shape, a new set of calibration coefficients are derived for each lidar shot by synthesizing a new calibration scan from a wavelength-by-wavelength interpolation in time between calibration scans performed before and after data acquisition periods.

5. EXAMPLE

Figure 3 shows the backscatter cross section profile of a cirrus cloud observed by the HSRL. Note that the true backscatter cross section peaks near the cloud top at ~9 km. The backscatter cross section is produced from the ratio of the separated aerosol to molecular backscatter signals in accordance with Eq. (5). Figure 4 shows the R^2-corrected, attenuated backscatter profile of this cloud. The attenuated profile is plotted in arbitrary units and is similar to the signal profile that would be observed by a single-channel lidar. Note the apparent decrease in cloud scatter with altitude due to attenuation, which suggests that the cloud

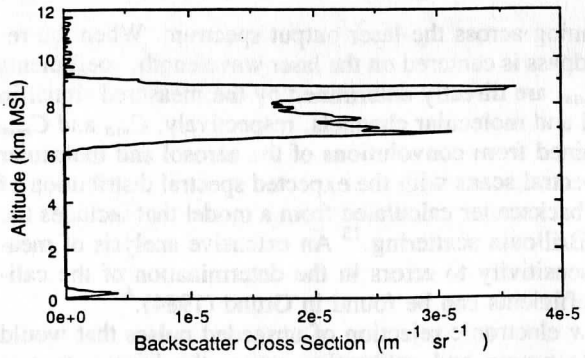

Fig. 3. Tropospheric aerosol backscatter cross section profile produced from a 10 min average of HSRL data acquired on Dec. 1, 1989. Boundary layer aerosol scattering can be seen below 1 km, and a cirrus cloud layer is present between 6 and 9 km. Note that the backscatter cross section peaks near the cloud top.

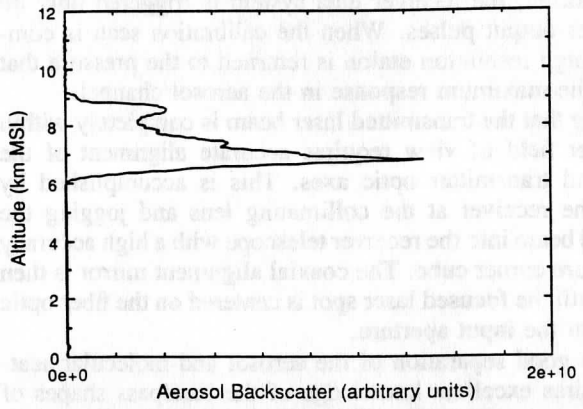

Fig. 4. Observed separated aerosol signal from which the Fig. 1 profile was generated. This is similar to the profile observed by a single-channel lidar. Without attenuation correction, the cloud appears to diminish with altitude.

is densest near the bottom. Figure 5 shows the natural log of the separated R^2-corrected molecular signal beyond the range at which the laser beam is completely within the receiver field of view. The decrease in signal with range is due both to the effects of decreasing molecular cross section with altitude and to particle and molecular extinction. Note that the molecular return drops off more rapidly within the cloud due to increased attenuation by the cloud.

The cloud optical depth is determined from the decrease in molecular signal across the cloud after compensating for the reduction in molecular backscatter cross section ($\tau \sim 1$ for this cloud). To mitigate noise, a best-fit line representing the expected signal calculated for an atmosphere free of particle scattering was calculated for the region just below and just above the cloud. Because cirrus cloud backscatter cross sections often exceed the molecular backscatter cross section ($\sim 7 \times 10^{-7}$ m^{-1} sr^{-1}) by several orders of magnitude, small crosstalk terms due to calibration uncertainties disturb the slope of the molecular backscatter profile. Consequently, the in-cloud region has been fitted with a profile derived from the known molecular backscatter cross section subject to a profile of extinction determined from a Bernoulli solution applied to the aerosol scattering profile (Fig. 4). The Bernoulli solution is an analytic solution to a differential form of the lidar equation. In this implementation, the measured optical depth is used as a constraint and a constant backscatter phase function with altitude is assumed. When the

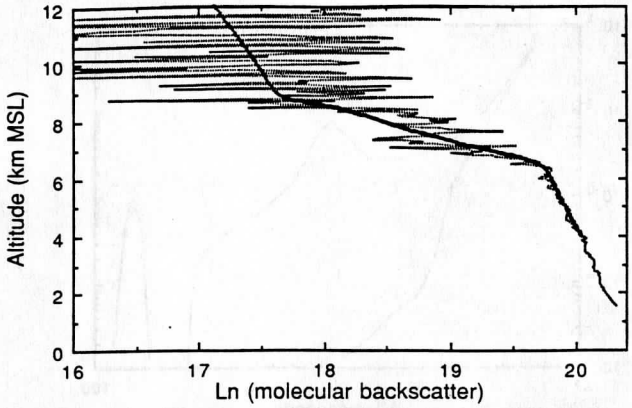

Fig. 5. Natural log of the molecular backscatter signal (dashed line) and best fit (solid line). Attenuation by the cloud causes the change in slope between 6 and 9 km altitude. The optical depth of this cloud was ~1 and the bulk backscatter phase function was ~0.048 sr^{-1}.

aerosol profile (Fig. 4) is divided by the best-fit molecular profile (Fig. 5) to produce the backscatter cross section (Fig. 3), the decrease in the molecular signal compensates for the loss of aerosol signal due to attenuation.

The bulk backscatter phase function indicated for this cloud by these measurements was 0.048 ± 0.015 sr^{-1} and the optical depth is 1.02 ± 0.24. The approximate extinction profile may be obtained from the backscatter cross section profile given in Fig. 3 by dividing the backscatter cross section values by the backscatter phase function, subject to the assumptions outlined above. Other measurements have yielded cirrus cloud backscatter phase functions between ~0.015 sr^{-1} and ~0.08 sr^{-1} and optical depths from <0.01 to greater than 2.7 (the approximate cloud penetration limit of the current system).[15]

It is important to note that the Bernoulli solution technique implemented here differs significantly from the more common single-channel inversion techniques because the solution is constrained by the simultaneously measured optical depth across the cloud. Although the large cloud backscatter signal causes some crosstalk in the molecular profile, background aerosol signals above and below the cloud tend to be of the order of or smaller than the molecular signals. Hence, suppression of the aerosol signal in the molecular channel outside the cloud provides essentially undisturbed estimates of the optical depth measured by this technique. Crosstalk performance improves in the lower troposphere, where ambient aerosols typically produce backscatter signals on the order of the molecular signals but the warmer temperatures cause a widening of the Doppler-broadened molecular spectrum. The crosstalk can be estimated from the ratio of the molecular profile signal perturbation in the cloud (see Fig. 5) to the aerosol signal at the same altitude shown in Fig. 4. At 8 km, for instance, this method would indicate ~1.5% residual crosstalk.

6. FUTURE DEVELOPMENTS

The system is currently undergoing reconfiguration for installation in a field deployable semitrailer. These modifications will include increasing the input aperture with a 20 in. diameter telescope and a simplified optical train to improve throughput. The etalons will be remounted in a temperature-stabilized chamber that should provide further reduction in the drift between received and transmitted wavelength.

Work is progressing on improving the laser seeding efficiency by optimizing the feedback loop parameters to correct for higher

frequency cavity vibrations. Casual experiments also suggest that further damping of flow irregularities in the primary cooling water will result in substantial improvements in seeding.

7. ACKNOWLEDGMENTS

Funding for the HSRL development, and cirrus data acquisition were provided under Army Research Office grant DAAG29-84-K-0069 and Office of Naval Research contract N00014-87-K-0436. Recent HSRL algorithm development and the incorporation of Brillouin scattering corrections in the molecular scattering model used to calibrate these data were funded under Air Force Geophysics Laboratory contract F19628-87-0056.

8. REFERENCES

1. J. D. Klett, "Stable analytical inversion solution for processing lidar returns," Appl. Opt. 20, 211–220 (1981).
2. J. A. Weinman, "Derivation of atmospheric profiles and wind speed over the ocean from a satellite-borne lidar," Appl. Opt. 27, 3994–4001 (1987).
3. G. Fiocco and D. B. DeWolf, "Frequency spectrum of laser echoes from atmospheric constituents and the determination of the aerosol content of the air," J. Atmos. Sci. 25, 488–496 (1968).
4. S. T. Shipley, D. H. Tracy, E. W. Eloranta, J. T. Sroga, F. L. Roesler, and J. A. Weinman, "High spectral resolution lidar to measure optical scattering properties of atmospheric aerosols. 1: theory and instrumentation," Appl. Opt. 22, 3716–3724 (1983).
5. J. T. Sroga, E. W. Eloranta, S. T. Shipley, F. L. Roesler, and P. J. Tryon, "High spectral resolution lidar to measure optical scattering properties of atmospheric aerosols. 2: calibration and data analysis," Appl. Opt. 22, 3725–3732 (1983).
6. C. J. Grund, "Application of the HSRL model II to measurements of aerosol backscatter phase function and cross section," MS thesis, Univ. of Wisconsin, Dept. of Meteorology (1984).
7. C. J. Grund, "Measurement of cirrus cloud optical properties by high spectral resolution lidar," Ph.D. thesis, Univ. of Wisconsin-Madison, Dept. of Meteorology, Abst. Inter. 48(5), Sec. B, Ord. No. ADG87-13152 (1987).
8. C. J. Grund, and E. W. Eloranta, "The 27-28 October 1986 FIRE IFO cirrus case study: cloud optical properties determined by high spectral resolution lidar," Mon. Wea. Rev. 118, 2344–2355 (1990).
9. R. T. H. Collis, and P. B. Russell, "Lidar measurement of particles and gases by elastic backscattering and differential absorption," in *Laser Monitoring of the Atmosphere*, E. D. Hinkley, ed., pp. 71–151, Springer-Verlag, New York (1976).
10. C. J. Grund and E. W. Eloranta, "Optically significant cirrus clouds may be rendered 'invisible' to space-borne simple lidar systems," OSA Tech. Dig. Series 18, 75–78 (1987).
11. E. W. Eloranta and S. T. Shipley, "Solution for multiple scattering," in *Atmospheric Aerosols: Their Formation, Optical Properties and Effects*, A. Deepak, ed., pp. 227–237, Spectrum Press (1982).
12. C. J. Grund and E. W. Eloranta, "Fiber optic scrambler reduces the bandpass range dependence of Fabry-Perot etalons used for spectral analysis of lidar backscatter," Appl. Opt., submitted (1990).
13. S. Yip and M. Nelkin, "Application of time-dependent density correlations in fluids," Phys. Rev. 135, A1241–A1247 (1964).
14. C. J. Grund, F. L. Roesler, and E. W. Eloranta, "Thermally induced spectral drift cancellation in pressure-tuned Fabry-Perot etalons," Appl. Opt. 27, 662–663 (1988).
15. C. J. Grund, S. A. Ackerman, E. W. Eloranta, R. O. Knutsen, H. E. Revercomb, W. L. Smith, and D. P. Wylie, "Cirrus cloud characteristics derived from volume imaging lidar, high spectral resolution lidar, HIS radiometer, and satellite," in *7th Conf. on Atmospheric Radiation*, pp. 357–362, Am. Meteorological Soc., 45 Beacon St., Boston, MA 02108 (1990).

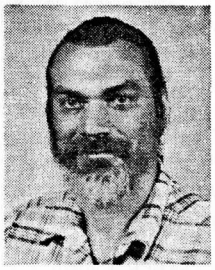

Chris Grund graduated summa cum laude with a BS degree in meteorology from the City College of New York in 1981 and earned both his MS (1984) and Ph.D. (1987) degrees in meteorology from the University of Wisconsin–Madison. He is currently an assistant scientist with the University of Wisconsin, where his work and research interests include the development of lidar systems, the measurement of atmospheric aerosol and cirrus cloud optical properties by lidar, and the application of active and passive remote sensing techniques to atmospheric measurements. As an independent electronics consultant during the past 15 years, he has been granted 12 patents and has developed a variety of electronic devices ranging from watches and games to remote detection security systems and a speaking bar code reader.

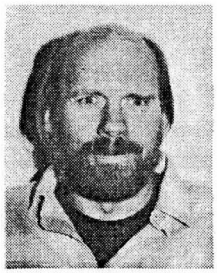

Ed Eloranta received his BA degree in physics in 1965 and his MS (1967) and Ph.D. (1972) degrees in meteorology, all from the University of Wisconsin–Madison. He is currently a senior scientist at the University of Wisconsin, where he directs a research group developing lidar systems and lidar data analysis techniques for atmospheric studies. Current research includes the extraction of meteorological information from three-dimensional lidar images of atmospheric boundary layers and clouds. Additional projects involve the measurement of cirrus cloud optical properties for climate studies.

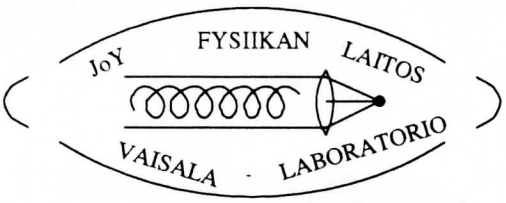

UNIVERSITY OF JOENSUU
DEPARTMENT OF PHYSICS
VAISALA LABORATORY

DISSERTATIONS 6

A HIGH SPECTRAL RESOLUTION LIDAR BASED ON AN IODINE ABSORPTION FILTER

PAIVI PIIRONEN

Joensuu 1994

UNIVERSITY OF JOENSUU
DEPARTMENT OF PHYSICS
VAISALA LABORATORY

DISSERTATIONS 6

A High Spectral Resolution Lidar Based on Absorption Filter

Paivi Piironen

ACADEMIC DISSERTATION

To be present, with the permission of the Faculty of Science of the University of Joensuu, for public criticism in Auditorium P1 of the University of Joensuu, Tulliportinkatu 1, Joensuu, on October 14th, 1994, at 12 noon.

JOENSUU 1994

Julkaisija
Publisher
Joensuun yliopisto
University of Joensuu

Toimittaja
Editor
FT Timo Jaaskelainen

Exchange
Joensuu University Library, exchange
P.O.Box 107, FIN-80101 JOENSUU, FINLAND
Fax: +358-73-151-2691

Sale
Joensuu University Library, sale of publications
P.O.Box 107, FIN-80101 JOENSUU, FINLAND
Fax: _358-73-151-2691
Email: lavikainen@joyl.joensuu.fi

UDK 535.2:551.510.4:551.508.5
ISSN 1236-4673
ISBN 951-708-268-1

Original print by: Joensuun yliopiston monistuskeskus 1994

Päivi Piironen
University of Wisconsin–Madison
Space Science and Engineering Center
1225 West Dayton Street
Madison, WI 53706, USA

Keywords: High Spectral Resolution Lidar, lidar, iodine absorption, optical parameters of atmosphere, error analysis

Abstract

A High Spectral Resolution Lidar (HSRL) that uses an iodine absorption filter and a tunable, narrow-bandwidth Nd:YAG laser is demonstrated. The iodine absorption filter provides better performance than the Fabry-Perot etalon that it replaces. This study presents an instrument design that can be used as a basis for a design of simple and robust lidar for the measurements of the optical properties of the atmosphere. The HSRL provides calibrated measurements of the optical properties of the atmospheric aerosols. These observations include measurements of aerosol backscatter cross section, optical depth, backscatter phase function, depolarization, and multiple scattering. The errors in the HSRL data are discussed and the effects of different errors on the measured optical parameters are shown.

Contents

1 Introduction

The climate models used for modeling the transport of the short and longwave radiation in the atmosphere require a knowledge of the aerosol and cloud optical properties. Because the optical properties of cirrus clouds are not well known, the measurements of cloud optical depth, phase function, and particle size provide important information. Clouds affect the radiative balance of the earth and its atmosphere by reflecting incoming solar radiation and trapping outgoing longwave radiation. Cirrus clouds have been found to have an important role on this process[1,2]. Cirrus clouds consist of large, nonspherical ice crystals and they are generally found between altitudes of 4 and 15 km. Compared to water clouds, cirrus clouds are generally optically thin. Studies based on climate models suggest that presence of cirrus may produce either a heating or cooling effect depending on the cloud optical properties and altitude[1,2].

The University of Wisconsin High Spectral Resolution Lidar (HSRL) measures optical properties of the atmosphere by separating the Doppler-broadened molecular backscatter return from the unbroadened aerosol return. The molecular signal is then used as a calibration target which is available at each point in the lidar profile. This calibration allows unambiguous measurements of aerosol scattering cross section, optical depth, and backscatter phase function. Also measurements of depolarization and multiple scattering can be performed. In this study, clear air aerosols, stratospheric aerosols, and cloud particles are all referred to as aerosols. Similar measurements of cloud optical parameters can be made with a Raman-lidar[3,4], but because the Raman backscatter cross section is about 1000 times smaller than the Rayleigh backscatter cross section, the HSRL has a significant signal strength advantage over the Raman-technique. Another advantage of the HSRL is that it can provide daytime measurements while sky noise background limits the measurements of the weak Raman signal to night time.

The basic idea of an HSRL was originally presented by Fiocco and DeWolf[5]. They proposed the measurements of atmospheric aerosols by interferometrically separating the backscatter signal. They demonstrated the principle of an HSRL with laboratory measurements of scattering from natural aerosols and artificially produced dense fog. A later experiment with the HSRL technique was performed by Schwiesow

and Lading[6], who used Michelson interferometers in an attempt to measure atmospheric temperature. Their evaluation showed that a Michelson interferometer based measurements would theoretically produce accurate measurements of atmospheric temperature, but development of a functional system was limited by the quality of available optical components.

An investigation done by Shipley *et al.*[7] for a shuttle borne lidar experiment to measure global distribution of aerosols and their effects on the atmospheric heat budget started the University of Wisconsin HSRL research. The demonstration of the first University of Wisconsin HSRL was published by Shipley *et al.*[8]. The paper by Sroga *et al.*[9] presented the first results measured with the same system. The transmitter was based on a dye laser that operated at 476.8 nm wavelength. This laser provided only a 2–4 mW output and it operated at 100 Hz repetition rate. The backscatter signal was collected by a 0.35 telescope with a 320 μrad receiver field of view. The filtering of the solar background was performed by using an interference filter and three low resolution etalons with a total bandpass of 2 pm. The separation between aerosol and molecular backscatter signals was based on a high resolution etalon with $\sim$ 0.5 pm bandpass. The HSRL was mounted in an aircraft. The system pointed down to ground and it therefore covered only about 2 km measurement range. The range dependence of the receiver spectrometer bandpass due to the angular sensitivity of the etalon transmission complicated the measurements.

The aircraft system was later modified for ground based operations and the changes were reported by Grund[10]. The problems due to the range dependence of the spectrometer bandpass were reduced by using a fiber optics scrambler[12]. The transmitter laser was changed to a CuCl laser operating at 510.6 nm wavelength. The laser output power was 50 mW at 8 kHz repetition rate. The receiver telescope and the high resolution etalon remained the same, but the number of low resolution etalons was decreased to two providing a 2.5 pm bandpass. This system was capable of measuring cirrus cloud optical parameters up to $\sim$ 12 km altitude. Later, the development of lasers enabled the use of an injection seeded, frequency doubled Nd:YAG-laser (532 nm) as the HSRL transmitter. The new laser provided a 0.7 W output at 4 KHz repetition rate. This change was reported by Grund and Eloranta[11].

After all the development in the HSRL, problems with the insufficient calibration accuracy and environmental sensitivity of the system operation remained. The HSRL produced accurate measurements of clear air and thin cirrus, but the measurement accuracy was not sufficient for the cases where the aerosol signal was large compared to the molecular signal. Eventhough the measurement accuracy was not high enough to provide direct measurements of the optical depth profile inside a cloud, the total cloud optical depth was obtained. The cloud optical depth was determined from the decrease in the molecular signal across the cloud. The calculations of optical depth profile inside a cloud were made by assuming a constant backscatter phase function with altitude. The measured molecular profile was fitted with a profile derived from the known molecular backscatter cross section that had been corrected for the atmospheric extinction. The extinction profile was obtained by applying the Bernoulli solution to the aerosol backscatter profile[12]. The measured optical depth was used as a constraint.

The accuracy of the HSRL calibration was improved and the sensitivity for environmental changes was reduced in the next University of Wisconsin HSRL (Eloranta and Piironen[13]). In order to make the system operation more stable, the system was moved to a temperature controlled and vibrationally isolated environment. Participation in field experiments was made possible by moving the lidar to a semitrailer. The diameter of the receiver telescope was increased to a 0.5 m and the field of view was decreased to 160 μrad. A new photon counting data system was designed and extensive computer control of the system operations was implemented. Depolarization and multiple scattering measurement capabilities were added. With the improved system, the measurements of cloud optical properties were performed at altitudes up to $\sim$ 30 km.

During the 18 first years of the University of Wisconsin HSRL, the separation between aerosol and molecular scattering was based on a Fabry-Perot etalon with a 0.5 pm bandpass. With this etalon, the signal was divided into two channels. The signal reflected from the etalon surface was measured with one channel. This channel contained the the wings of the molecular spectrum and the part of the aerosol spectrum that did not pass the high resolution etalon. The other channel was used to measure

the part of the aerosol spectrum and the central part of the molecular spectrum that transmitted through the etalon. The basic idea of the spectral separation of a high resolution etalon based HSRL is presented in Fig 1.

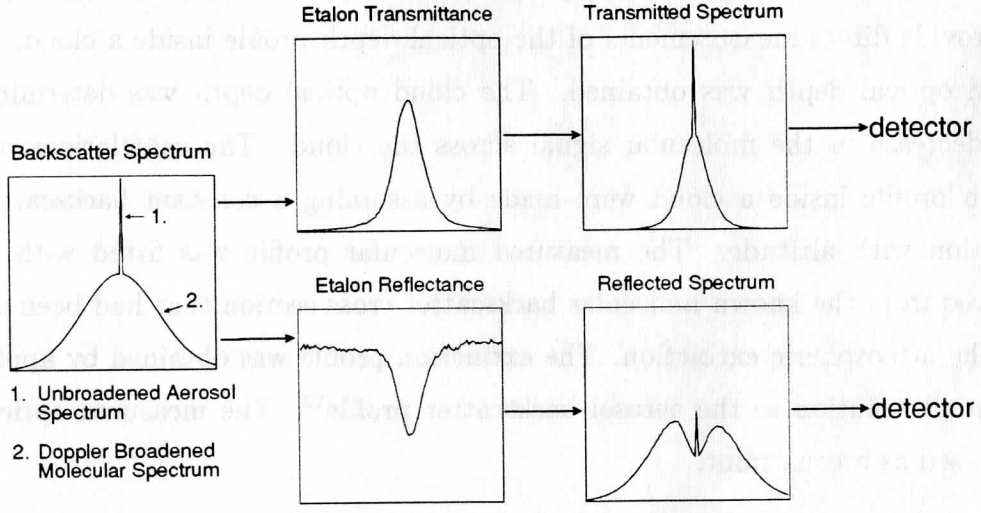

Figure 1. The spectral response of a high resolution etalon based HSRL. The received signal is a combination of the Doppler-broadened molecular backscatter spectrum and the unbroadened aerosol spectrum. The aerosol signal and the center of the molecular signal that transmits through the etalon is detected with one channel. The other channel detects the signal reflected from the etalon.

For the aerosol backscatter signal, only a $\sim$ 2:1 separation ratio between aerosol and molecular channel is achieved by a etalon. The Fabry-Perot etalon based HSRL produces accurate measurements of clear air, thin cirrus, and stratospheric aerosols. However, when the system is used to probe dense water clouds, the aerosol signal becomes on the order of 10^3 larger than the molecular return. Therefore, the inversion coefficients used to separate the aerosol and molecular signals must be known with better than 0.01% accuracy or otherwise some of the aerosol return will appear in the separated molecular return. Since the inversion coefficients for the etalon based system are known with only $\sim$ 0.1% accuracy, the measurements of dense water clouds are subject to error. The performance of a Fabry-Perot etalon is limited by its finesse and the angular distribution of incoming light. The etalon must be operated in pressure and temperature controlled environment, since better than a 0.1 mbar

pressure tuning accuracy and 0.1 °C temperature stability are required to keep the filter performance stable.

Shimizu *et al.*[14] proposed the use of an narrow-band atomic absorption filter in an HSRL and She *et al.*[15] reported high spectral resolution lidar measurements of temperature and aerosol extinction coefficient made by using a barium atomic absorption filter. These studies, and later studies from the same group[16,17], have shown, that an absorption filter provides a high rejection against aerosol scattering and therefore it makes the separation between molecular and aerosol scattering easier. Another advantage of an absorption filter is the stability of the absorption characteristics[14]. Furthermore, the transmission characteristics of an absorption filter are not dependent on the mechanical alignment of the filter[14] or the angular dependence of the incoming light. Also, a wide dynamic range in rejection against aerosol scattering is achieved by simply changing the vapor pressure[14] or the length of the cell.

This study presents an HSRL employing an iodine absorption filter. The spectrum of the $B^3\Pi^+_{ou} \rightarrow X^1\Sigma^+_g$ electronic transition in molecular iodine has more than 22 000 absorption lines in the visible wavelengths[18], and 8 of them are easily reached by thermally tuning a frequency doubled Nd:YAG laser output[19]. Compared to the barium, the advantage of iodine is that instead of requiring a dye laser, a narrow bandwidth, frequency doubled Nd:YAG laser can be used. Also, a strong absorption is obtained in a short cell at room temperature. Even though iodine has extensive hyperfine structure, the absorption line width is similar to the barium line width, which is broadened by operating at a temperature of ~500 °C.

A large number of iodine absorption lines have been used as reference for Doppler-limited spectroscopy studies and also numerous spectroscopic studies of the line structure and hyperfine structure have been performed. Liao and Gupta[20] reported a use of an iodine absorption vapor cell as a narrow band filter for fluorescence spectroscopy. Lately Miles *et al.*[21] reported the measurements of flow field properties based on an iodine absorption filter and Filtered Rayleigh Scattering technique. The first iodine absorption filter based HSRL is presented here.

The basic idea of an iodine absorption filter based HSRL is presented in Figure 2. The received backscatter signal is divided to two channels. One channel detecting

a sample from the total backscatter spectrum and the other channel the spectrum filtered by the iodine absorption filter. This signal contains information about the wings of the molecular spectrum and a small aerosol cross-talk signal. The first measurements made with the iodine absorption based HSRL were presented by Piironen and Eloranta[22].

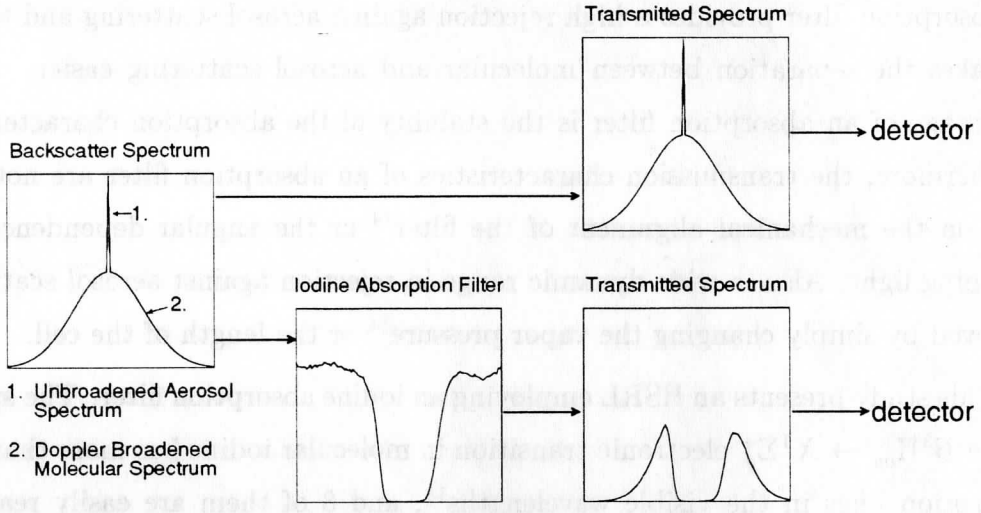

Figure 2. The spectral response of an iodine absorption filter based HSRL. The detected backscatter spectrum is divided to two channels. One containing the information from the total backscatter spectrum and the other the wings of the molecular spectrum and a small aerosol cross-talk.

The work presented in this thesis is organized as follows. A short introduction to the HSRL theory is given in Chapter 2. After that, the instrumentation of the new iodine absorption based HSRL is given in Chapter 3. This chapter also presents the basic principles of the polarization and multiple scattering measurements. A more detailed description of the iodine absorption cell is given in Chapter 4. The system calibration and laser wavelength locking are discussed in Chapter 5. In Chapter 6, examples from the data obtained with the new HSRL are given. This chapter gives a more detailed description of the depolarization measurements and also shows the effects of multiple scattering on the measured depolarization ratio. In addition to the depolarization measurements, the measurements of scattering ratio, aerosol backscatter cross section, and optical depth are discussed. The measurements show, that the

use of an iodine absorption filter enables accurate measurements of cloud optical parameters. Because the cross talk between channels can be accurately corrected and because the 160 μrad field of view of the HSRL effectively suppresses multiple scattering, the optical depth inside a cloud can be measured. This makes future studies of scattering phase function possible. As a final example from the HSRL measurements the Chapter 6 shows an atmospheric temperature profile obtained by the HSRL. The accuracy of the HSRL measurements is discussed in Chapter 7 and the error analysis is presented.

2 Lidar theory of the HSRL

The lidar equation of a monostatic lidar system can be presented in the following form

$$N(R) = \frac{N_o}{R^2}\frac{cA}{2}[\beta_a(R)\frac{P_a(\pi,R)}{4\pi} + \beta_m(R)\frac{P_m(\pi,R)}{4\pi}]e^{-2\tau(R)} + M(R) + B, \quad (1)$$

where

$N(R)$	= number of photons incident on the receiver field of view from range R per data bin length,
N_o	= number of transmitted photons,
c	= speed of light,
A	= area of the receiver telescope,
$\beta_a(R), \beta_m(R)$	= aerosol and molecular scattering cross sections per unit volume, respectively,
$\frac{P_a(\pi,R)}{4\pi}, \frac{P_m(\pi,R)}{4\pi}$	= normalized backscatter phase function due to aerosol and molecular scattering, respectively,
$\tau(R)$	= one way optical depth between lidar and backscatter volume at range R, $= \int_0^R \beta_\epsilon(r')dr'$, where $\beta_\epsilon(R)$ = total extinction cross section per unit volume,
$M(R)$	= multiple scattering contribution incident on the receiver per data bin length,
B	= number of background photons incident on the receiver per data bin length.

Equation (1) demonstrates that the lidar return depends on both the local value of the backscatter cross section and on the optical depth between the lidar and backscattering volume at range R. A conventional single channel lidar provides a single measurement of N(R) at each range, and therefore it does not provide enough information to solve the lidar equation for extinction or backscatter cross section. The knowledge about the relationship between the backscatter cross section and extinction has to

be known or assumed and an estimate of a boundary value has to be given (see for example Klett[23]).

In order to make measurements of extinction and backscatter cross section, the HSRL measures two signals which can be processed to present lidar returns from aerosol and molecule backscattering. The separation between the aerosol and molecular scattering is possible, because the signal backscattered from air molecules is Doppler-broadened, while the signal from more massive, slowly moving aerosols remains spectrally unbroadened.

In the case of the HSRL, two separate lidar equations can be written

1) For aerosols

$$N_a(R) = F(R)\frac{N_o c A}{2R^2}\beta_a(R)\frac{P_a(\pi, R)}{4\pi}e^{-2\int_0^R \beta_\epsilon(r')dr'} \tag{2}$$

2) For molecules

$$N_m(R) = F(R)\frac{N_o c A}{2R^2}\beta_m(R)\frac{3}{8\pi}e^{-2\int_0^R \beta_\epsilon(r')dr'}, \tag{3}$$

The molecular backscatter phase function is here replaced with its analytical value $\frac{3}{8\pi}$. The term F(R) is an overlap term, that is a function of receiver and transmitter geometry[8]. Because the molecular scattering cross section is a function of the air density and can be calculated from the Rayleigh scattering theory using an independently measured atmospheric density profile, the equation (3) is well defined and it can be solved for the extinction. The molecular scattering cross section provides a calibration target which is available at each point of the lidar return.

Following optical parameters can be obtained from the separated lidar signals:

1) Aerosol to molecular backscatter ratio (scattering ratio) SR(R)

$$SR(R) = \frac{N_a(R)}{N_m(R)}. \tag{4}$$

Notice that, the backscatter ratio measurement is not dependent from the overlap term, and therefore measurements of backscatter ratio for the overlap region can be performed. The same effect can be seen later on the aerosol backscatter cross section and depolarization ratio determination.

2) Aerosol backscatter cross section

The properties of the molecular scattering are well known and therefore, the atmospheric density can be used to compute the molecular scattering cross section per unit volume β_m. From Rayleigh scattering theory[24], the molecular scattering cross section per unit volume is

$$\beta_m(R) = \mathcal{N}_m(R)\frac{d\sigma_R(\pi)}{d\Omega}, \tag{5}$$

where

$\mathcal{N}_m$ = number of gas molecules per unit volume

$\frac{d\sigma_R(\pi)}{d\Omega}$ = differential Rayleigh scattering cross section at scattering angle π per average gas molecule

For mixture of atmospheric gases below 100 km altitude[24],

$$\frac{d\sigma_R(\pi)}{d\Omega} = 5.45[\frac{\lambda(\mu m)}{0.55}]^{-4}10^{-28}cm^2sr^{-1}. \tag{6}$$

The number of gas molecules per unit volume can be calculated from the atmospheric pressure P(R) and temperature T(R).

$$\mathcal{N}_m(R) = \frac{P(R)}{T(R)}\frac{N_A}{R_a}, \tag{7}$$

where

P(R) = atmospheric pressure at range R

T(R) = atmospheric temperature at range R

N_A = Avogadro's number

R_a = gas constant of dry air

Thus, by using the previous equations, the molecular scattering cross section per unit volume can be written in the following form.

$$\beta_m = \frac{C_{air}P(R)}{T(R)}, \tag{8}$$

where

C_{air} $= 3.786 \times 10^{-8} KhPa^{-1}m^{-1}$ at 532 nm (from Eq. 5)

$P(R)$ = atmospheric pressure

$T(R)$ = atmospheric temperature

The aerosol backscatter cross section can be calculated by using the backscatter ratio and the calculated value of β_m

$$\beta_a(R)\frac{P_a(\pi,R)}{4\pi} = SR(R)\beta_m(R)\frac{3}{8\pi}. \tag{9}$$

3) The optical depth of a layer between ranges R_1 and R_2

$$\tau(R_2) - \tau(R_1) = \int_{R_1}^{R_2} \beta_\epsilon(r')dr' = \frac{1}{2} ln \left[\frac{\beta_m(R_2)}{\beta_m(R_1)}\frac{R_1^2}{R_2^2}\frac{N_m(R_1)}{N_m(R_2)}\frac{F(R_1)}{F(R_2)}\right]. \tag{10}$$

4) Total extinction cross section

The average value of total extinction cross section is a range derivative of the optical depth

$$< \beta_\epsilon > = < \frac{\partial \tau(R)}{\partial R} > = \frac{\tau(R_2) - \tau(R_1)}{R_2 - R_1}. \tag{11}$$

5) Backscatter phase function

The backscatter phase function, $\frac{P_a(\pi,R)}{4\pi}$, can be calculated from the following equation

$$\frac{P_a(\pi,R)}{4\pi}a(R) = \beta_m(R)\frac{3}{8\pi}\frac{SR(R)}{\beta_\epsilon(R)}, \tag{12}$$

where

$a(R)$ = single scattering albedo.

For water and ice clouds and most aerosols, the single scattering albedo at the wavelength of 532 nm can be assumed to be unity and therefore the backscatter phase function can be measured.

6) Linear depolarization ratio

The discrimination between water and ice clouds can be made from the depolarization properties of the backscatter signal. The linear depolarization ratio can be given as follows.

$$\delta_{a,m}(R) = N_{(a,m)\perp}(R)/N_{(a,m)\parallel}(R), \tag{13}$$

where $N_\perp$ and $N_\parallel$ are the number of incident on the receiver perpendicular and parallel to the receiver polarization axis, respectively. In the case of the HSRL, separate depolarizations of aerosol and molecular backscattering can be measured.

7) Cloud particle size

By measuring the signal strength variations as a function of field of view, the size of the cloud particles can be measured. The multiple scattered lidar return is a function of receiver field of view, particle size, range from lidar and the optical depth of the cloud. In the HSRL, the multiple scattering information along with the simultaneous single scattering measurement are used to calculate the cloud particle size.A detailed description of the multiple scattering approximation used for the HSRL measurements is presented by Eloranta[25,26] and Eloranta and Shipley[27].

3 Instrumentation

3.1 Introduction

3.1.1 An overview of the high resolution etalon based system

In the earlier versions of the University of Wisconsin HSRL, the separation between aerosol and molecular backscatter signals was made with a high resolution etalon with ~ 0.5 pm bandpass. The Figure 3 shows the receiver of the etalon based system[13]. The backscattered light was collected by the receiver telescope and directed through a fiber optics scrambler. The fiber optics scrambler was used to reduce the range dependence of the receiver spectrometer bandpass due to the angular sensitivity of the etalon transmission[12]. After collimation, the signal was prefiltered with an interference filter and a pair of low resolution etalons. After passing the dual aperture, the light was directed to the high resolution etalon. The high resolution etalon was slightly tilted with respect to the optical axis. This allowed the light that did not pass through the etalon to be reflected back to the dual aperture and to the molecular channel photodetector (PMT1). The light that passed through the high resolution etalon was detected with the aerosol channel photodetector (PMT2). The signal detected with the aerosol channel was a combination of aerosol backscatter spectrum and the center of molecular backscatter spectrum. The signal detected with the molecular channel was a combination of the wings of the molecular spectrum and the part of the aerosol backscatter spectrum that did not pass the high resolution etalon.

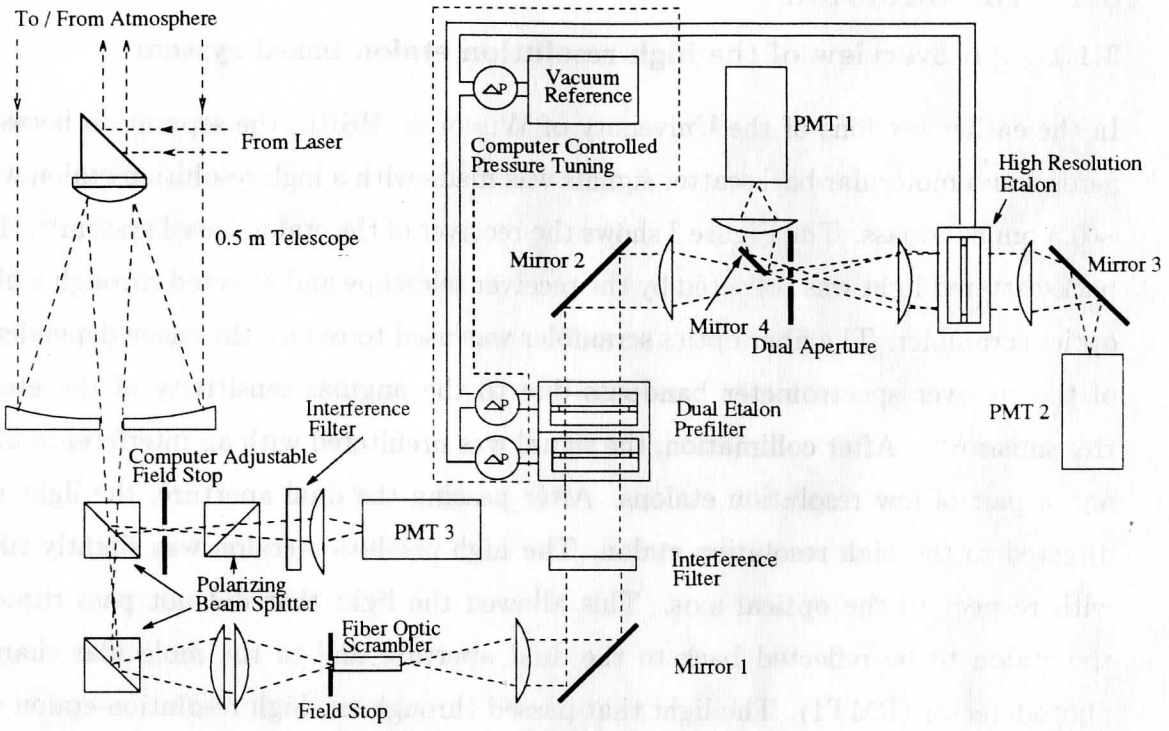

Figure 3. The receiver of the high resolution etalon based system. The backscatter signal is collected with a telescope. The fiber optics scrambler reduces the range dependence of the receiver spectrometer bandpass due to the angular sensitivity of the etalon transmission. The signal is background filtered with a interference filter and a pair of low resolution etalons. The separation between aerosol and molecular backscatter signals is done in the high resolution etalon. The part of the spectrum that transmits the etalon is combination of aerosol backscatter spectrum and the center of molecular backscatter spectrum (PMT2). The signal detected with PMT1 is a combination of the wings of the molecular spectrum and the part of the aerosol backscatter spectrum that did not pass the high resolution etalon.

3.1.2 A short introduction to the improvements

The instrument has been modified to measure polarization and a separate channel has been added to measure both polarization and signal amplitude variations as function of receiver field of view. These modifications allow discrimination between ice and water clouds and measurements of multiple scattering. Along with these modifications, the high resolution etalon, used in the earlier versions of the HSRL, has been

replaced with an iodine absorption filter. Also, the system has been redesigned for use in a semitrailer. Other changes include new data acquisition system, temperature controlled environment for the receiver optics, and improved optical design. The system parameters of the HSRL are summarized in Table 1.

The changes to the HSRL have improved the measurement capabilities of the HSRL. With the new HSRL, the measurements of the optical parameters of the atmosphere below 35 km can be made and therefore, the measurements can cover clouds from water clouds to high altitude cirrus clouds and also measurements of stratospheric aerosol layers can be performed. Clouds with optical depths up to ~ 3 can be measured. This means that most of the cirrus cloud cases can be fully observed and the cloud bases of the thick water clouds can be measured up to 300-500 m inside the cloud. This has been achieved by using a high pulse repetition rate, small pulse energy per laser pulse, and very fast photon counting electronics. Furthermore, the averaging time required for a good signal to noise ratio has been decreased by improving the optical transmission of the system. The use of the iodine filter, the controlling of the pressure of the etalons and the temperature of the optics, and the locking of the laser wavelength to an iodine absorption peak have increased the stability and the reliability of the system. Therefore, the need for frequent calibrations is eliminated and a stable operation can be maintained over a long period of time. The enhanced calibration technique has improved the accuracy of the HSRL calibrations.

Table 1. HSRL specifications (April 26, 1994)

Transmitter	
Wavelength	532 nm
Pulse duration	$\sim$ 130 ns
Pulse repetition rate	4 kHz
Average power	$\sim$ 0.2 W (seeded)
Frequency stability:	
Without I_2-locking	$\sim$ 100 MHz/hour (= 0.09 pm/h)
With I_2-locking	$\lambda\pm$ 0.052 pm
Receiver	
Telescope	
Type	Dall-Kirkham
Diameter	0.5 m
Focal length	5.08 m
Wide field of view channel	
Filter bandwidth	1.0 nm
Field of view	computer adjustable 0.21 $\rightarrow$ 4.0 mrad
Polarization rejection	$\sim 1\times10^{-3}$
Aerosol+molecular channel	
Filter bandwidth	8 pm
Field of view	0.160 mrad
Polarization rejection	$\sim 1\times10^{-3}$
Molecular channel	
Filter bandwidth	1.8 pm
Field of view	0.160 mrad
Polarization rejection	$\sim 1\times10^{-3}$
Photon counting data system	
Number of counters	3 (wfov, aerosol+molec., molec.)
Number of data buffers	6 (2 polarizations per channel)
Minimum bin width	100 ns
Number of bins	8192/channel
Max. rate of counters	$\sim 10^9$ Hz, tested to 350 MHz
Embedded computer	Intel i960CA
System control	Sun Sparc II

3.2 Transmitter

3.2.1 Transmitter laser

As a transmitter, the University of Wisconsin HSRL uses a continuously pumped, Q-switched, injection seeded, frequency doubled Nd:YAG laser operating at a 4 kHz pulse repetition rate[12] (Figure 4). The host cavity is based on a Quantronix model 116 laser. The quarter waveplates on either side of the Nd:YAG-rod are used to generate circularly polarized light in the rod in order to eliminate the spatial hole burning. The narrow bandwidth single frequency operation is achieved by injecting the cw-output of a diode pumped monolithic Nd:YAG ring laser (a modified Lightwave model S-100 seedlaser) into the host cavity through a partially transmitting rear mirror. Measurements have shown, that less than 100 MHz/h frequency drift is achieved. The 4 kHz pulse repetition rate is achieved by using an acousto-optic Q-switch.

The output of the laser is externally doubled by a KTP crystal. The frequency doubled output of the laser is tunable over a 124 GHz frequency range by controlling the temperature of the seedlaser diode. The original analog temperature controlling circuit of the seedlaser has been modified and connected to the microprocessor to allow remote control of the seedlaser Nd:YAG crystal temperature.

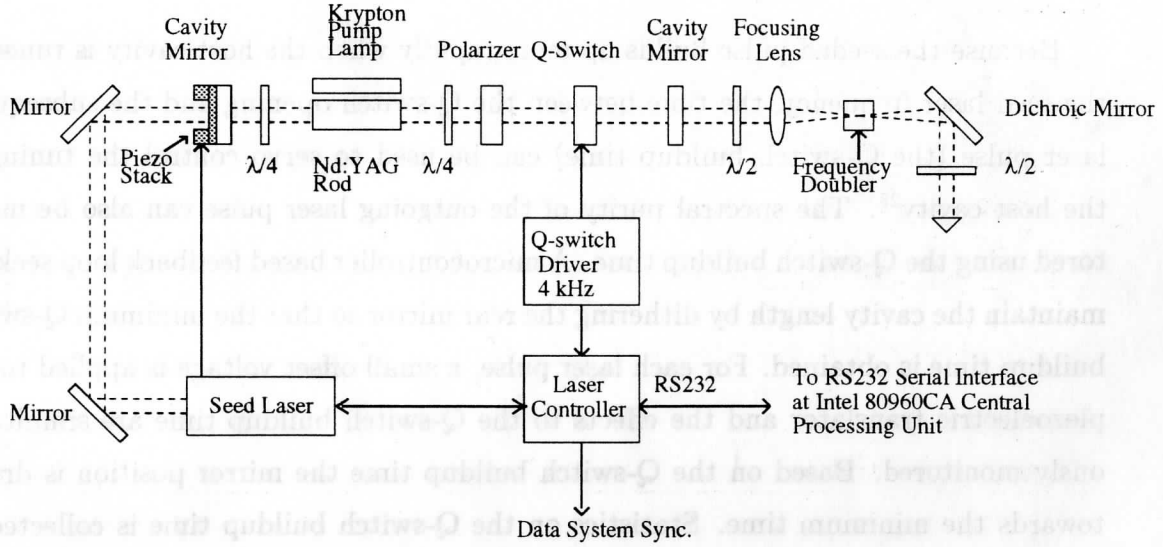

Figure 4. The HSRL transmitter laser.

After frequency doubling, the 532 nm and 1064 nm beams are separated by a harmonic beam separator. Because up to 15% of the residual 1064 nm beam is reflected from the beam separator, a second harmonic beam separator in the laser output (Figure 5) is used to provide more efficient filtering. The remaining 1064 nm beam is cleaned by a spatial filter. The spatial filter also cleans a halo of broader bandpass radiation.

Successful injection seeding requires that overlap between seedlaser resonance frequency and the frequency of a host cavity longitudinal mode is achieved. When the frequency of a host cavity longitudinal mode is locked to the seedlaser resonance frequency, the pulse developing out from the seedlaser signal will saturate the homogeneously broadened gain medium preventing development of any other axial modes from the spontaneous emission. Therefore, because one longitudinal mode is amplified more than any other mode, a spectrally narrow bandwidth pulse is generated. Since the seedlaser emissions used for injection seeding are generally $\sim$ 10 orders of magnitude stronger than the spontaneous emission, the Q-switched pulse builds up sooner out of the seed emission than the spontaneous emission. The frequency locking between seedlaser and host cavity is realized by controlling the host cavity length with a piezoelectric translator.

Because the seeded pulse builds up more rapidly when the host cavity is tuned to the seed laser frequency, the time between the Q-switch opening and the subsequent laser pulse (the Q-switch buildup time) can be used to servo control the tuning of the host cavity[28]. The spectral purity of the outgoing laser pulse can also be monitored using the Q-switch buildup time. A microcontroller based feedback loop seeks to maintain the cavity length by dithering the rear mirror so that the minimum Q-switch buildup time is obtained. For each laser pulse, a small offset voltage is applied to the piezoelectric translator and the effects to the Q-switch buildup time are simultaneously monitored. Based on the Q-switch buildup time the mirror position is driven towards the minimum time. Statistics on the Q-switch buildup time is collected at 4 kHz rate, but the mirror position is dithered at $\sim$ 140 Hz. The amount of dither is calculated based on the seeding percentage. The observed Q-switch build up time is $\sim$ 4.5 μs and the difference between seeded and unseeded conditions is typically

$\sim$ 500 ns. Because the spectral purity of the transmitted laser beam is important for HSRL measurements and because some shots are unseeded, the information from the Q-switch build up time is used to trigger the data system only for seeded shots.

The frequency stability of a single-frequency laser is determined by the seedlaser and the stability of the frequency locking is affected by the environment. The injection seeded operation is easily interrupted by mechanical vibrations transmitted through the support structure or through the cooling water or hoses. The effects of change in the optical length of the cavity due to thermal expansions of the support structure and temperature changes in the laser rod are compensated by the active controlling of the main cavity length. The laser is installed on a Super-Invar breadboard supported by a thick honey comb table that is mounted into a vibration insulated frame. The invar breadboard and the honey comb table are isolated from each other by a rubber pad. The laser was delivered with a Super-Invar table, which is thermally stable, but it is found to be acoustically sensitive. The active controlling of the main cavity length already minimizes the effects of changing environmental temperature so that an acoustically more insensitive table might provide a better performance. The mechanical vibrations coming from the laser cooling pump and transmitted into the cavity by hoses and water are isolated by a pressure dumper in the cooling water line. Because the original pressure dumper did not offer enough isolation, an extra damping system was installed. Also extra long elastic plastic water hoses are used to further attenuate the vibrations coming from the laser cooling pump. Furthermore, the temperature of the surrounding environment is stabilized by controlling the air temperature around the laser. The wavelength locking of the laser output to a iodine absorption line is demonstrated later in Chapter 5.2.

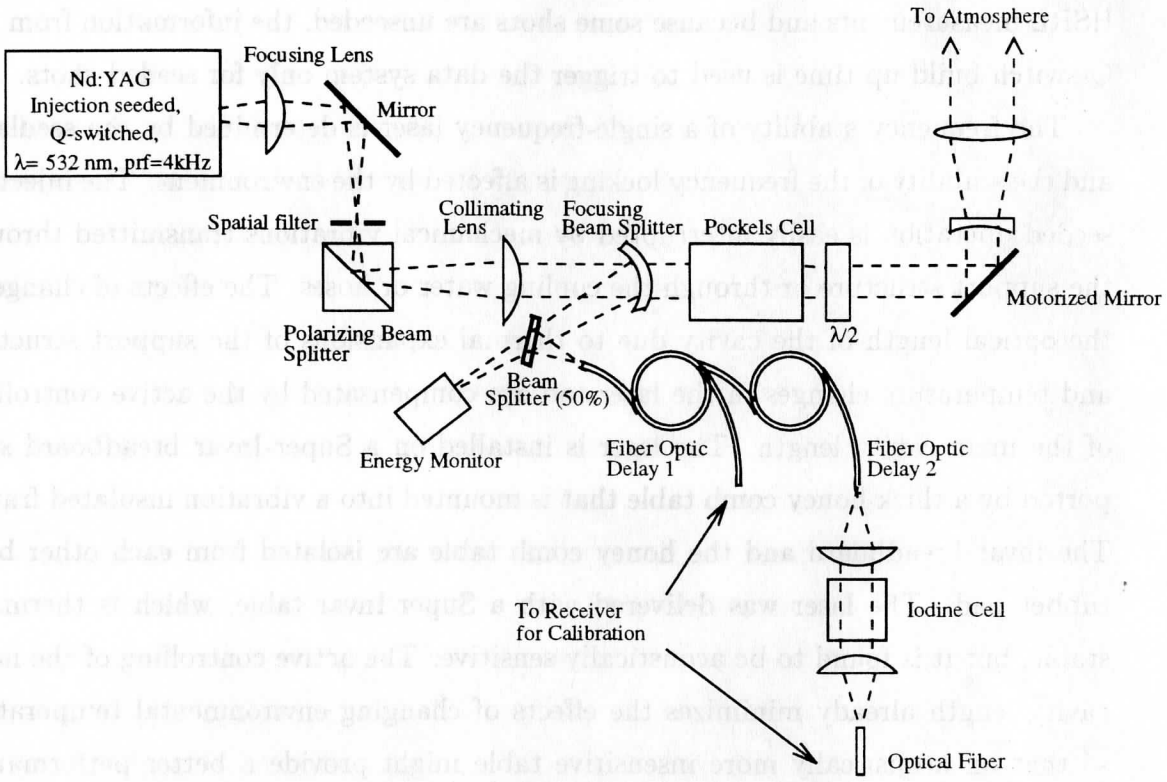

Figure 5. The HSRL transmitter setup. The HSRL transmitter employs an injection seeded, frequency doubled Nd:YAG laser. A Pockels cell in the output is used to rotate the polarization of the outgoing laser beam by 90 degrees for alternative laser pulses. An iodine absorption cell is used for the frequency locking of the laser wavelength. A sample of each laser pulse is directed to a pair of optical fibers, delayed, and injected back to the receiver for system calibrations. The length of the fibers is set so that the time-separated pulses can be recorded into the data profile.

3.2.2 Optics

A small amount (~2 %) of each transmitted laser pulse is directed into a pair of 100 m long optical fibers, delayed, and injected back to the receiver for system calibrations (see Figure 5). Since some of the laser shots are unseeded, the delay is necessary so that the measured Q-switch buildup time of each pulse can be used as a quality control to trigger the data system only for seeded shots. The length of the fibers is

set so that the time-separated pulses can be recorded in the data profile. The other ends of the calibration fibers are connected to a diffuse cylinder, which is located at the receiver such that the calibration light signals can be used to monitor system performance during data taking. Another 2 % of the laser light is taken into an energy monitor. The energy normalization of the received signal is realized by storing the energy of each laser pulse into the data record. A 4 cm long iodine cell is used for frequency locking of the laser. This cell provides $\sim$ 50 % absorption when the laser is tuned to the absorption peak. The frequency locking to the iodine peak is described later in Chapter 5.2.

Because the HSRL measures depolarization of the clouds and uses this information to separate between water and ice clouds, the polarization stage of the outgoing laser beam has to be well controlled. The output of the laser is linearly polarized and the orientation of the polarization vector is set perpendicular to the plane of the hypotenuse of the polarization cube. The use of the polarization cube guarantees that the residual cross-polarized component is cleaned out from the outgoing laser beam. In order to be able to use the same receiver optics and the same detector for both polarization components, the polarization of the outgoing laser pulse is rotated by 90 degrees for alternative laser pulses by a Pockels cell. The accuracy of the Pockels cell rotation is measured by observing the light coming from the Pockels cell through a polarizing cube with a photodetector. These calibrations show that the residual cross polarization can be reduced to 0.1 % of the parallel component. The calibration accuracy is limited by the 0.1 % rejection accuracy of the polarizing cube. The timing of the voltage switching between laser pulses is synchronized with the Q-switch signal and the controller electronics assures that the proper Pockels cell voltage is applied in time before the next laser shot. The final alignment between the transmitter and receiver polarization axes is performed by adjusting a half-waveplate and by using the atmosphere as a calibration target.

The use of small receiver field of views is made possible by decreasing the divergence of the outgoing laser beam with a beam expanding telescope (magnification 4x).

3.3 Receiver

3.3.1 Optics

The backscattered light is collected using a 50 cm diameter telescope (see Figure 6). To avoid specular reflection from horizontally oriented ice crystals, the system pointing direction is tilted by 4 degrees from the zenith. The signal polarized parallel to the receiver polarization axis and the signal perpendicular to that are separated by using a polarization cube (see Figure 6). This cube separates the signal to the WFOV-channel (PMT 3) and to the spectrometer-channels (combined aerosol+molecular channel (PMT1) and molecular channel (PMT 2)). An extra polarization cube for both channels is used to clean up the cross polarization component of the received signal down to a level that makes accurate depolarization measurements possible.

The multiple scattering properties can be studied by using the WFOV-channel, while simultaneously measuring the single scattering return with the spectrometer channels. A stepper motor driven aperture for the WFOV-channel enables field of view variations between 0.224 and 4 mrad. An interference filter with 1 nm bandpass is used for the background filtering. Because the field of view can be wide and the filter bandpass is broad, the WFOV measurements are currently limited to night time. The field of view of the spectrometer channels is 160 μrad, which further decreases the background sky noise and multiple scattering effects to the measured signal.

In order to achieve daytime measurements with the spectrometer channels, a low resolution etalon pair and an 1 nm interference filter are used to suppress the background solar radiance. The bandpass of the etalon pair is $\sim$9 pm, which is about 3 times the width of the expected Doppler broadened molecular spectrum. The length of the spacers is chosen so that only one common transmission order for the etalon pair occurs inside the interference filter bandpass. The bandpass of the low resolution etalon pair is wider than in earlier systems[8,12] in order to decrease the system sensitivity for the drift between transmitter wavelength and the etalon transmission maximum. The effects of environmental changes to the etalon performance are eliminated by mounting each etalon into a separate pressure and temperature controlled chamber. A third etalon chamber is used as a pressure reference. The absolute pressure in reference chamber and the differential pressures in each etalon chamber are

maintained by a computer controlled servo loop. The etalons are operated near the pressure where the changes in tuning gas density with temperature are cancelled by the thermal expansion of the etalon spacers[29]. Nitrogen is used as a tuning gas.

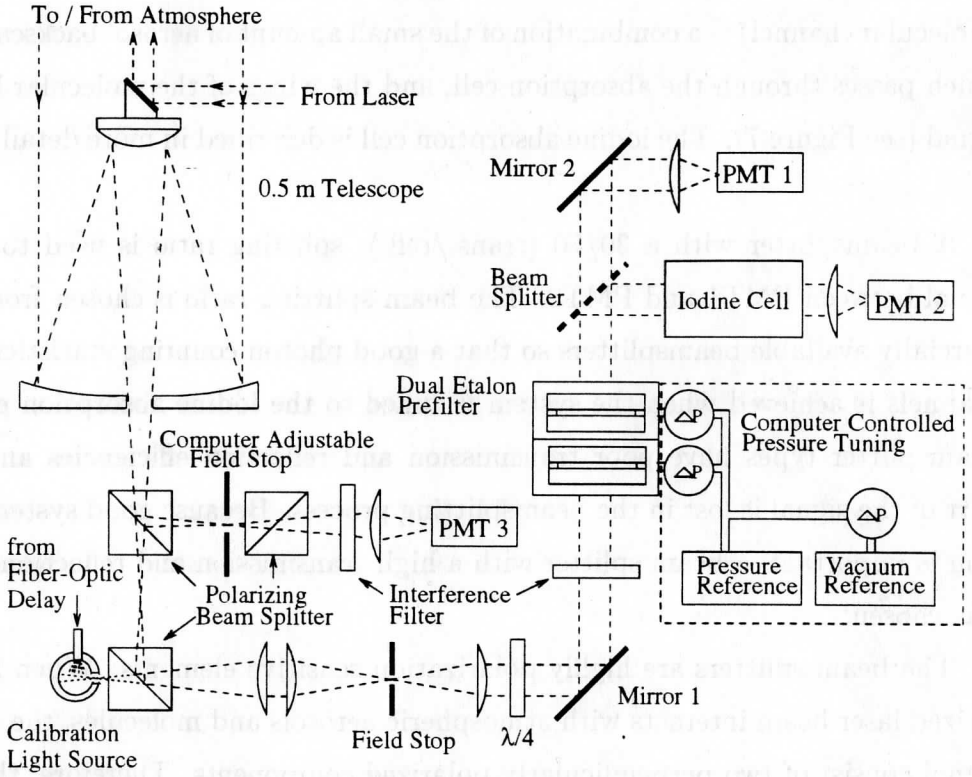

Figure 6. A polarizing prism at the output of the telescope separates the orthogonally polarized signals between wide field of view channel (PMT3) and the spectrometer channels (PMT1 and PMT2). Since the polarization of the transmitted laser pulse is rotated by 90^o between laser pulses, each channel alternatively receives perpendicular and parallel components. The received backscatter signal is prefiltered with an interference filter and a low resolution etalon pair before being directed into a beam splitter. The signal detected with PMT1 contains the information about the total aerosol and molecular backscatter signal. The signal directed through the iodine cell and detected by PMT2 is a combination of a amount of aerosol backscatter signal which passes through the absorption cell and the wings of the molecular backscatter signal.

After background filtering, the signal is divided into two channels by a beam splitter. The signal detected with the PMT1 (combined aerosol+molecular channel) contains the information about the total aerosol and molecular backscatter signal. The signal directed through the 43 cm long iodine cell and detected by the PMT2 (molecular channel) is a combination of the small amount of aerosol backscatter signal, which passes through the absorption cell, and the wings of the molecular backscatter signal (see Figure 7). The iodine absorption cell is described in more detail in Chapter 4.

A beamsplitter with a 30/70 (trans./refl.) splitting ratio is used to divide the signal between PMT1 and PMT2. The beam splitting ratio is chosen from the commercially available beamsplitters so that a good photon counting statistics with both channels is achieved when the system is tuned to the iodine absorption peak. Some beamsplitter types have poor transmission and reflection efficiencies and therefore part of the signal is lost in the beamsplitting process. Because good system transmission is important, a beam splitter with a high transmission and reflection efficiencies was chosen.

The beam splitters are highly polarization sensitive elements. When linearly polarized laser beam interacts with atmospheric aerosols and molecules, the backscatter signal consist of two perpendicularly polarized components. Therefore, the polarization sensitivity of the beamsplitter transmission and reflection has to be taken into account. The polarization sensitivity of the beamsplitter performance is noted as a problem in a system described by Krueger *et al.*[17]. The advantage of the HSRL is that the received signal is polarization filtered and therefore the light coming from the atmosphere to the beam splitter is always incident with the same polarization. On the contrary, the light from the current calibration light source is polarized orthogonally to the lidar signal and therefore the polarization sensitivity of the beam splitter creates a problem. This problem is solved by generating a circularly polarized light for the beamsplitter with a $\frac{\lambda}{4}$-waveplate.

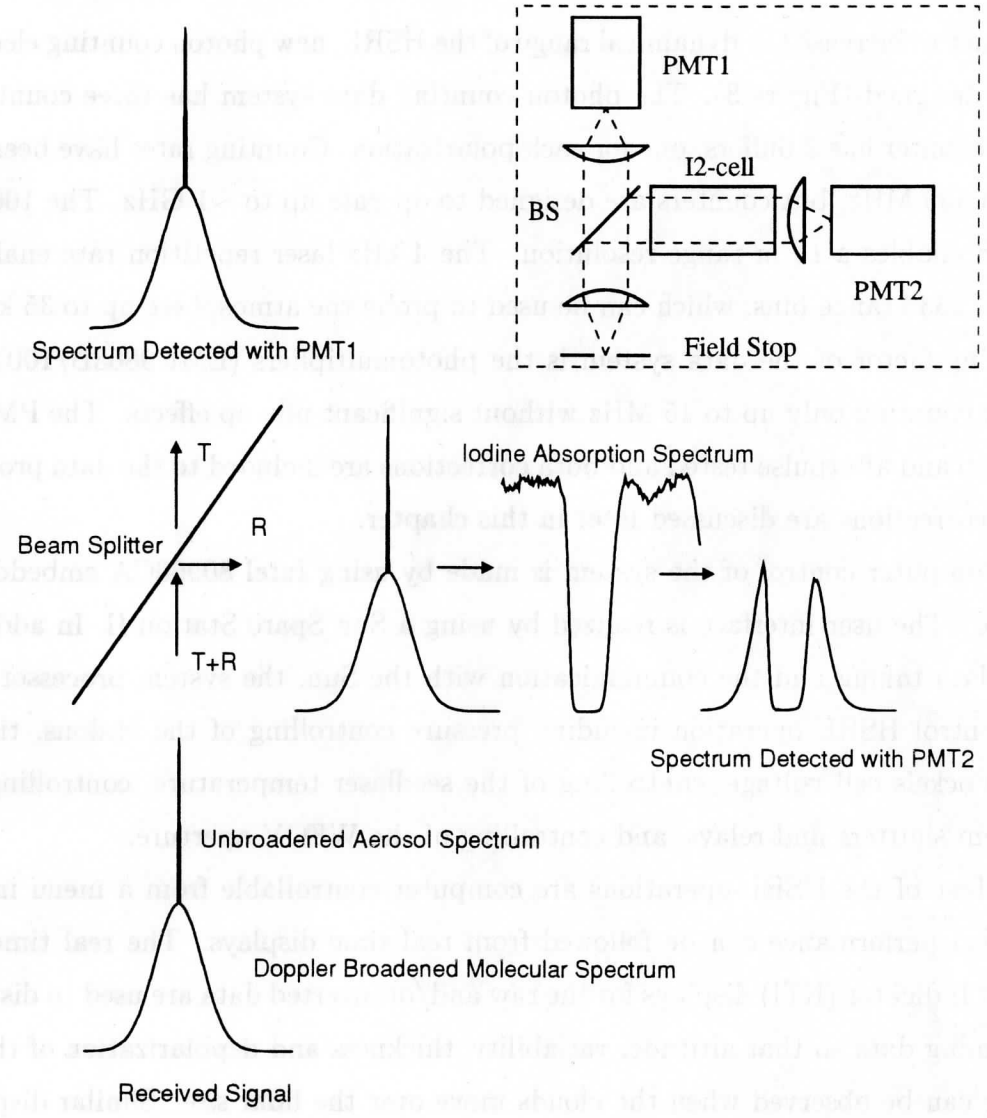

Figure 7. The spectral response of the HSRL receiver. The insert figure at the upper right corner shows a simplified setup of the spectrometer channels. The light that passes the field stop contains information about the Doppler-broadened molecular spectrum and the aerosol backscatter spectrum. The signal is divided into two parts with the beam splitter. The signal, which is transmitted through the beam splitter is detected with PMT1 and it contains information from the total backscatter signal. The signal, that reflects from the beam splitter is directed through an iodine absorption cell. In this process, the aerosol backscatter signal is attenuated in the iodine absorption line. Also the central parts of the molecular spectrum are filtered out and therefore the signal detected with PMT2 is a combination of the wings of the molecular spectrum and that part of the aerosol backscatter signal that passes through the cell.

3.3.2 Data system

In order to increase the dynamical range of the HSRL, new photon counting electronics were designed (Figure 8). The photon counting data system has three counters and each counter has 2 buffers, one for each polarization. Counting rates have been tested up to 350 MHz, but counters are designed to operate up to ~1 GHz. The 100 ns bin width enables a 15 m range resolution. The 4 kHz laser repetition rate enables the use of 2333 range bins, which can be used to probe the atmosphere up to 35 km. The limiting factor of the data system is the photomultipliers (EMI 9863B/100), which allow counting only up to 15 MHz without significant pile-up effects. The PMT's are pile-up and afterpulse tested and both corrections are included to the data processing. The corrections are discussed later in this chapter.

Computer control of the system is made by using Intel 80960CA embedded processor. The user interface is realized by using a Sun Sparc Station II. In addition to the data taking and the communication with the Sun, the system processor is used to control HSRL operation including pressure controlling of the etalons, timing of the Pockels cell voltage, controlling of the seedlaser temperature, controlling of the system shutters and relays, and controlling of the WFOV aperture.

Most of the HSRL-operations are computer controllable from a menu interface. System performance can be followed from real time displays. The real time Range Time Indicator (RTI) displays for the raw and/or inverted data are used to display the incoming data so that altitude, variability, thickness and depolarization of the cloud layer can be observed when the clouds move over the lidar site. Similar displays for the cloud optical properties (optical depth, aerosol backscatter cross section, phase function) can be shown.

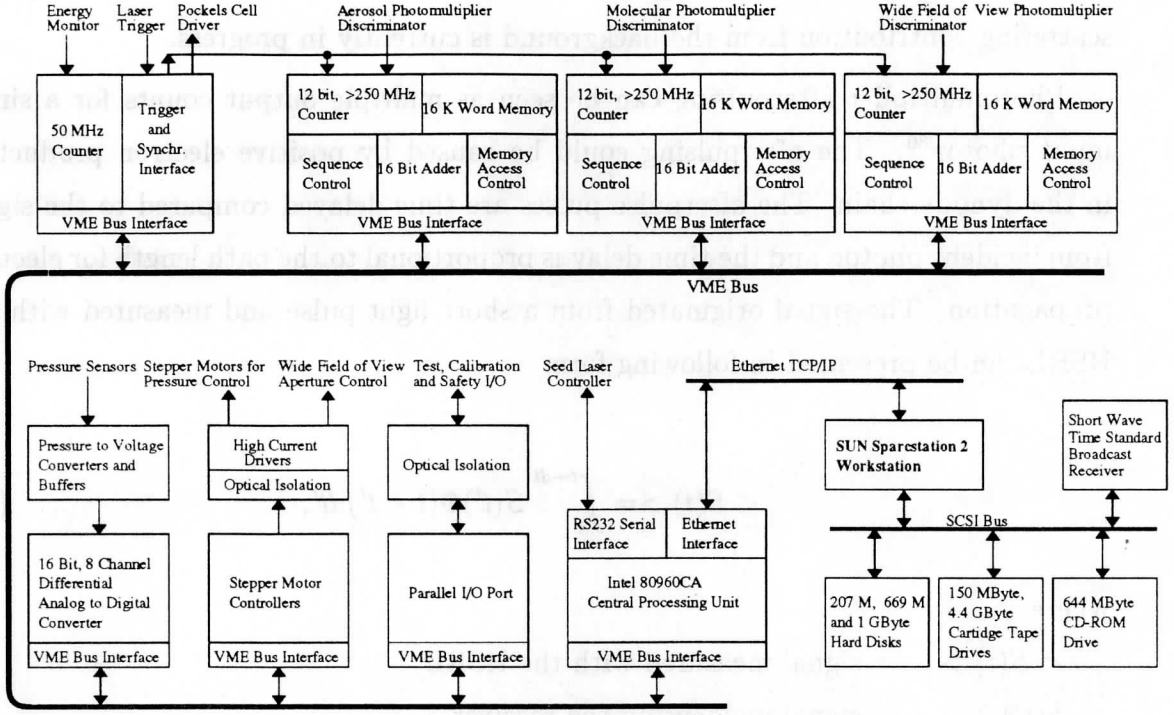

Figure 8. The HSRL data acquisition system.

The new counter design has improved the background light measurement accuracy of the HSRL. Instead of interrupting the data taking every 3.5–7 min for background and calibration checks (as was made with the system described by Grund[10]), the new HSRL is capable of measuring the background light simultaneously with the data. The maximum resolution of the data system is increased from 256 to 4096 range bins per channel. In the HSRL, the amount of background light in the measurement is calculated from the measured profile by using the upper altitudes of the lidar profile. The signal together with the background light is saved and therefore different kind of background corrections can be studied. Currently, the measured HSRL profiles are background corrected by assuming the signal above ~33 km to be background. By averaging the upper range bins together, the average amount of background in the measurement is calculated. The disadvantage of the current background correction method is that some of the signal can still be originated from Rayleigh scattering

leading into an overestimate of the amount of background light for altitudes 33 km or higher. A development of a background correction method that removes the Rayleigh scattering contribution from the background is currently in progress.

Photomultiplier afterpulsing can be seen as multiple output counts for a single input photon[30]. The afterpulsing could be caused by positive electron production in the dynode chain. The afterpulse pulses are time delayed compared to the signal from incident photon and the time delay is proportional to the path length for electron propagation. The signal originated from a short light pulse and measured with the HSRL can be presented in following form

$$< S(t) >= \int_0^{t+dt} S(t')\Phi(t-t')dt', \tag{14}$$

where

$< S(t) >$	= signal measured with the HSRL
S(t')	= signal incident on the receiver
Φ	= signal responce function, that contains the laser pulse width, datasystem bin width and afterpulsing of the photomultiplier

The afterpulse probability distributions were measured by illuminating the photomultiplier photocathode with a short duration laser light pulse. Pulse counting rates less than one count per 100 ns long data bin per pulse were used. A large number of laser pulses were averaged (~1 hour average). The probability distributions were calculated from the background corrected data. The amount of background light was calculated from the end of data record and the average value was subtracted from data. The measured afterpulse probability distributions of two photomultiplier tubes are presented in Figure 9. The afterpulse probability distribution was found to be different for each tube and therefore a separate correction for each tube had to be implemented to the signal analysis program. With a known afterpulse probability distribution function, the afterpulse contribution can be removed from the measured signal by using deconvolution. The effect of afterpulse correction to the measured signal is presented in Figure 10.

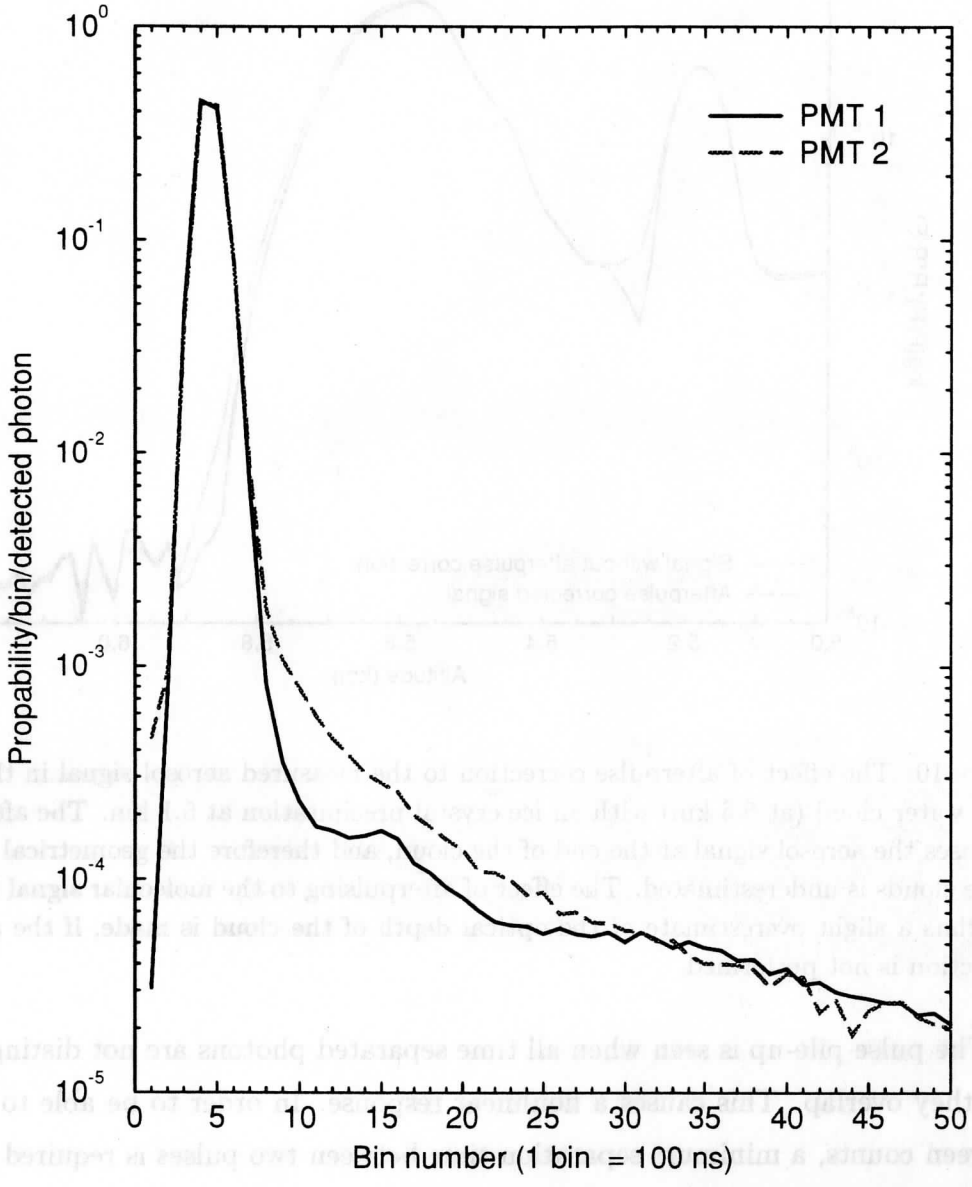

Figure 9. The temporal distributions of two EMI 9863B/100 photomultiplier tubes. The temporal distribution of the measured photons is a convolution of the laser pulse width, bin width of the data system, and the afterpulsing of the photomultiplier. The laser pulse is located in the first bins and the afterpulse can be seen as a decaying tail. The afterpulse distribution of the PMT1 shows better afterpulse behavior than the PMT2.

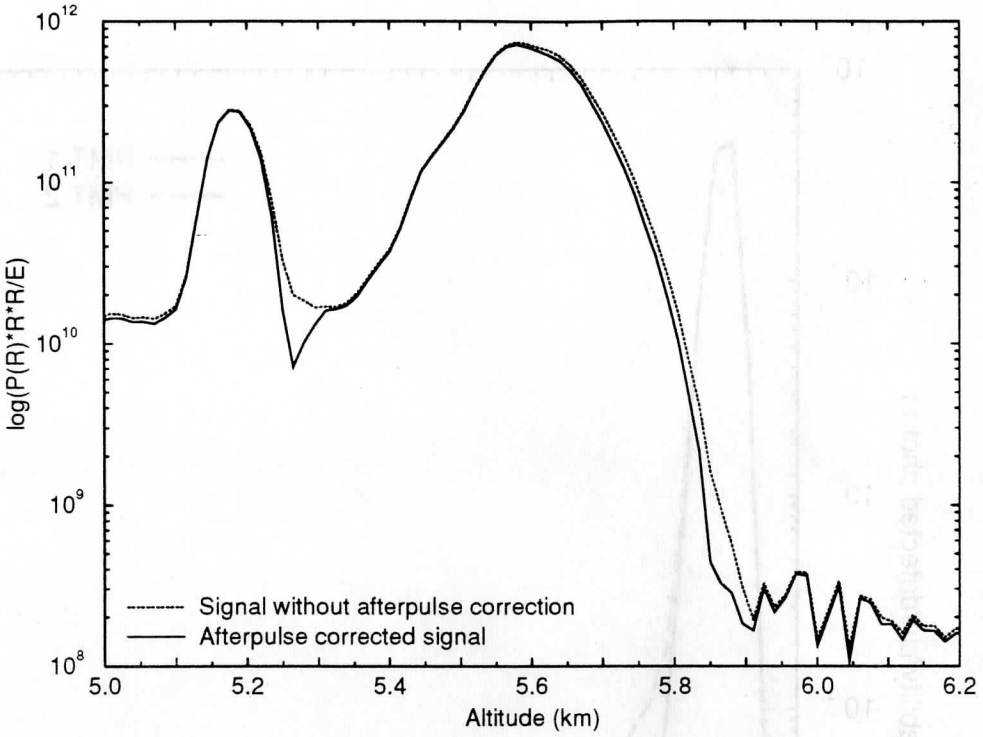

Figure 10. The effect of afterpulse correction to the measured aerosol signal in the case of thick water cloud (at 5.6 km) with an ice crystal precipitation at 5.1 km. The afterpulsing increases the aerosol signal at the end of the cloud, and therefore the geometrical thickness of the clouds is underestimated. The effect of afterpulsing to the molecular signal is similar, and thus a slight overestimate of the optical depth of the cloud is made, if the afterpulse correction is not performed.

The pulse pile-up is seen when all time separated photons are not distinguishable and they overlap. This causes a nonlinear response. In order to be able to separate between counts, a minimum separation time between two pulses is required for them to be distinguished. This time is called resolving time (or dead time). Since the time interval distribution of photons that reach the photomultiplier follow a Poisson distribution, the probability P_o that a pulse overlaps with another pulse inside a certain time interval is given by the following formula[31]

$$P_o = 1 - e^{-R\tau} \tag{15}$$

where

τ = resolving time

R = average count rate

In order to obtain the resolving time (dead time) of the photomultipliers, the photomultiplier responses to different count rates were tested. First, light level is set to level which is high enough to generate a pile-up. Then the photomultiplier response to different light levels is measured by changing the light intensity with neutral density filters and recording the signal change. In order to be able to define the resolving time of the photomultiplier, the photon counting was modeled. The pulses coming from the photomultiplier were treated as Poisson distributed signals. The resolving time that produced the best fit between simulated and measured results was used for the pile-up correction. All photomultipliers were found to have $\sim$ 13 ns resolving time. The pile-up correction has to be performed before the afterpulse correction or any other corrections, because the pile-up effect is nonlinear. The pile-up is affected by the signal strength, signal background and afterpulsing and therefore, data has to contain the information from all these factors when the correction for pile-up is performed.

In order to make the pile-up correction for data, the following equation was used

$$N = N_o e^{-R\tau} \tag{16}$$

where

N = measured counts

N_o = actual counts

τ = resolving time

R = average count rate = $\frac{N_o}{dt}$

This equation is solved iteratively for N_o, so that

1. $N_o(1) = \mathrm{N}$
2. New $N_o(i+1) = Ne^{\frac{N_o(i)}{dt}\tau}$, where dt = bin length [s]

3. Step 2 is repeated until N_o converges

The effect of pile-up correction to the measured signal is presented in Figure 11.

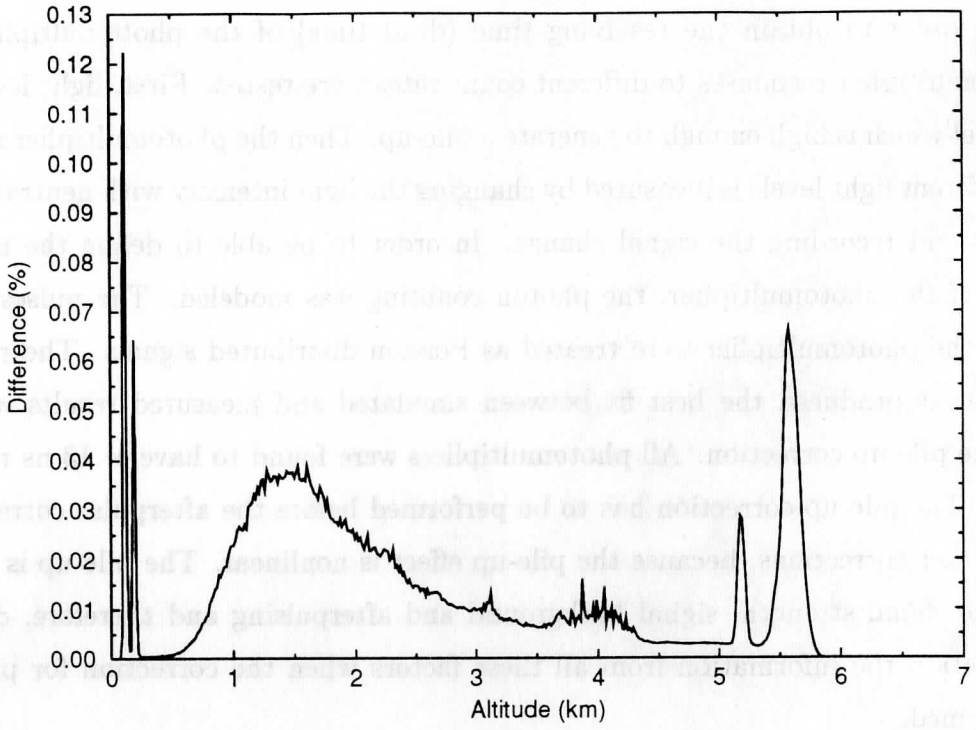

Figure 11. The effect of pile-up correction to the measured aerosol signal in the case of thick water cloud (at 5.6 km) with an ice crystal precipitation at 5.1 km. The calibration fiber signals are shown as spikes at altitudes $\sim$ 0 km. The maximum number of photons measured for the water cloud is 0.68 photons/100 ns bin and after pile-up correction 0.75 photons/100ns bin are observed. Even with this low count rates the effect of pile-up is $\sim$ 10% and therefore, the pile-up correction is very important when strong returns from clouds are studied.

4 Iodine absorption filter

In order to overcome the limited capability of the high resolution etalon to separate between aerosol and molecular scattering and to increase the system stability and reliability, an iodine absorption filter was constructed. For the first HSRL measurements a 43 cm long cell was made. The cell was made from glass tubing with an attached side arm. Optical quality end windows with anti-reflection coatings were epoxed to the ends. The cell with iodine crystals in a side arm was evacuated and kept at 27 °C. Transferring of the iodine from the absorption cell into the vacuum pump was prevented by evacuating the cell through a cold trap and cooling the side arm with liquid nitrogen. Although the iodine cell can be operated at room temperature, the operating temperature of the cell has to be controlled, because the vapor pressure of iodine is very temperature sensitive[32]. In the HSRL, the cell temperature is maintained with ±0.1 °C accuracy by operating the cell in temperature controlled environment.

The iodine spectrum is measured by scanning the laser wavelength by changing the temperature of the seedlaser under computer control. A small amount of laser light is directed into a 100 m long fiber optic delay (Fiber 1 in Figure 4) and sent to the receiver to create a calibration light source. The temperature-wavelength dependence of the scan was determined by using the free spectral range of the high resolution etalon as a reference. This could be made, because the free spectral range of the etalon can be calculated when the length of the etalon spacers is known and the spacing of two (or more) etalon transmission peaks in temperature units can be measured. The calibration was made by simultaneously measuring the transmission spectrum of the high resolution etalon and iodine absorption filter. The simultaneous measurement of the high resolution etalon and iodine absorption filter transmissions was made by measuring the signal reflected from the high resolution etalon (Figure 12) and the signal transmitted through the absorption cell. The pressure in etalon was held constant while the laser wavelength was scanned. The spectrum was normalized by measuring the cell transmittance without the iodine cell.

A part of the measured iodine spectrum is presented in Figure 13. The measured spectrum was compared with a published spectrum[18] and an ~0.01 pm wavelength

agreement in relative line positions was observed. The linearity of the temperature scan was confirmed from the free spectral range information of high resolution etalon by performing the scan over more than one free spectral range. Single mode operation between two seedlaser mode hops can be maintained over 20 GHz range (at 1064 nm) and within this range two high resolution etalon free spectral ranges can be covered. During a mode hop the laser frequency jumps back about 10 GHz.

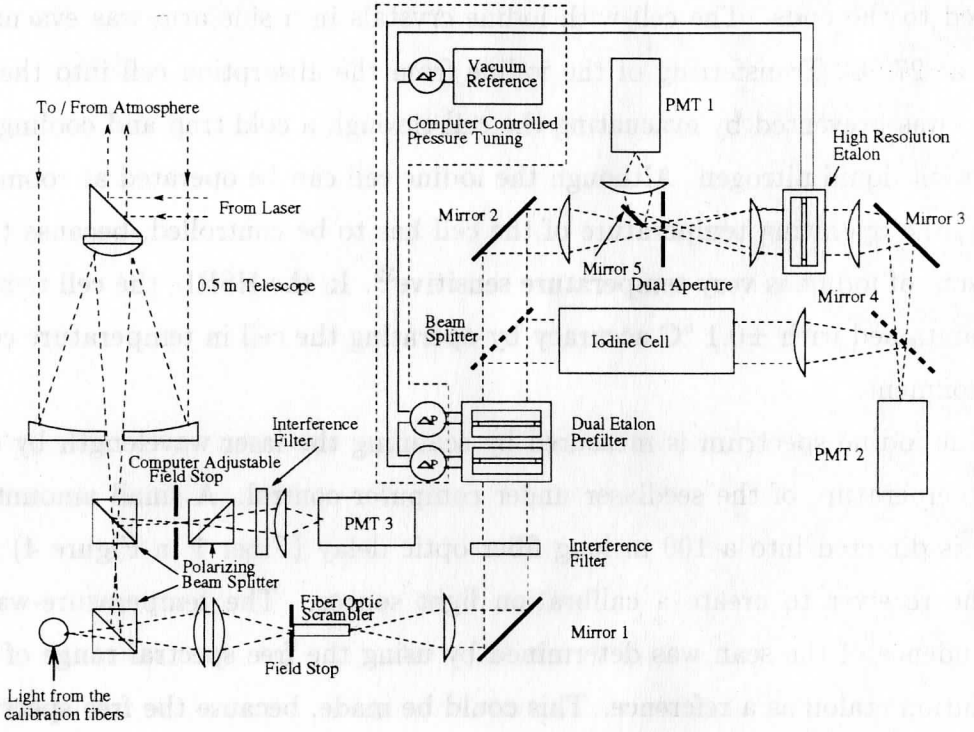

Figure 12. The HSRL receiver used for iodine spectrum calibrations. The same receiver setup was used for the first HSRL measurements with the iodine absorption filter. For data taking the transmission of the high resolution etalon was tuned out from the peak and the etalon was used as a reflector. When the beamsplitter and the mirror 4 are removed from the system, the system returns back to the old HSRL receiver.

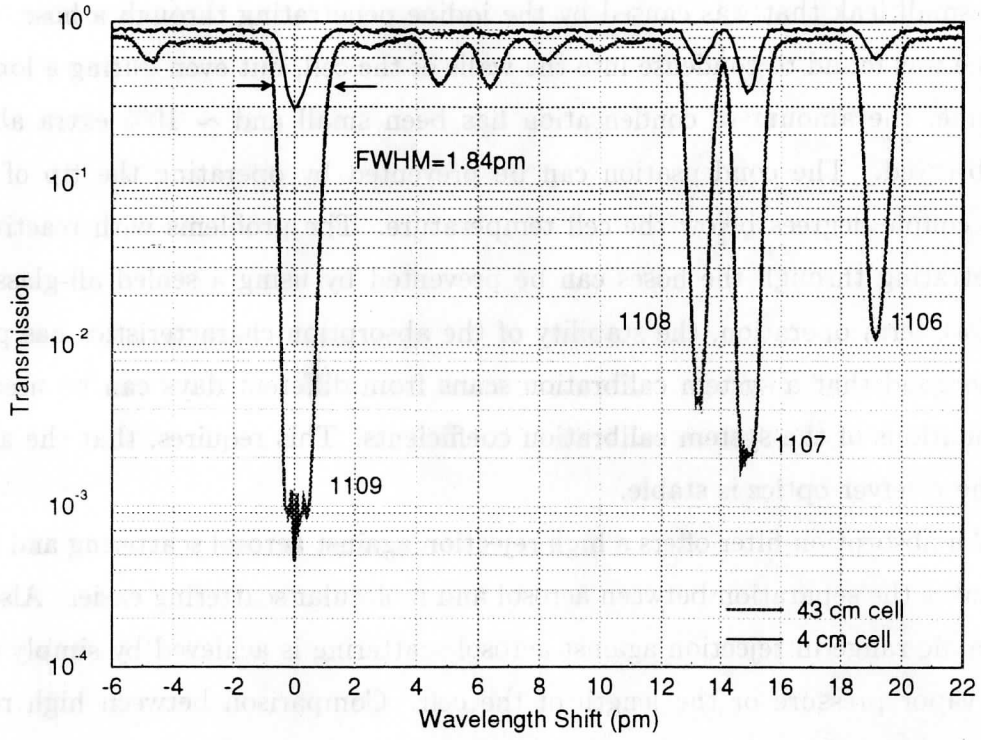

Figure 13. Transmission of a 4 cm and 43 cm iodine cells as a function of wavelength shift. The identification line numbers are from Gerstenkorn and Luc[18].

For initial HSRL measurements the line 1109 (peak wavelength 532.26 nm)[18], which is well isolated from the neighboring lines, was chosen. The full width half maximum width of the line is ~1.8 pm and the peak transmission is ~ 0.08%. The hyperfine structure of the peak 1109 defines the asymmetric shape of the absorption peak[33]. In fact, the line 1109 is a combination of two rotational vibrational transitions with different hyperfine structures.

The iodine absorption cell provides a robust filter for the HSRL, because it is not dependent on the mechanical alignment of the filter or the angular dependence of the incoming light. Another advantage is the stability of the absorption characteristics. This provides a stable long term operation. The strength of observed absorption line is dependent on the line strength, and the length, temperature, and pressure of the cell. By controlling the operating environment and with a nearly leak proof system, the

current iodine cell is operated for several months without any maintenance. During this time, a small change in absorption strength and line width were observed due to a small leak that was caused by the iodine penetrating through a hose. Also the iodine was found to condense into the walls of the cell, but even during a long period of time, the amount of condensation has been small and $\sim$ 10% extra absorption is observed. The condensation can be prevented by operating the tip of the side arm couple degrees below the cell temperature. The problems with reactive iodine penetrating through the hoses can be prevented by using a sealed all-glass cell. In a short term operation, the stability of the absorption characteristics has proven to be so good that a system calibration scans from different days can be used for the calculations of the system calibration coefficients. This requires, that the alignment of the receiver optics is stable.

An absorption filter offers a high rejection against aerosol scattering and therefore it makes the separation between aerosol and molecular scattering easier. Also, a wide dynamic range in rejection against aerosol scattering is achieved by simply changing the vapor pressure or the length of the cell. Comparison between high resolution etalon and iodine absorption filter performance is presented in Figure 14. A 2:1 separation between molecular and aerosol scattering by the etalon (Figure 14.b) is measured compared to a 1000:1 separation in the iodine cell when operated at 27 °C (Figure 14.a). The molecular transmission in Figure 14.a and Figure 14.b is calculated by using the Doppler-broadened molecular spectrum at -65 °C. This temperature is close to the lowest temperature measured at the tropopause and this gives the smallest transmission through the iodine absorption cell. The molecular transmission of the high resolution etalon and the iodine absorption filter are similar (Figure 14.c). Due to wide absorption line width, the molecular transmission of the iodine filter is more dependent on the air temperature than the etalon. The temperature dependence of the cell transmission is modeled by using the table values of iodine vapor pressure[32] (Figure 14.d). Calculations show, that by changing the cell temperature from 27 °C to 0 °C, the online transmission can be tuned from 0.08% to 60%.

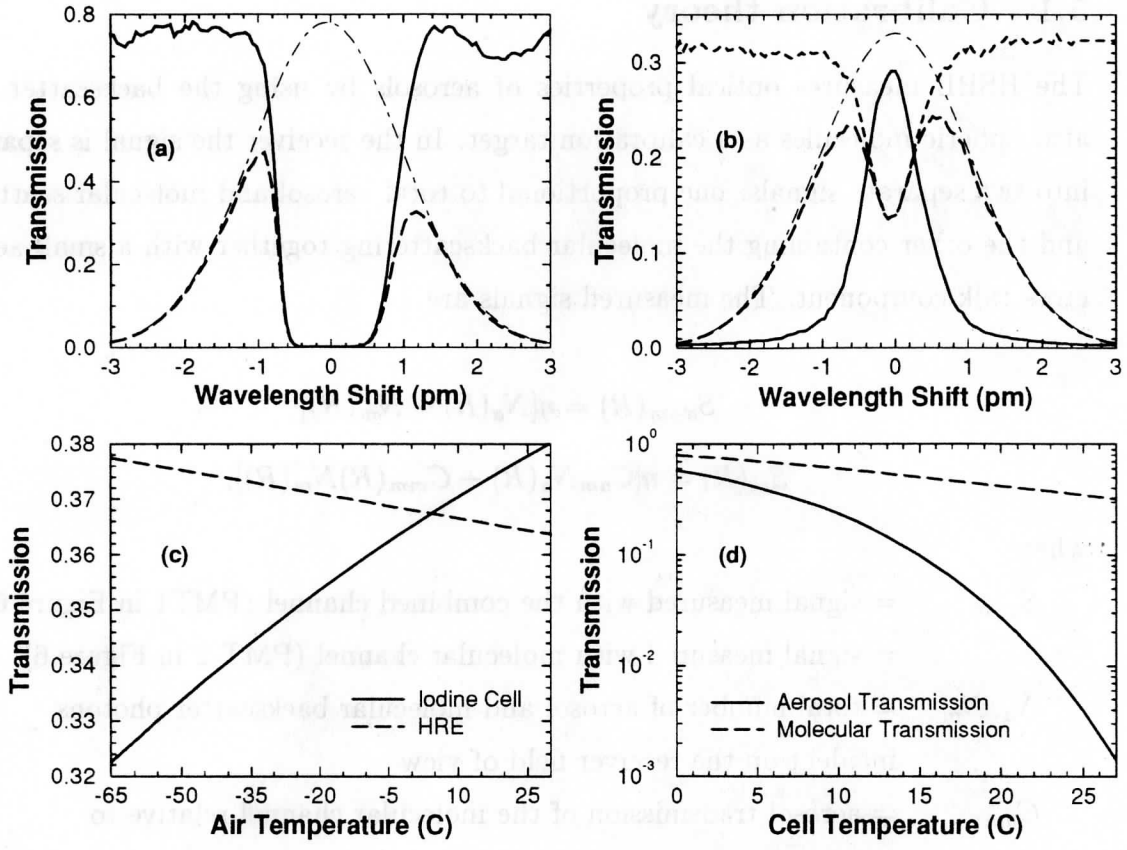

Figure 14. (a) Transmission of 43 cm cell (solid line) together with the molecular transmission (dashed line) at -65 °C air temperature as a function of wavelength shift. Dot-dashed line shows the calculated molecular spectrum at -65 °C. (b) Etalon transmission (solid line) and calculated molecular transmission (dashed line) as a function of wavelength shift. Dot-dashed line shows the calculated molecular spectrum at -65 °C. (c) Comparison of molecular transmission of high resolution etalon and iodine cell as a function of air temperature. (d) Iodine cell aerosol and molecular transmission as a function of cell temperature.

5 Calibration and tuning

5.1 Calibration theory

The HSRL measures optical properties of aerosols by using the backscatter from atmospheric molecules as a calibration target. In the receiver the signal is separated into two separate signals: one proportional to total aerosol and molecular scattering and the other containing the molecular backscattering together with a small aerosol cross talk component. The measured signals are

$$S_{a+m}(R) = \eta[N_a(R) + N_m(R)] \tag{17}$$

$$S_m(R) = \eta[C_{am}N_a(R) + C_{mm}(R)N_m(R)], \tag{18}$$

where

S_{a+m} = signal measured with the combined channel (PMT1 in Figure 6)

S_m = signal measured with molecular channel (PMT 2 in Figure 6)

N_a, N_m = total number of aerosol and molecular backscatter photons incident on the receiver field of view

C_{am} = aerosol transmission of the molecular channel relative to the combined channel

C_{mm} = molecular transmission of the molecular channel relative to the combined channel

η = system efficiency factor that includes the optical transmission of the combined channel and its photomultiplier quantum efficiency

These two equations can be solved to present the separated aerosol and molecular backscatter signals.

$$N_m(R) = \frac{S_m(R) - C_{am}S_{a+m}(R)}{\eta(C_{mm}(R) - C_{am})} \tag{19}$$

$$N_a(R) = \frac{S_{a+m}(R) - \eta N_m(R)}{\eta} \tag{20}$$

The calibration coefficients C_{am} and C_{mm} are obtained from a system calibration scan. For calibration the system input aperture is uniformly illuminated with a diffuse

light. The receiver spectral transmission function is measured by scanning the laser wavelength over an 11 pm wavelength range around the selected iodine absorption peak and recording the signals (originated from calibration fiber 1 and calibration fiber 2) with both spectrometer channels (PMT1 and PMT2 in Figure 6). A calibration scan is performed before and after each dataset. When system is running for a long period of time (time $\sim$ 3 hours) the system operation is interrupted and a calibration scan is performed. An example from a calibration scan is presented in Figure 15. In addition to the information on the system spectral transmission, the calibration signals contain information on the beamsplitting ratio between channels. Since the signal measured through the iodine cell is flat at the top of the iodine absorption peak, the determination of the wavelength of the absorption maximum is based on the signal from the reference iodine cell (4 cm cell in Figure 5, calibration fiber 2) and measured with the PMT1. Otherwise, the signals from the first calibration fiber are used for the calibration coefficient calculations.

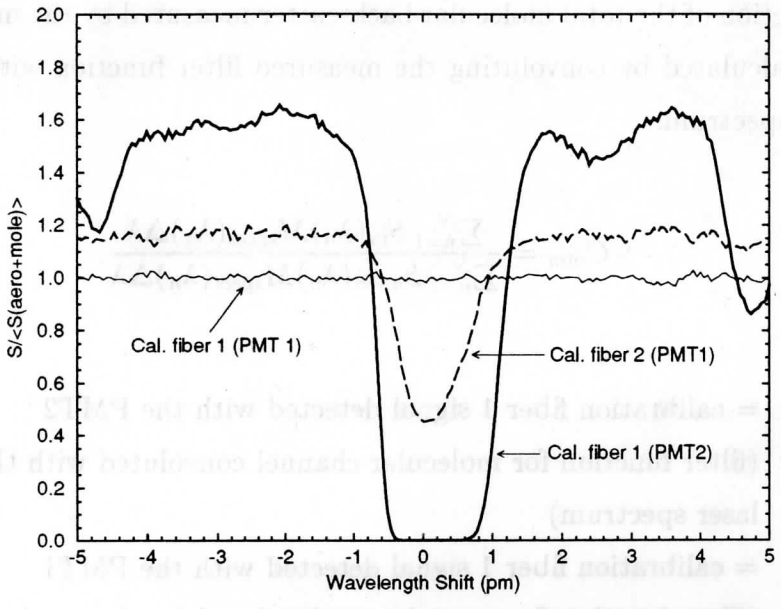

Figure 15. An HSRL calibration scan. The calibration fiber 1 signal that is detected with PMT2 shows the iodine absorption spectrum of the 43 cm long iodine cell. The calibration fiber 2 signal detected with PMT1 presents the absorption spectrum of the 4 cm long reference cell. The signal from calibration fiber 1 and detected with PMT1 is used as a reference.

Since the Doppler-broadening of the aerosol backscatter is negligible, the spectral distribution of the aerosol backscatter can be assumed to be similar to the spectral distribution of the transmitter laser. The measured calibration signals can be presented as a convolution between laser spectral distribution and spectral bandpass of each channel. Therefore, the fraction of the total aerosol backscatter detected by the molecular channel (C_{am}) can be directly obtained from the calibration signals.

$$C_{am} = \frac{S_m(\text{at peak})}{S_{a+m}(\text{at peak})}, \tag{21}$$

where

S_m = calibration fiber 1 signal detected with the PMT2 at the iodine absorption peak

S_{am} = calibration fiber 1 signal detected with the PMT1 at the iodine absorption peak.

The fraction of the total molecular backscatter measured by the molecular channel (C_{mm}) is calculated by convoluting the measured filter function with the calculated molecular spectrum.

$$C_{mm} = \frac{\sum_{n=1}^{N} S_m(\lambda_n) M_{spect}(\lambda_n) \Delta\lambda}{\sum_{n=1}^{N} S_{a+m}(\lambda_n) M_{spect}(\lambda_n) \Delta\lambda}, \tag{22}$$

where

S_m = calibration fiber 1 signal detected with the PMT2 (filter function for molecular channel convoluted with the laser spectrum)

S_{a+m} = calibration fiber 1 signal detected with the PMT1 (filter function for aerosol + molecular channel convoluted with the laser spectrum)

M_{spect} = calculated molecular spectrum

N = number of points in calibration scan

λ = wavelength

$\Delta\lambda$ = the wavelength difference between two points in the calibration scan

The divisor on the Eq. 22 is presented as a convolution aerosol and molecular channel. Therefore, the divisor presents the amount of molecular spectrum seen with the combined aerosol and molecular channel. The dividend of the Eq. 22 describes the molecular signal detected through the iodine absorption cell. The molecular spectrum model used in the calculation is presented in a paper by Yip and Nelking[34] and it includes the effects of Brillouin scattering as a function of temperature and pressure.

The accuracy of the calibration coefficients is mainly limited by the photon counting statistics. Because the signal transmitted through the absorption peak is small, the error due to photon counting statistics dominates the error in the determination of C_{am}. Therefore, the accuracy of the C_{am} is improved by increasing the photon counting statistics at the absorption peak. Three different ways to increase the photon counting statistics can be considered. First, the signal at the absorption peak can be increased by scaling the light with neutral density filters while scanning. Second, the amount of aerosol backscatter signal can be further decreased into a point where the effects of the photon counting statistics are negligible. Third, longer averaging time can be used.

The disadvantage of using neutral density filters is that the filters have to be well calibrated and the change in the value of neutral density filter has to recorded into the data so that the signal can be reconstructed back to the absorption spectrum. The disadvantage of the longer absorption cell is that the increased cell length will further decrease the amount of transmitted molecular signal. Also the spectral purity of the laser limits the observable absorption strength. In order to be able to obtain a good photon counting statistics for the signal of the whole absorption peak, a long averaging time is required and therefore the total calibration time would be unreasonable long ($\sim$ 1h) and during this time the laser has time to drift. The drift in the laser output wavelength during the scan effects the width of the measured absorption spectrum.

The current HSRL uses a calibration procedure, where the absorption spectrum is first measured by scanning the laser wavelength so that $\sim$ 1% photon counting accuracy is achieved for the spectrum around the absorption peak. In order to obtain

a high photon counting statistics in short period of time, the light from the calibration fibers is optimized so that maximum number of photons is detected with small pile-up effects at the detectors. During the scan the location of the peak absorption maximum is detected from the signal through the 4 cm long reference iodine absorption cell. After completing the scan, the seedlaser temperature is set back to the maximum and by using a tuning program (described in more detail in Chapter 5.2) the laser wavelength is kept at the absorption peak until better than 3% photon counting statistics is obtained. With this procedure the effects due to a shift in the laser output wavelength to the width of the absorption spectrum can be minimized and the photon counting errors in the determination of the C_{am} can be reduced from about 20% to 3% within $\sim$ 10 min averaging time.

The atmosphere provides the best reference when the accuracy of the HSRl calibrations is studied. Figure 16 presents an HSRL calibration which is performed simultaneously with data taking. Two different cases are studied. First, a calibration from a thick water cloud is shown. Second, a calibration from clear air is presented. In order to detect the possible range dependence of the calibration, lidar returns from different altitudes are studied. The comparison between calibrations from atmosphere and from the calibration light source also recovers possible misalignments of the system.

The system calibration signal from the iodine absorption spectrum presents a calibration from a pure aerosol target. The agreement between system calibration and atmospheric calibration from a thick water cloud can be seen from Figure 16. Both signals are defined from the ratio of the signal detected through the iodine cell to the signal detected with the combined aerosol+molecular channel. The background corrected, energy normalized signals are used. The data is averaged over a 90 m range. An expected calibration curve from a pure molecular target can be calculated by convoluting the measured iodine absorption spectrum with the calculated molecular spectrum. The calculated molecular calibration together with a measured atmospheric calibration from different altitudes are presented in Figure 16.b-d. The measured absorption spectrum is presented as a reference. For the calculated molecular calibration, the atmospheric temperature, and therefore the width of the Doppler-

broadened molecular spectrum, is calculated by using the temperature values obtained by a radiosonde measurement. The signals from higher altitudes are disturbed by the low photon counting statistics, but otherwise a good agreement between system calibration and atmospheric calibration is obtained and no range dependence in the system calibration is observed. The range dependence of the atmospheric calibration would show up as a noticeable deviation from the system calibration.

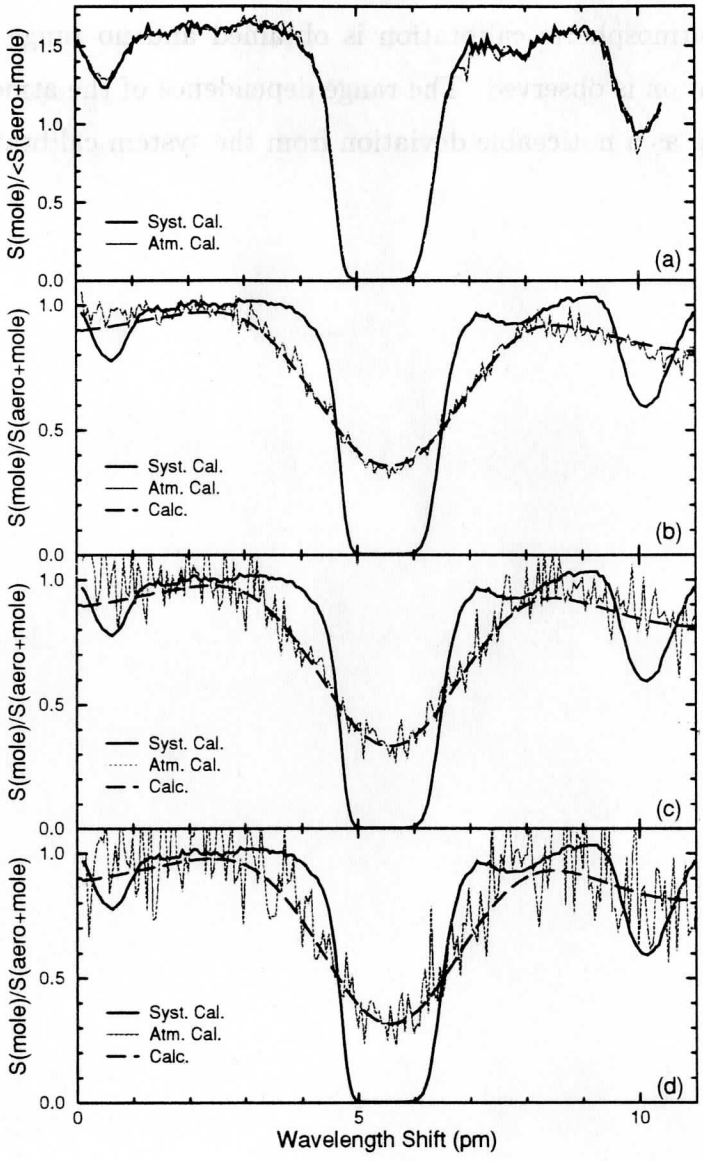

Figure 16. A HSRL calibration scan together with a simultaneous calibration from the atmosphere. Figure (a) shows a calibration from a thick water cloud (thin dashed line) together with a system calibration scan (thick solid line). In figures (c)-(d), the dashed line shows a clear air calibration at 3175 m (b), 5510 m (c), and 7550 m (d). The temperatures at these altitudes were -11 °C (b), -32 °C (c), and -45 °C (d), respectively. The long dashed line presents the expected molecular return. The measured calibration scan is presented as a reference (solid line).

5.2 The laser wavelength locking into the iodine absorption peak

The system calibration is sensitive to the drifts between the transmitter wavelength and the receiver bandpass transmission maximum. The measurements show that the seedlaser drifts at ~100 MHz/h rate. In order to achieve a stable long term operation without frequent calibrations, the wavelength of the transmitter laser is locked to the iodine absorption peak. Wavelength locking to the Doppler-broadened iodine absorption line was used because it requires much less power than a locking into a hyperfine structure of the iodine absorption line with Doppler-free technique[33]. Compared to the wavelength locking with a high resolution etalon, the advantage of the locking to an iodine absorption peak is that, iodine peak provides an absolute frequency reference. Another technique to lock the laser output wavelength to the Doppler-broadened iodine absorption line was reported by Arie and Byer[35]. They use Fourier transformation spectroscopy to lock the laser to the center of the Doppler-broadened peak. This method does not require any dither of the laser frequency, but it is more complex.

In the HSRL, the absorption spectrum of the 4 cm long iodine absorption cell is used to provide information about the absorption peak maximum. The absorption peak of the 43 long iodine absorption cell cannot be used as a reference for the wavelength locking because the saturation of the absorption at the peak causes the flat shape of the peak, and because the signal at the peak is small due to the strong absorption. Therefore it does not provide good photon counting statistics for the locking. The length of the reference cell is chosen so that the absorption is $\sim$ 50%. The cell transmission has to be high enough to provide a good photon counting statistics within a short averaging time.

The locking of the laser wavelength to the iodine absorption peak is performed by using an automatic controlling program that works as follows. First, the location of the absorption maximum is detected during a calibration scan. After completing the scan, the program automatically sets the seedlaser temperature to the observed peak. In order to keep the laser wavelength locked to the maximum absorption wavelength, the seedlaser temperature is dithered around the optimum temperature

and information about the ratio of signal from the second calibration fiber to the signal from the first calibration fiber detected with PMT 1 (see Figure 17) is gathered. The seedlaser temperature is kept at temperature that produces the minimum ratio. The basic idea of the tuning program is presented in the following.

The tuning procedure has four steps. First, information about the ratio between calibration fibers is gathered for the seedlaser temperature (T(peak)) that was detected to produce the minimum ratio. Then, a temperature T=T(peak)+dT is applied and the change in the ratio is observed. After gathering enough statistics ($\sim$ 30 s), the seedlaser temperature is returned back to the temperature T(peak) and a new value for the ratio at this temperature is measured. After this, the optimum temperature is detected by finding the temperature that produces the minimum ratio. If the temperature T=T(peak)+dT produced a smaller ratio, then that temperature becomes to the new optimum temperature T(peak). If the ratio for temperature T=T(peak)+dT was not better, the dithering to temperature T=T(peak)-dT is performed and the procedure is repeated. The wavelength dither corresponds to temperature change of 0.009 °C (0.052 pm). A time history of the dither temperatures for a 9 hour run shows that, the seedlaser temperature is dithered between 3 temperatures under typical operating conditions.

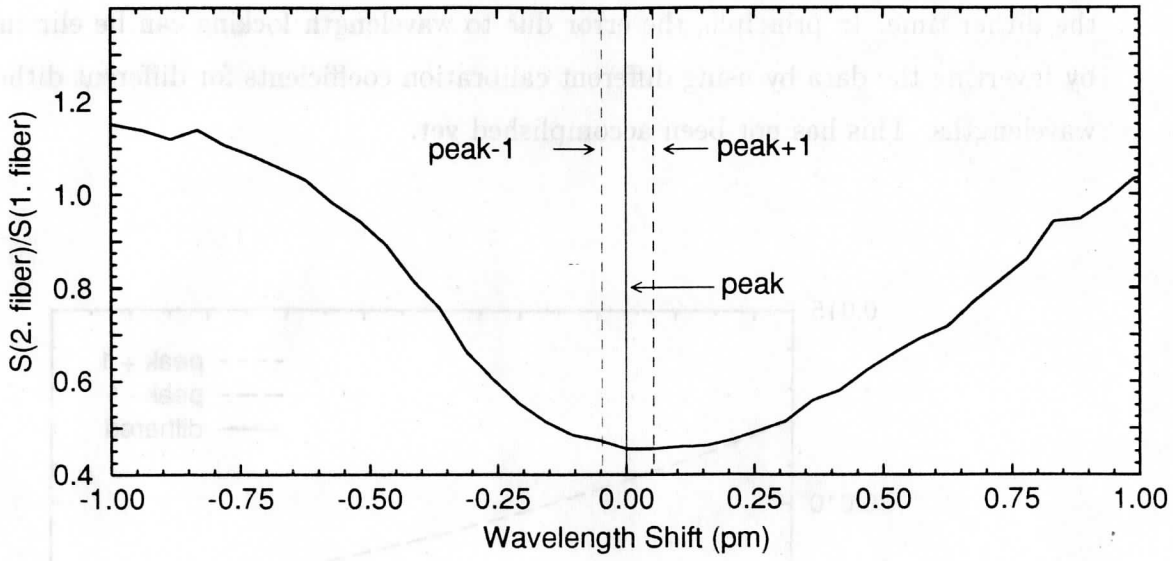

Figure 17. Signal for the frequency locking of the laser. An expanded view from the peak shows that as the temperature is changed in either direction from the detected peak, a change in the ratio is noticed.

Because the absorption peak of the 43 cm long absorption cell is flat around the maximum absorption wavelength, the error due to tuning to the amount of aerosol detected in the molecular channel (C_{am}) is comparable to the photon counting statistics. On the other hand, the error due to dithering to the amount of detected molecular signal in the molecular channel (C_{mm}) is a combination of photon counting statistics and the error between the convoluted signals at different dithering wavelengths. The errors in C_{mm} due to tuning as a function of atmospheric temperature are presented in Figure 18. Figure 18 shows the error in the determination of C_{mm}, when the laser wavelength is tuned off by ± 0.052 pm, but the calculation of C_{mm} is made for the peak wavelength. Also the error due to dithering is shown. The asymmetry of the absorption spectrum makes the errors due to the tuning asymmetric. The total effect of the tuning procedure to the measured profiles has to be calculated as a weighted average of the errors at different dithering wavelengths, because the tuning program is realized so that the laser spends 2/3 of the time at the wavelength that produces

the minimum ratio and 1/3 of the time doing the dithering. Therefore, the total error due to dithering is better than 0.1%, when measurement period is long compared to the dither time. In principle, the error due to wavelength locking can be eliminated by inverting the data by using different calibration coefficients for different dithering wavelengths. This has not been accomplished yet.

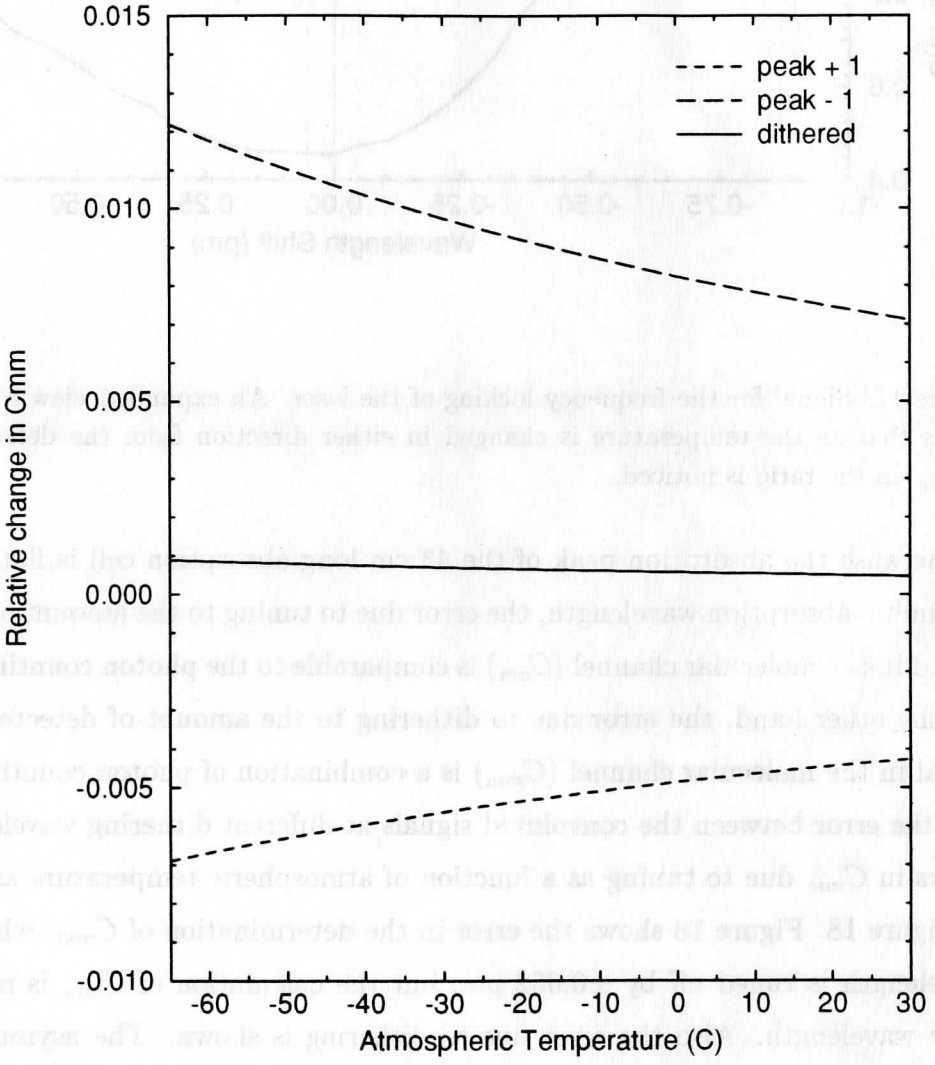

Figure 18. The errors in C_{mm} due to the tuning. Error when the seedlaser temperature is detuned from the optimum temperature by ± one step (0.009 °C) and when the seedlaser temperature is dithered, but the inversion is performed by using the observed peak value.

6 Measurements

Starting from July 1993, the iodine absorption filter based HSRL has been operated at the University of Wisconsin-Madison campus. During this time the HSRL has been routinely operated and the stability and reliability of the system have been tested. As a result, a dataset consisting of $\sim$ 30 different cirrus cloud cases has been obtained with a simultaneous NOAA-11 and/or NOAA-12 satellite overpasses. As an example from the data collected with the HSRL a dataset from November 11, 1993 is shown. This dataset contains a meteorologically interesting case: a cirrus cloud, supercooled water cloud, and ice crystal precipitation together with a strong low level aerosol structure. Figures 19 - 25 present Range Time Indicator (RTI) pictures from the data. Both raw and inverted data are shown along with depolarization and optical depth. The pictures are generated from the background corrected, energy normalized, and range square corrected data.

For the RTI's of the inverted data, the aerosol and molecular signals are separated by using Equations 19 and 20. The optical depth is obtained from the ratio of the inverted molecular profile to the return predicted for the pure molecular scattering (Eq. 10). The color scale shows the signal strength and the white areas are regions where the backscatter signal is larger than the maximum color scale value. The black areas indicate that the signal is smaller than the smallest color scale value.

The Figure 19 shows the raw lidar return detected with the combined aerosol and molecular channel. This profile is similar to the profile obtained with a conventional single channel lidar: the signal from small amounts of aerosol scatterers is dominated by the scattering from molecules, and therefore all aerosol structures are not clearly visible. The ability of the HSRL to separate aerosol and molecular scattering can be seen from the RTI picture of the inverted aerosol signal Figure 20. After inversion, the aerosol structures are more visible and they do not have the decrease with altitude caused by the atmospheric density profile. The ability of the iodine absorption filter to reject aerosol scattering is visible from the RTI of the raw molecular signal (see Figure 21): only a small aerosol cross-talk for the densest parts of the clouds is observed and this is easily removed by the inversion, as can be seen from Figure 22. The phase of the water at different layers can be seen from the depolarization RTI's. Figure

23 shows the raw depolarization observed with the combined aerosol and molecular channel. The inverted aerosol depolarization is shown in the Figure 24. From these pictures, a cirrus cloud at $\sim$ 8 km (depolarization ratio $\sim$ 40%) and a supercooled water cloud at 5 km (depolarization ratio $\sim$ 1 %) with ice crystal precipitation can be easily separated. For low level aerosols (0-3.7 km), a two layer polarization structure is seen. The small increase in water cloud depolarization as a function of cloud height is an indicator of multiple scattering. The low molecular depolarization is presented in Figure 25. The low depolarization ratio values with small signal to noise ratio show up in the picture as noise.

The optical depths on the different parts of the data set can be seen from the Figure 26. The optical depth of the cirrus cloud between 7 and 10 km is $\sim$ 0.4. The water cloud at $\sim$ 5 km has an optical depth of 2.5-3. The extinction through the ice crystal precipitation below the water cloud and the extinction through the water cloud can be seen as a change in the color scale as a function of altitude. The optical depth of the ice crystal precipitation is $\sim$ 0.1.

A more detailed analysis of the dataset is presented in the following sections. First, the depolarization measurements are discussed in Chapter 7.1. The effects of multiple scattering to the depolarization measurements are shown. The measurements of the cloud particle sizes are not included to this study. The depolarization data from August to November 1993 is analyzed and a summary from the observed depolarizations as a function of atmospheric temperature is given. Second, an example from a measurement of scattering ratio, aerosol backscatter cross section, and optical depth is given together with error estimates for the optical depths (see Chapter 7.2). The temperature dependence of the Doppler-broadened molecular spectrum enables the measurements of the atmospheric temperature by the HSRL. Preliminary results from a temperature measurement are presented in Chapter 7.4.

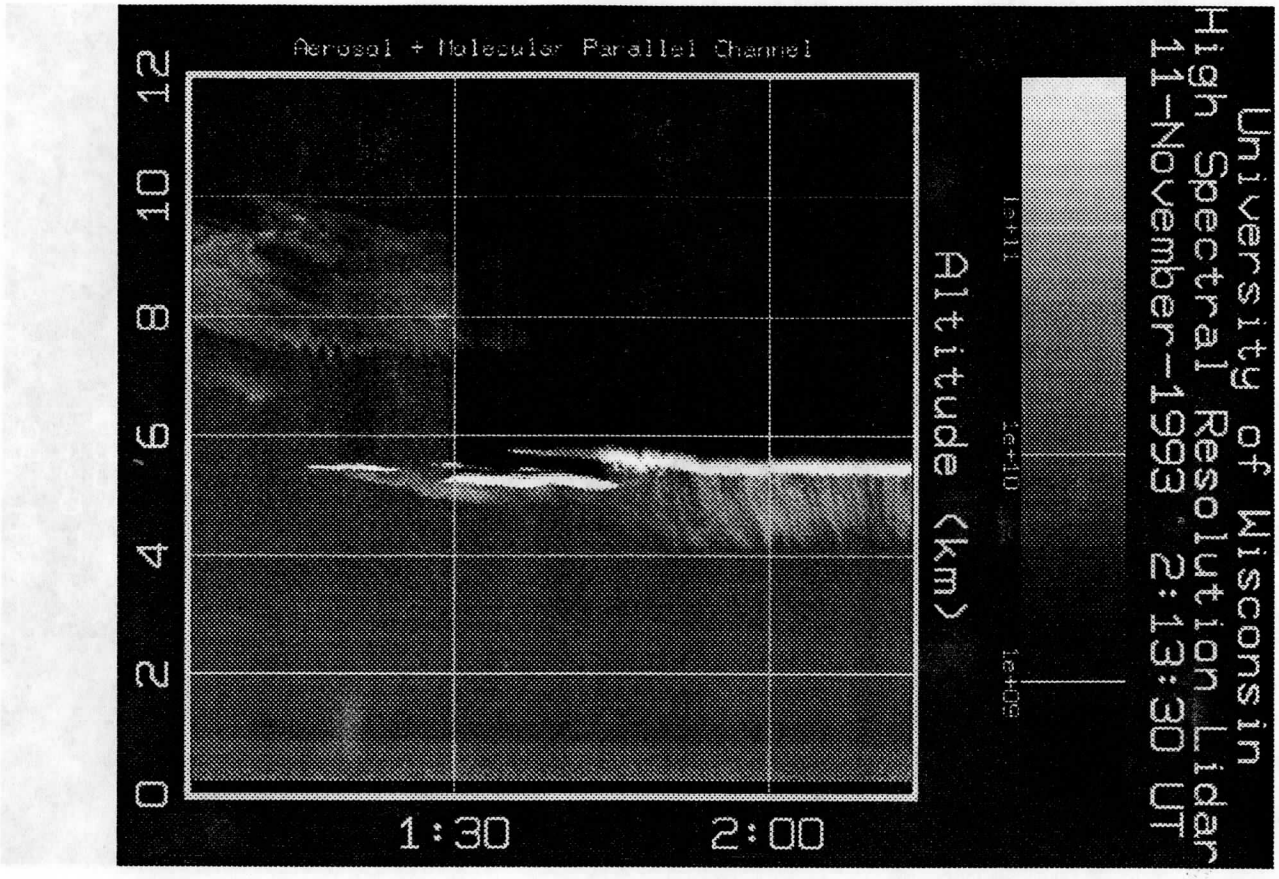

Figure 19. The raw lidar return presenting the combined aerosol and molecular channel return. A water cloud layer with an ice crystal precipitation are seen at 5 km. Above the water cloud, a cirrus cloud can be seen. The low level aerosol structure between 0 and 3.7 km is hardly visible because it is damped by the molecular backscatter signal.

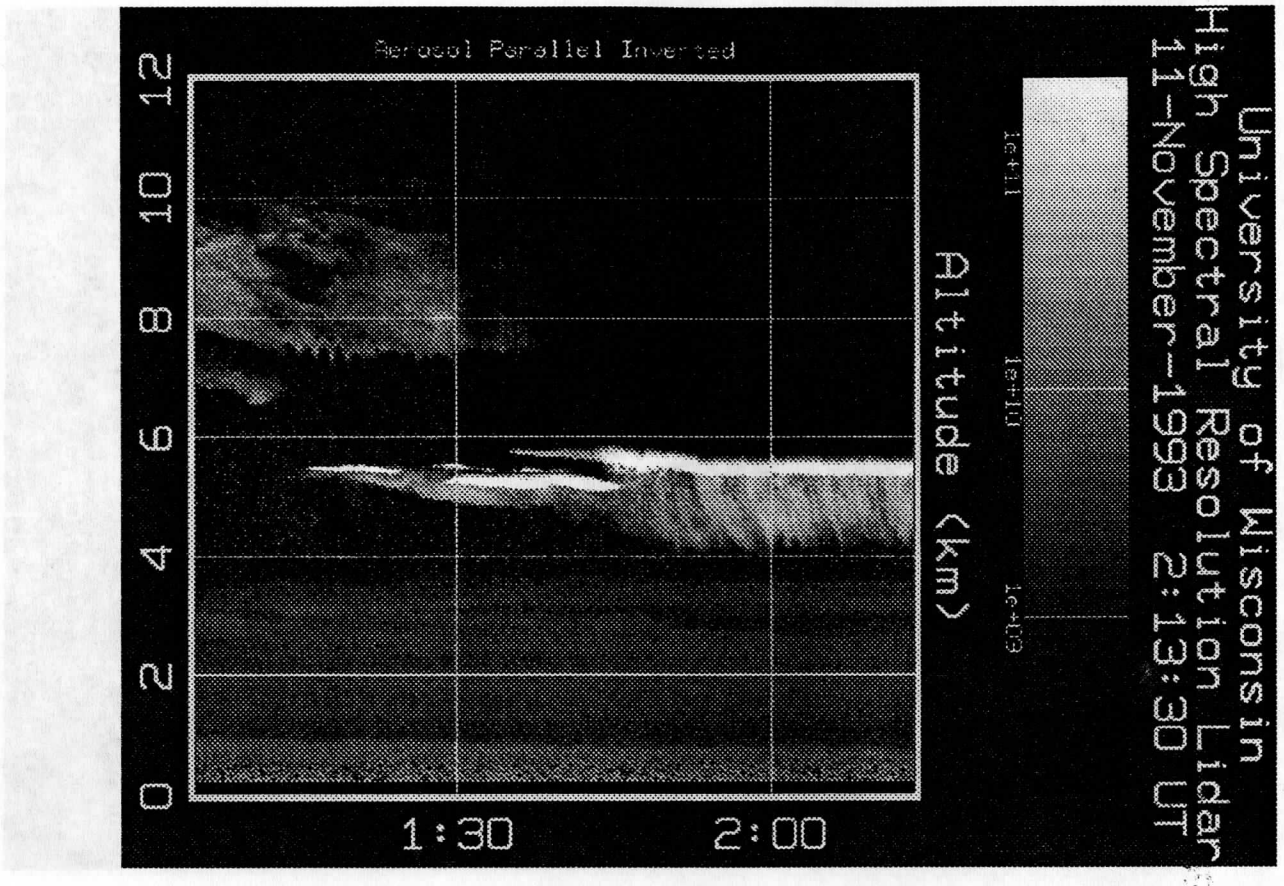

Figure 20. The inverted aerosol profile. After separating the aerosol and molecular backscatter returns, the layers where the aerosol backscatter signal is small compared to the molecular signal are clearly visible. The largest difference is seen for the low level aerosol layer between 0 and 3.7 km.

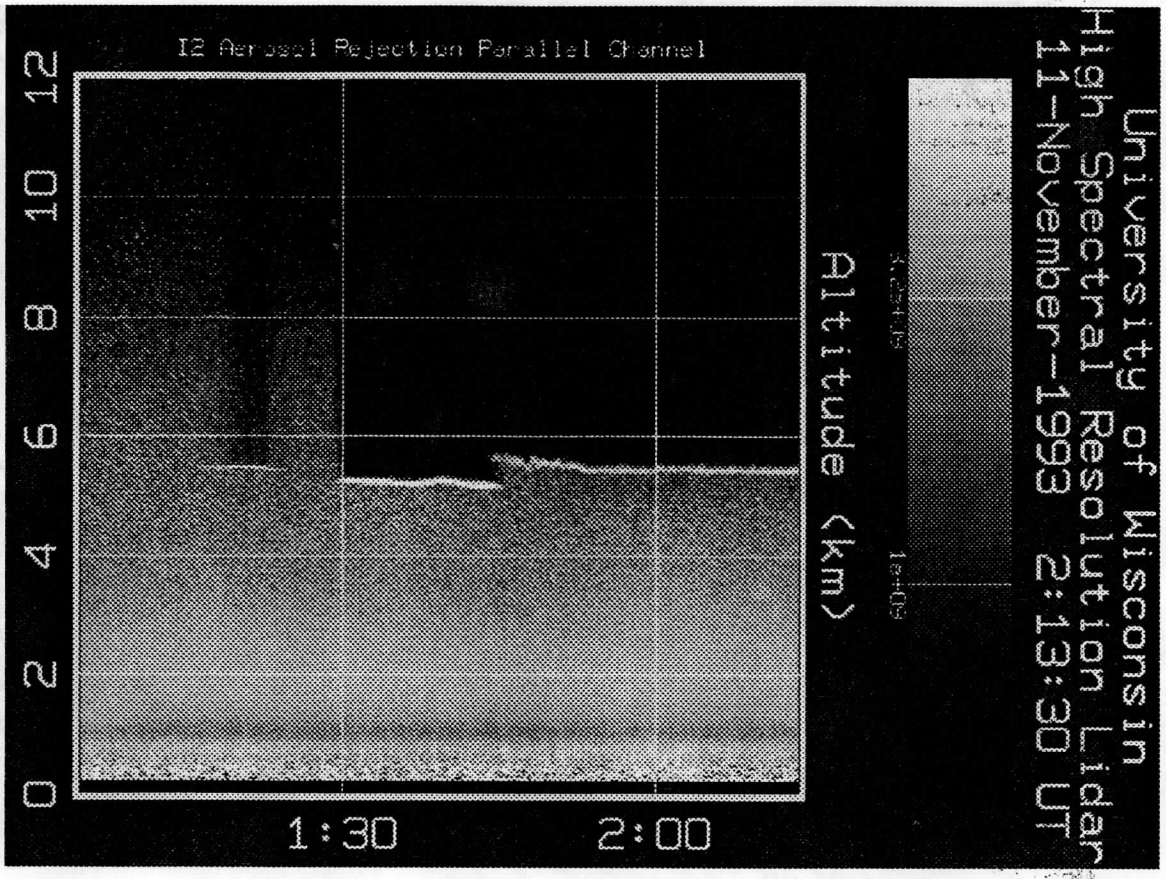

Figure 21. The raw molecular return. A small aerosol cross talk signal is visible for the densest parts of the water cloud at $\sim$ 5.5 km. The dark areas indicate that very little or no return through parts of the water cloud is observed.

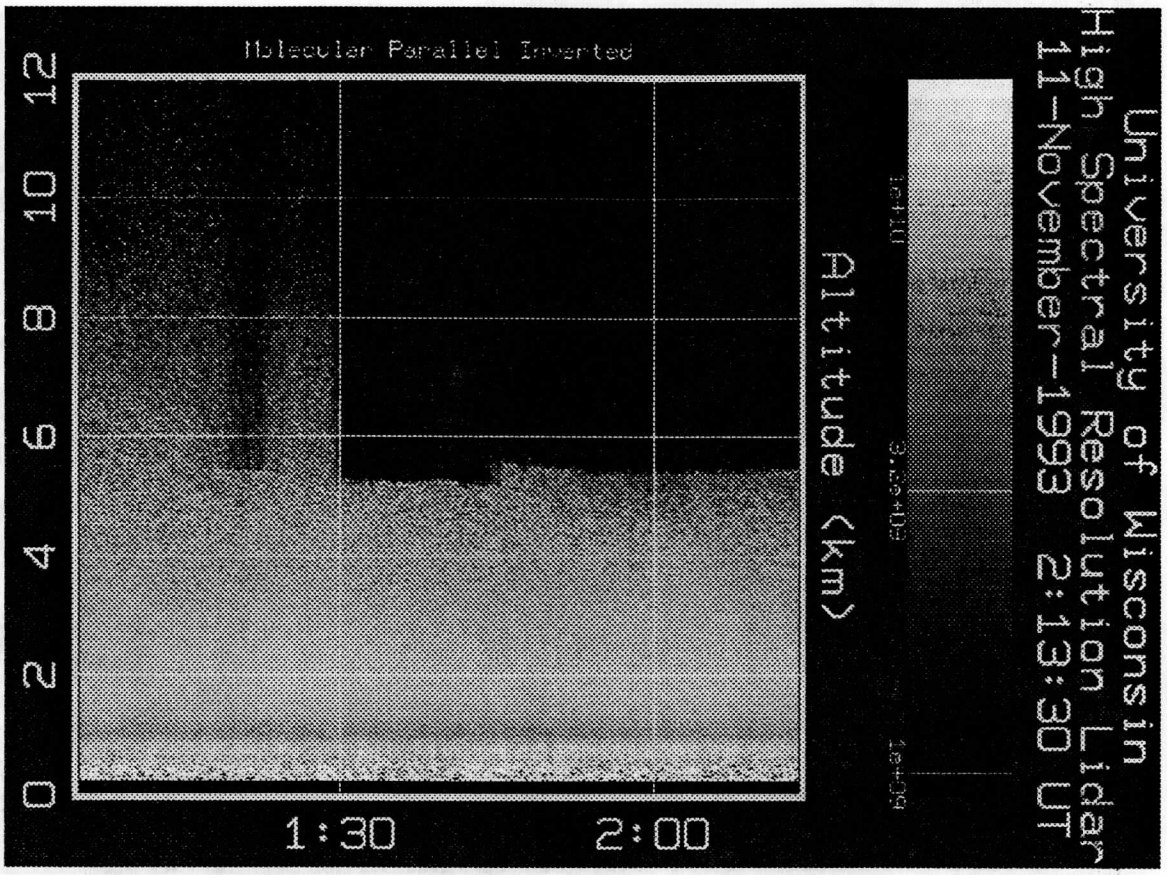

Figure 22. The inverted molecular profile. After the inversion, the cross talk that was visible in Figure 21 cannot be seen and the inverted molecular profile therefore presents the atmospheric extinction at various points of the dataset. The inaccuracy of the overlap correction can be seen as a darker line at $\sim$ 1 km.

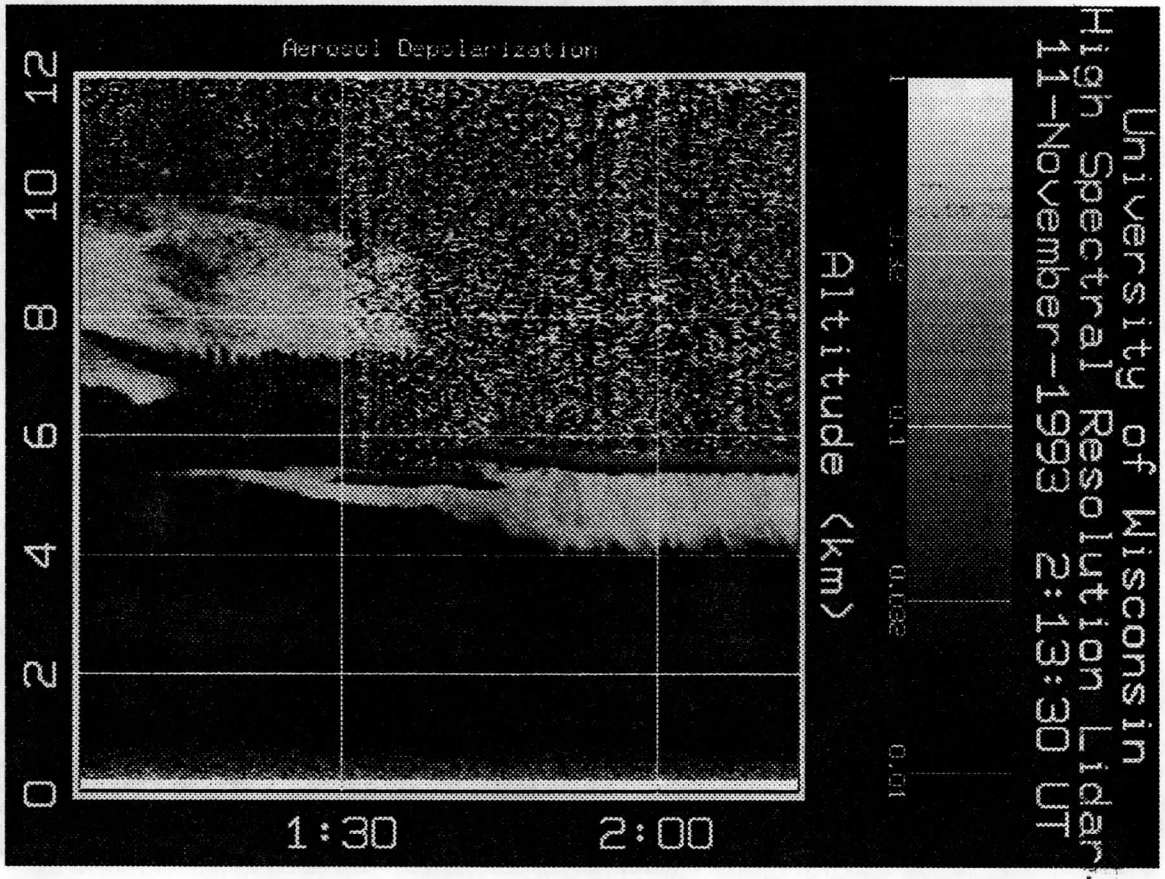

Figure 23. The raw aerosol depolarization combined with the molecular depolarization. The picture shows the depolarization ratio that is seen with a lidar that cannot separate the aerosol and molecular backscatter signals. The depolarizations for altitudes with low aerosol content are dominated by the molecular depolarization. The parts of the cirrus cloud and parts of the ice crystal precipitation between 4 and 5.5 km show depolarization ratios that are $\sim$ 10%, and those layers could be expected to contain mixture of ice and water. Some parts of aerosol layer between 2 and 3.7 km show depolarization of $\sim$3.5 %. The water cloud at 5.5 km has $\sim$1% depolarization. The increase in the water cloud depolarization as a function of altitude is due to the multiple scattering.

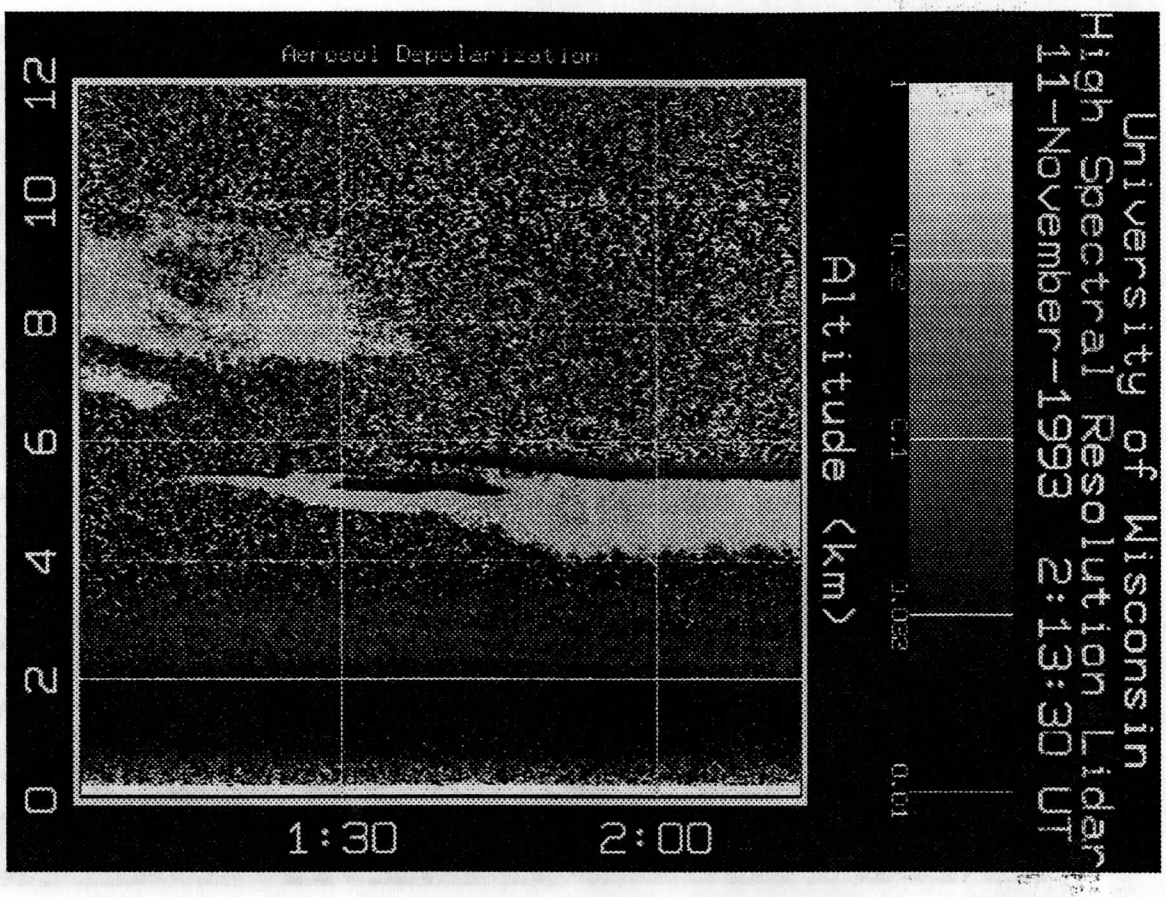

Figure 24. The inverted aerosol depolarization. After inversion, the cirrus cloud depolarization of $\sim$ 40% indicates pure ice depolarization. The ice crystal precipitation falling out from the water cloud show similar depolarizations values. The low level aerosol structure shows a two layer polarization structure. A $\sim$1% depolarization ratio for the layer between 0.5-2 km is observed indicating nearly spherical particles. The depolarization of the layer between 2 and 3.7 km shows a $\sim$ 5% depolarization.

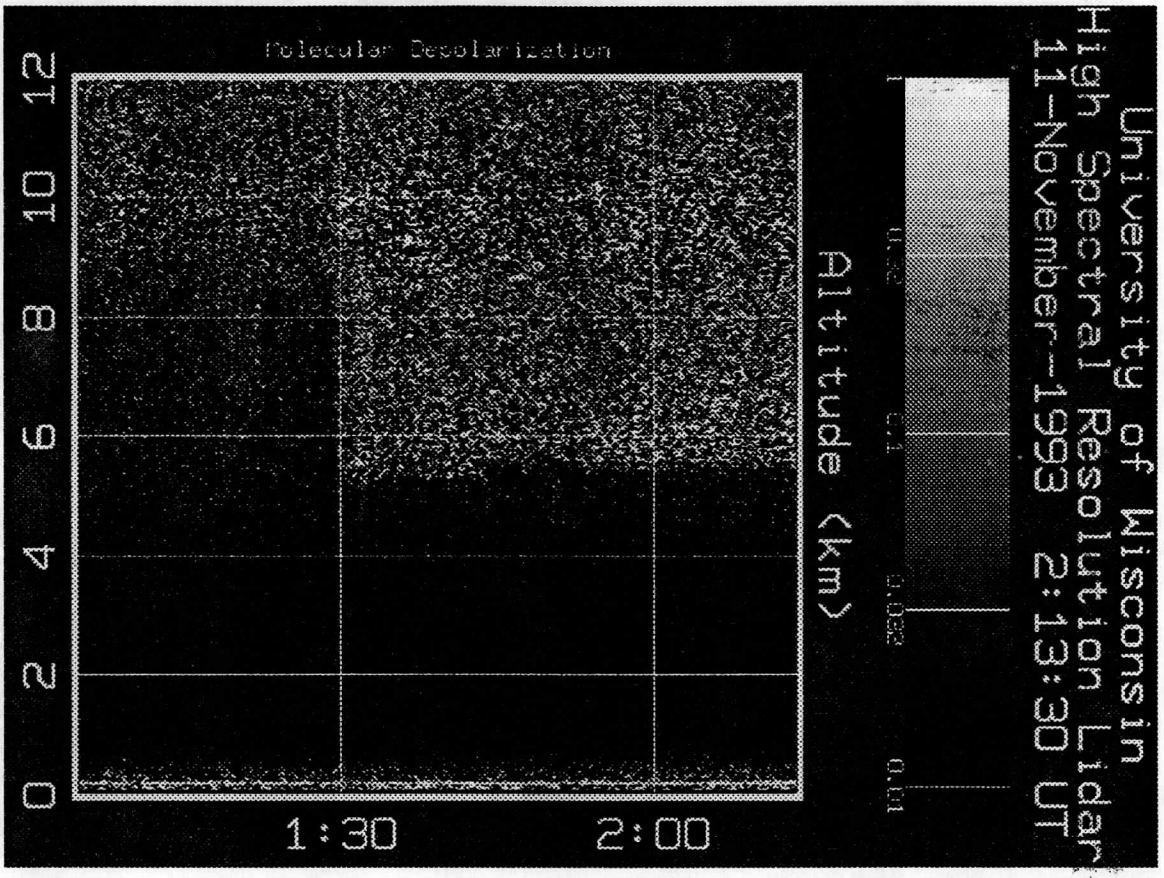

Figure 25. The inverted molecular depolarization. A less than 1% molecular depolarization is observed. The increase in the depolarization variations at the higher altitude is due to the low signal to noise ratio.

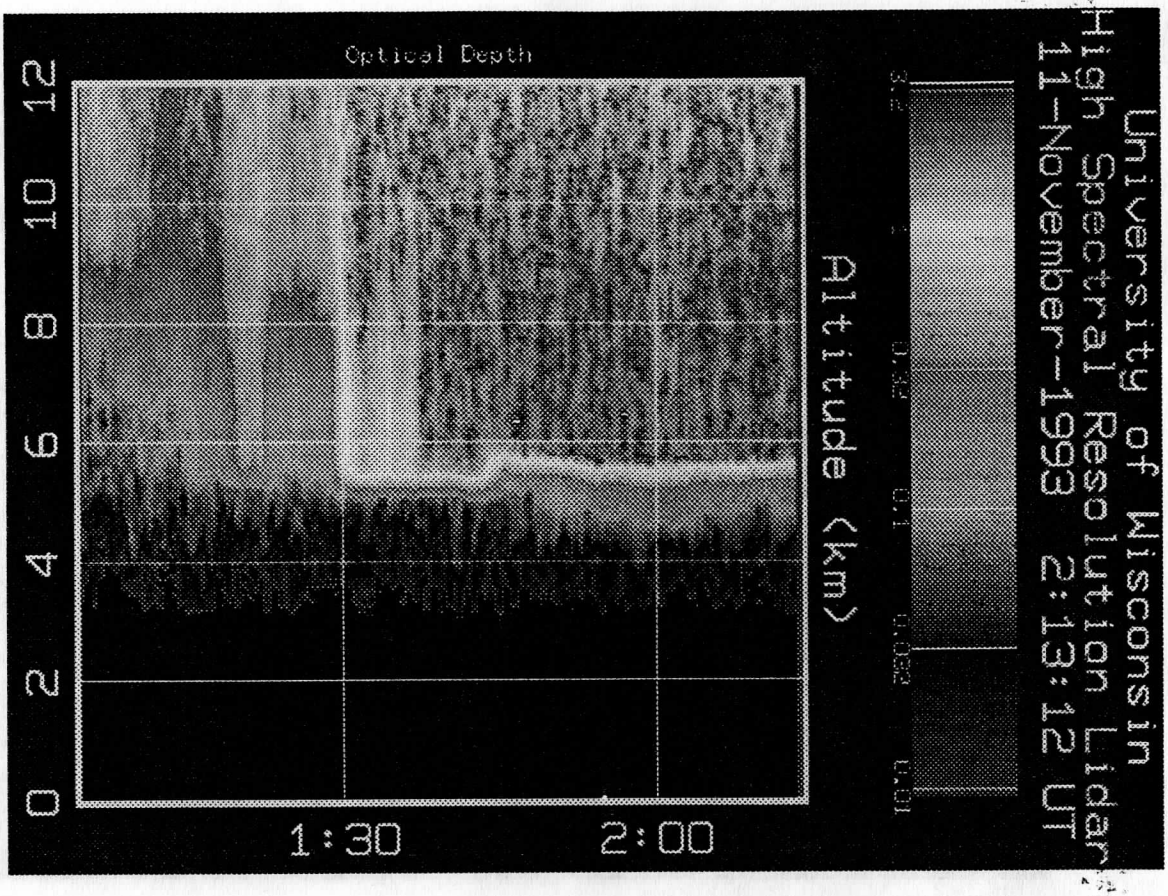

Figure 26. The optical depth. The optical depth above 3 km is shown. The optical depth of the cirrus cloud between 7 and 10 km is ~ 0.4. The water cloud at ~ 5 km has a optical depth of 2.5-3. The extinction through the ice crystal precipitation below the water cloud and the extinction through the water cloud can be seen as a change in the color scale. The optical depth of the ice crystal precipitation is ~ 0.1.

6.1 Depolarization ratio

Lidar measurements of atmospheric depolarization can be used to distinguish between liquid and solid phases of water in the atmosphere[36–38]. The quantity to describe the degree of polarization is the linear depolarization ratio δ

$$\delta = \frac{I_\perp}{I_\parallel}, \tag{23}$$

where $I_\perp$ and $I_\parallel$ are the measured perpendicular and parallel backscatter intensities in respect to the transmitter polarization axis. The backscatter signal of a linearly polarized laser beam from spherical particles is totally linearly polarized ($\delta = 0$). The particles can be assumed to be spherical in case of wet haze, fog, cloud droplets, and small raindrops. The depolarization of the pure molecular atmosphere is nonzero, because of the anisotropy of the air, and therefore a 0.37–0.4 % depolarization for the Cabannes line is expected[39,40]. The depolarization of the molecular return that includes the Cabannes line and the rotational Raman lines is $\sim 1.5\%$[40]. If particles are nonspherical (as ice crystals, snow flakes or dust particles) or if the backscatter signal has a multiple scattering contribution, the backscattered signal contains a cross-polarized component ($0 < \delta < 1$). A specular reflection from a oriented ice crystal layer provides a small depolarization, which therefore can be misinterpreted as the backscatter signal from a water cloud, but the off vertical pointing direction of the HSRL is expected to prevent this.

Lidar studies of atmospheric polarization have been traditionally based on a technique, where a linearly polarized laser beam is sent to the atmosphere and the received polarization components are separated by a polarization cube and detected by a pair a photomultiplier tubes, one for each polarization component. This method requires a precise calibration of the receiver in order to avoid the problems due to differences between channels in optics, and in photomultiplier sensitivity.

In the new HSRL (see Figs. 5 and 6), the polarization measurements are made by using one transmitter laser and one detector for both polarization components. The transmitted laser beam is linearly polarized, and for polarization measurements the polarization of the transmitted laser beam is rotated by 90 degrees on alternative laser pulses by a Pockels cell. In the receiver, the signal parallel to the transmitter

polarization axis and the signal perpendicular to that are separated and cleaned by a polarization cube pair. Since the polarization of the transmitted laser shot alternates between two subsequent laser shots, the same detector can accurately measure both polarization components and therefore no calibration of the receiver is required. The 250 μs time separation between laser pulses insures, that both depolarization components are measured from the same atmospheric scatterers. The depolarization variations as a function of field of view can be studied with the new WFOV-channel. The effects of specular reflection from a horizontally oriented crystal layer are minimized by tilting the receiver by 4 degrees from the zenith. With the HSRL, separate measurements of aerosol and molecular depolarizations can be made.

Depolarization measurements are affected by presence of multiple scattering when a lidar is used to probe dense clouds. Because the amount of detected multiple scattering is dependent from the cloud particle size, range from the cloud, optical depth of the cloud, and the field of view of the system, typical systems with 1-5 mrad field of views have difficulties separating between water and ice for dense clouds. In order to separate between water and ice for optically thick clouds, the HSRL uses a 160 μrad field of view for the spectrometer channels.

Figure 27 represents an example of the multiple scattering effect on the measured depolarization. Figure 27.a. shows the measured energy and range square corrected signals from a supercooled water cloud with ice precipitation. For the WFOV-channels, 0.22, 0.65, 1.1, and 1.6 mrad field of views are used. The WFOV-channel measurements are then compared to the measurements of the 0.16 mrad field of view channels. The amount of multiple scattering in the signal is calculated from the ratio of the WFOV-signal to the signal simultaneously measured with the narrow field of view channel (see Figure 27.b.). Figure 27.c shows the depolarization ratios for different field of views and the Figure 27.d shows the ratio of the WFOV depolarization to the narrow field of view depolarization. For the optically thin ice crystal precipitation layer, the change in depolarization as a function of field of view is hardly noticeable. The change from ice to water shows up as a drop in the depolarization ratio. All field of views show a low depolarization for the water cloud base but as soon as the signal penetrates deeper into the cloud, an increase in the depolarization

as a function of field of view can be observed. Inside 300 m the multiple scattering effects in the cloud will increase the depolarization of the larger field of views up to the level which is comparable with the observed ice crystal depolarization and therefore, the separation between ice and water becomes impossible. The low values of depolarization observed with the narrow field of view channel and with the smallest WFOV field of view show that the narrow field of view effectively suppresses the effects of multiple scattering. Therefore, the HSRL signals from these field of views can be used to separate between ice and water clouds even for optically thick clouds. On the other hand, information from depolarization and signal strength variations as a function of field of view can be used to verify multiple scattering calculations.

Theoretically, the depolarization of the spherical dropplets should be zero, but the depolarization ratios observed for the water cloud at 5.5 km is ~2 %. In the cases of water clouds with an ice crystal precipitation, the non-zero values of depolarization ratio can be explained by the presence of ice. Because the water cloud is precipitating ice, there has to be some ice mixed with water in the cloud. The scattering from the cloud base is $\sim$ 20 times larger than signal from ice crystal precipitation. Based on this ratio, $\sim$ 2 % ($\sim$ 1/20 x ice depolarization of 40 %) depolarization for the cloud base depolarization can be expected due to the presence of ice crystals with $\sim$ 40 % depolarization.

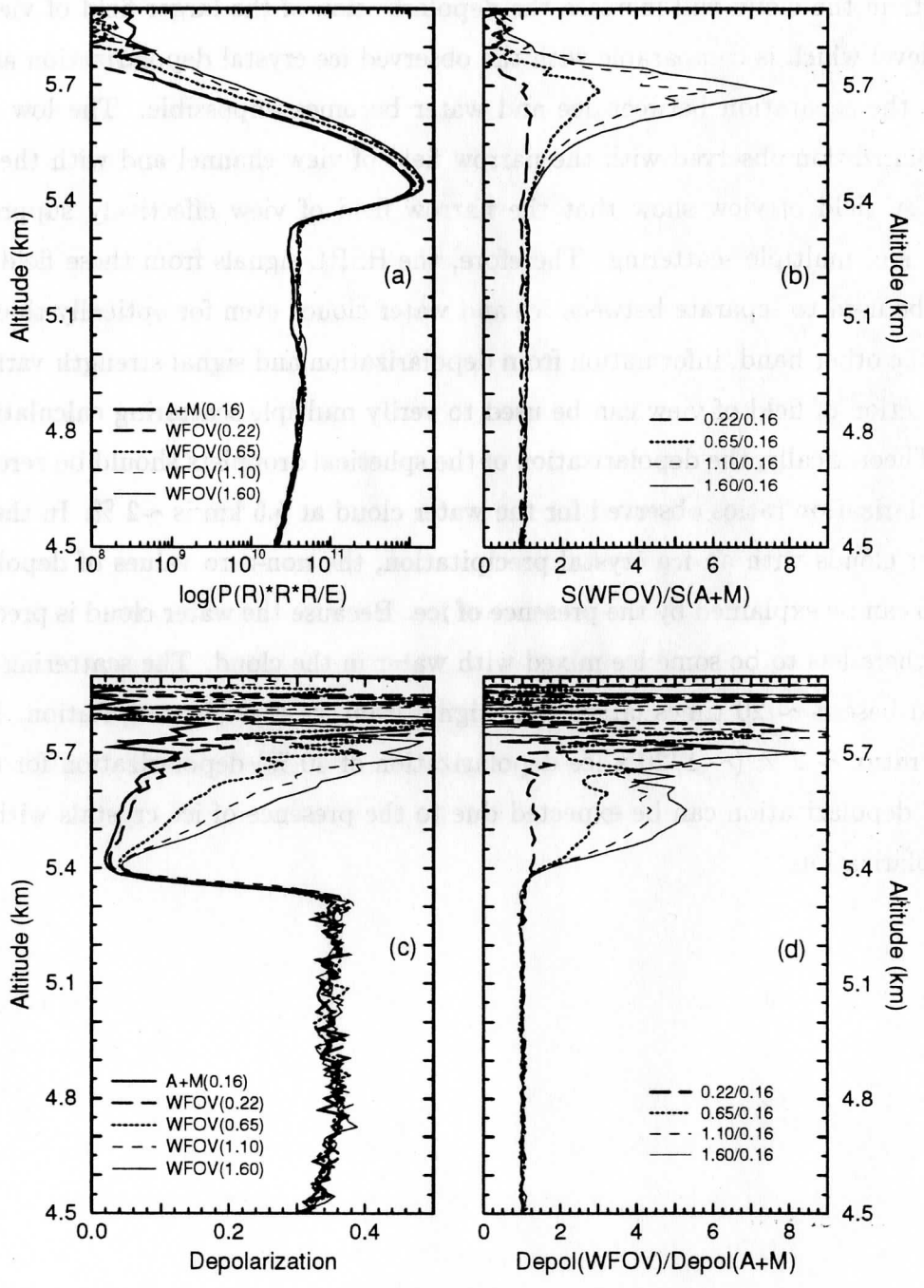

Figure 27. Effects of multiple scattering on depolarization in the backscatter return from a water cloud at 5.5 km with ice crystal precipitation between 4.5 and 5.3 km. Data obtained on November 11, 1993 02:04-02:14 UT. (a) Measured signals. (b) Ratios of measured WFOV signals to 0.16 mrad field of view signal. (c) Measured depolarization ratios. The cloud base depolarization of the smallest field of view at 5.4 km is $\sim$ 2 %. (d) Ratios of the measured WFOV depolarizations to the depolarization of the 0.16 mrad field of view channel.

The capability of the HSRL to distinguish between aerosol and molecular scattering allows separate polarization measurements. This is important when layers with a low aerosol content are studied. The effects of the molecular scattering on the observed depolarization can be seen by comparing the raw and inverted aerosol depolarization ratios. For the cases where the amount of aerosol scatterers is small, the signal from molecular scattering dominates the depolarization picture (see Figure 23). Therefore, aerosol depolarizations similar to the molecular depolarization can be seen and also parts of the cirrus cloud and ice crystal precipitation show depolarization ratios which are close to the depolarization of the supercooled water or mixture of ice and water (green areas in the raw aerosol depolarization RTI). After inversion a clear difference in the depolarizations is seen: the depolarization of the low level aerosols is better defined and the depolarization of the cirrus shows that the cloud contains pure ice crystals (Figure 24). Therefore, a clear separation between ice and water can be based to the depolarization ratios calculated from the inverted aerosol profiles. The effect of the inversion to the depolarization ratio is also visible from the Figures 28 – 29.

The profile of the raw aerosol depolarization shows the depolarization of the combined aerosol+molecular channel and therefore, it shows the depolarization ratio which is seen with a conventional single channel lidar. The raw molecular depolarization contains the depolarization component of the aerosol cross talk together with the molecular depolarization. In the same figure, the separated aerosol and molecular signals are shown with the inverted aerosol and molecular depolarizations. Figure 28 shows a two layer water cloud with an ice crystal precipitation. The peaks of the water clouds are observed at 5.2 and 5.6 km and the corresponding low depolarization values are 1–2 %. A small increase in the depolarization with penetration depth is observed. The values of raw depolarization of the ice crystal precipitation are close to those of water and ice mixture, but the inverted depolarization ratios show a clear ice depolarization. After inversion the increase in aerosol depolarization at 2–3.7 km is also very clear. The Figure 29 shows a water cloud layer at 5.4 km with a more dense ice crystal precipitation. With increased backscatter signal from ice, the value of raw depolarization ratio indicates clear ice and therefore the effects of molecular

depolarization do not show up so clearly, eventhough a change in depolarization ratio is observed after the inversion.

The depolarization observed in the clear air is 0.7–0.8 %, when the observations are made without the low resolution etalons. When the low resolution etalons are used, the depolarization is 0.55–0.6 %. The expected value for the molecular depolarization of the Cabannes line is $\sim$ 0.4 and $\sim$ 1.44 for the Cabannes line[39,40] and rotational Raman lines[40]. The HSRL observations show a 1.5 % depolarization for the signal from the rotational Raman lines and Cabannes line. Because the system filter bandpass admits a small fraction of the rotational Raman lines (75 % depolarization) and simultaneously blocks part of the Cabannes line, the molecular depolarization value measured by the HSRL is larger than the expected Cabannes line depolarization. The amount of transmitted rotational Raman signal is temperature dependent. A model to calculate the expected depolarization was written. This model includes the rotational Raman spectrum for nitrogen and oxygen, molecular spectrum including effects of Brillouin scattering, and spectral transmissions of different filters. The polarization that correspond to different atmospheric temperatures can be calculated. The ratio of rotational Raman signal to Rayleigh signal is chosen so, that a 1.44 % depolarization for the clear air is observed. These calculations show, that a 0.56 –0.62 % depolarization is expected for the case where no low resolution etalons were used. A 0.402 –0.425 % depolarization is expected, when one or two etalon are used. The depolarization observed with the HSRL are larger than the expected values. The cause of the additional depolarization in the HSRL measurements is currently unknown.

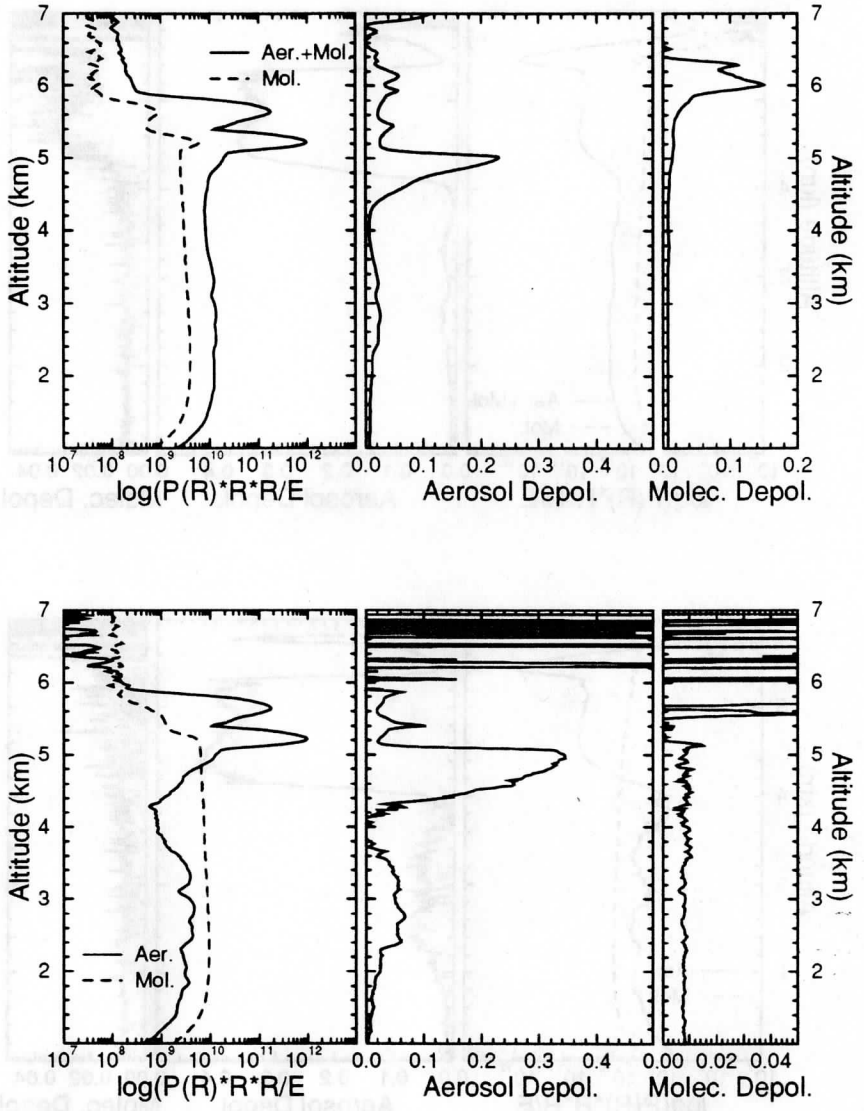

Figure 28. Raw and inverted depolarization ratios of clear atmosphere with ice crystal precipitation and two water cloud layers above it (November 11,1993 01:35-01:47 UT). The upper set shows the raw aerosol and raw molecular profiles together with the depolarizations. The lower set shows the inverted profiles with the inverted depolarizations. The water clouds are observed at 5.2 and 5.6 km altitudes. The low water cloud depolarization values can be observed from the aerosol depolarization figures. The small increase in water cloud depolarization as a function of penetration depth is due to the multiple scattering. The weak signal from the ice crystal precipitation is visible 4.3-5.1 km. Because of the low ice crystal content, the raw depolarization ratios of the ice crystal precipitation shows values that would indicate mixed phase, but after the inversion a clear ice crystal depolarization is visible. The clear air aerosol depolarization is less than 6%. The observed molecular depolarization is 0.8 %.

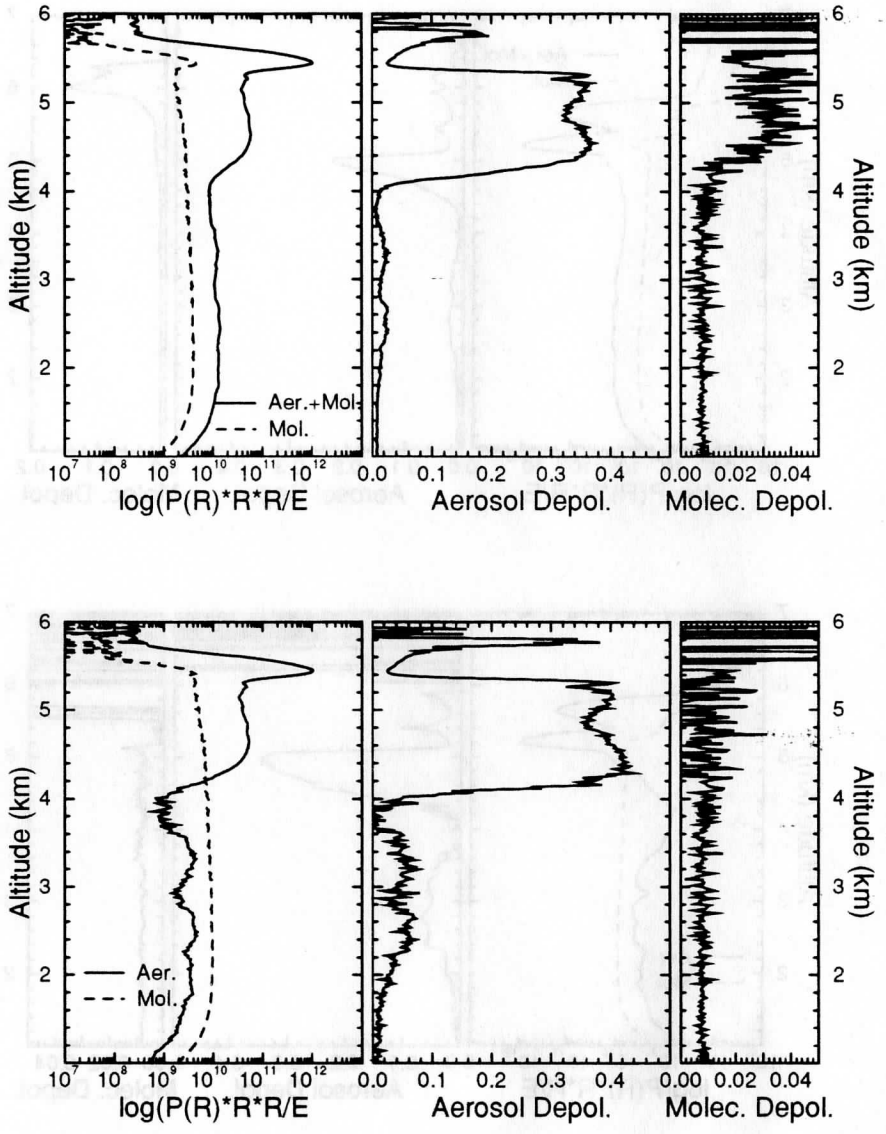

Figure 29. Raw and inverted depolarization ratios of a thin cirrus cloud and a thin water cloud with an ice crystal precipitation (November 11,1993 01:55-02:01 UT). The upper set shows the raw aerosol and molecular profiles along with the raw depolarization ratios. The lower set shows the inverted profiles with the inverted depolarization ratios. The water cloud at 5.5 km has a low depolarization value ~1.5% at the cloud base and it increases towards the cloud top due to the multiple scattering. The dense ice crystal precipitation is visible between 4 and 5.4 km. Because the ice crystal content of the precipitation is large compared to the molecular backscatter, only small difference between raw and inverted aerosol depolarizations is observed. The raw molecular depolarization shows a small increase for the cloud, but after the inversion a constant 0.8% depolarization is observed.

The depolarization data for cirrus clouds obtained between August and November 1993 have been analyzed. A summary of the observed depolarization ratios as a function of temperature are presented in Figure 30. In this study only clouds with scattering ratios greater than 0.5 were used. This was made in order to fully separate cloud depolarizations from noisy clear air depolarizations. The values of clear air depolarizations are low and affected by the photon counting statistics. Because the HSRL measurements have shown, that the scattering ratios of clear air aerosol and stratospheric aerosols can exceed values 1-3, the use of the scattering ratio of 0.5 does not guarantee a clear separation between clouds and clear air aerosols. On the other hand, the scattering ratios of the cirrus clouds can be below 1. Therefore, a visual separation between cirrus clouds and clear air aerosols is made and only the cloud altitudes are included to the study. In this study, 2 min averaging times for the data were used. By using a short averaging time, the errors due to temporal changes of the atmosphere were minimized. The atmospheric temperatures were obtained from radiosonde measurements and temperature intervals of 5 °C were used. Water clouds at cirrus cloud altitudes were separated from ice clouds based on the depolarization ratio values. Clouds with depolarization ratio values less than 15 % were classified as water clouds.

The high depolarization values of the cirrus clouds are easily separable from the water cloud depolarizations. The average cirrus cloud depolarization varies from 33% to 41% showing an increase towards the colder temperatures. Part of this can be expected to be from different shape, size, and orientation of the ice crystals at different temperatures[41,42]. The size and shape of the ice crystals have been found to be different at different temperatures and the crystals have been found to have a preferred orientation. A similar increase in cloud depolarization towards colder temperature was observed by Platt *et al.*[43]. His study was made for midlatitude and tropical cirrus and the depolarization values for temperatures from -30°C to -10 °C were lower, ranging from ~0.15 to ~ 0.25. The cirrus cloud depolarizations measured with the HSRL do not show any depolarization values below 20% for the temperatures from -30 to -10 °C. The system used by Platt had a 2.5 mrad field of view, and the low depolarization values are possibly caused by multiple scattering from water

clouds. The HSRL measurements have shown that when the depolarization of a water cloud is measured with a system with $\sim$ 1.0 mrad field of view, the effects of multiple scattering are large enough to cause depolarization values of $\sim$ 20%, and therefore the separation between water and ice becomes impossible. Also the HSRL measurements show a substantial probability of observing water at temperatures from -30 to 0 °C.

In 45% of the cases simultaneous observations of water cloud layers at the cirrus cloud altitudes were made. The Figure 30 shows, that supercooled water clouds at cirrus cloud altitudes are found at temperatures as low as -35 °C. Above 0°C temperature the low depolarization values indicate pure water, and the presence of cirrus disappears. The water cloud depolarizations are below 10 % and they contain the effects of multiple scattering. When the same clouds are studied with a NOAA-11 or NOAA-12 satellite, the simultaneous appearance of the water and ice cannot be noticed. On the satellite measurements, the cloud types are separated by using the information on the temperature. Therefore, if satellite data is used for cirrus optical depth studies, a supercooled water cloud layer mixed with ice cannot be easily separated and water will increase the optical depth value determined for the cirrus cloud. The depolarization ratio knowledge of the cloud measured with a lidar can be used to separate the water from ice and therefore separate optical depth measurements for both constituents can be performed.

The initial measurements have shown that the HSRL is capable of measuring cirrus cloud particle sizes. These measurements together with phase function measurements can be used for further studies of the cloud particle size effects on the depolarization ratio[26].

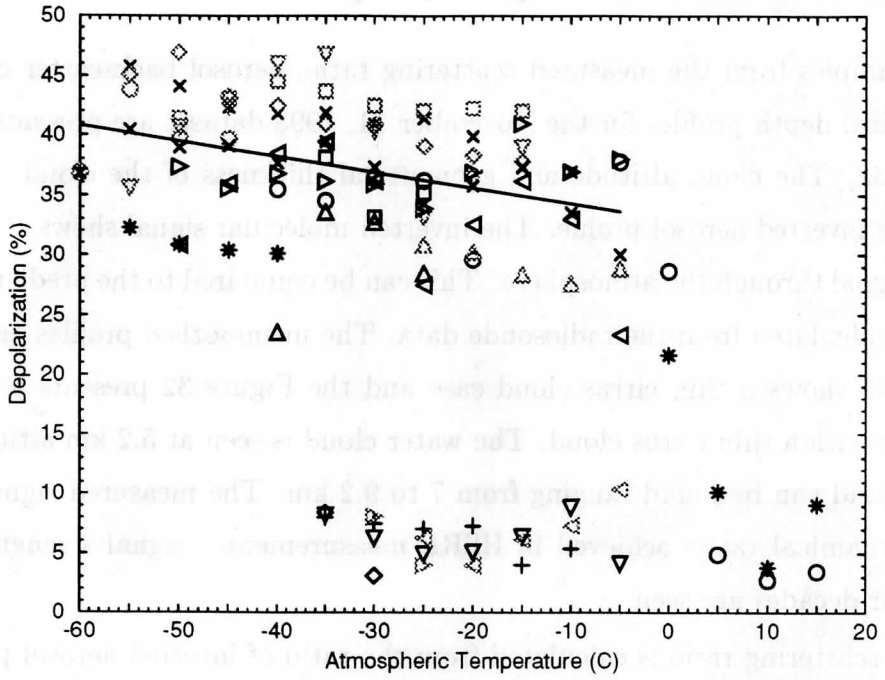

Figure 30. Cirrus cloud and supercooled water cloud depolarization as a function of temperature observed between August 2 and November 11, 1993. The depolarization values below 10% are indication of water clouds and higher depolarization values indicate the presence of ice.

6.2 Measurements of scattering ratio, aerosol backscatter cross section, and optical depth

Two examples from the measured scattering ratio, aerosol backscatter cross section and optical depth profiles for the November 11, 1993 dataset are presented in figures 31 and 32. The cloud altitude and geometrical thickness of the clouds can be seen from the inverted aerosol profile. The inverted molecular signal shows the extinction in the signal through the atmosphere. This can be compared to the predicted Rayleigh return, calculated from the radiosonde data. The unsmoothed profiles are used. The Figure 31 shows a thin cirrus cloud case and the Figure 32 presents a water cloud together with a thin cirrus cloud. The water cloud is seen at 5.2 km altitude and the cirrus cloud can be found ranging from 7 to 9.2 km. The measured signals show the large dynamical range achieved in HSRL measurements: signal strength variations over four decades are seen.

The scattering ratio is calculated from the ratio of inverted aerosol profile to the inverted molecular profile. The measured scattering ratios for the whole dataset vary from $\sim 10^{-3}$ to $\sim$1000. The maximum scattering ratio is 10 for the case presented in Figure 31 and $\sim$300 for the water cloud case in Figure 32.

The aerosol backscatter cross section is obtained from the scattering ratio and an estimate for the atmospheric density profile. The values of aerosol backscatter cross section change from $\sim 10^{-6} m^{-1} sr^{-1}$ for cirrus and ice precipitation to $\sim 10^{-4} m^{-1} sr^{-1}$ for water cloud. The observed aerosol backscatter values of the clear air are between 10^{-6} and $10^{-7} m^{-1} sr^{-1}$.

The total optical depths are calculated from the ratio of the inverted molecular signal to the return predicted for the pure molecular scattering. They range from 0.5 to 2.5 for this dataset. The Figure 31 shows a optical depth of 0.5 for the cirrus cloud and a optical depth 1.4 is observed for the case in Figure 32. The water cloud optical depth is 1 and the cirrus cloud gives an optical depth of 0.4. With the laser power used for this measurement, the optical depth of 2.5 is the upper limit of the current system. By increasing the laser output power larger optical depths can be measured. Because the cross talk between channels is small and it can be accurately corrected, and also because the 160 μrad field of view of the HSRL effectively suppresses multiple

scattering, the optical depths inside a cloud can be measured.

The accuracy of the optical depth measurements can be seen from the Figure 33. The leftmost graph shows the error in the optical depth measurement of a thin cirrus cloud and rightmost graph shows the error when a cirrus cloud of optical depth ~ 1 is studied. The errors presented here are root mean square errors and they consist of photon counting, background correction, calibration, and wavelength tuning errors. The signals are spatially averaged with a 150 m filter and the filtering is taken into account in the error analysis. The accuracy of the optical depth measurements is limited by the photon counting statistics. This can be seen from the error bars, which are on the same order as the signal fluctuations. The accuracy of the HSRL measurements can be increased by increasing the signal strength and/or by using a constrained nonlinear fit to the inverted molecular profile.

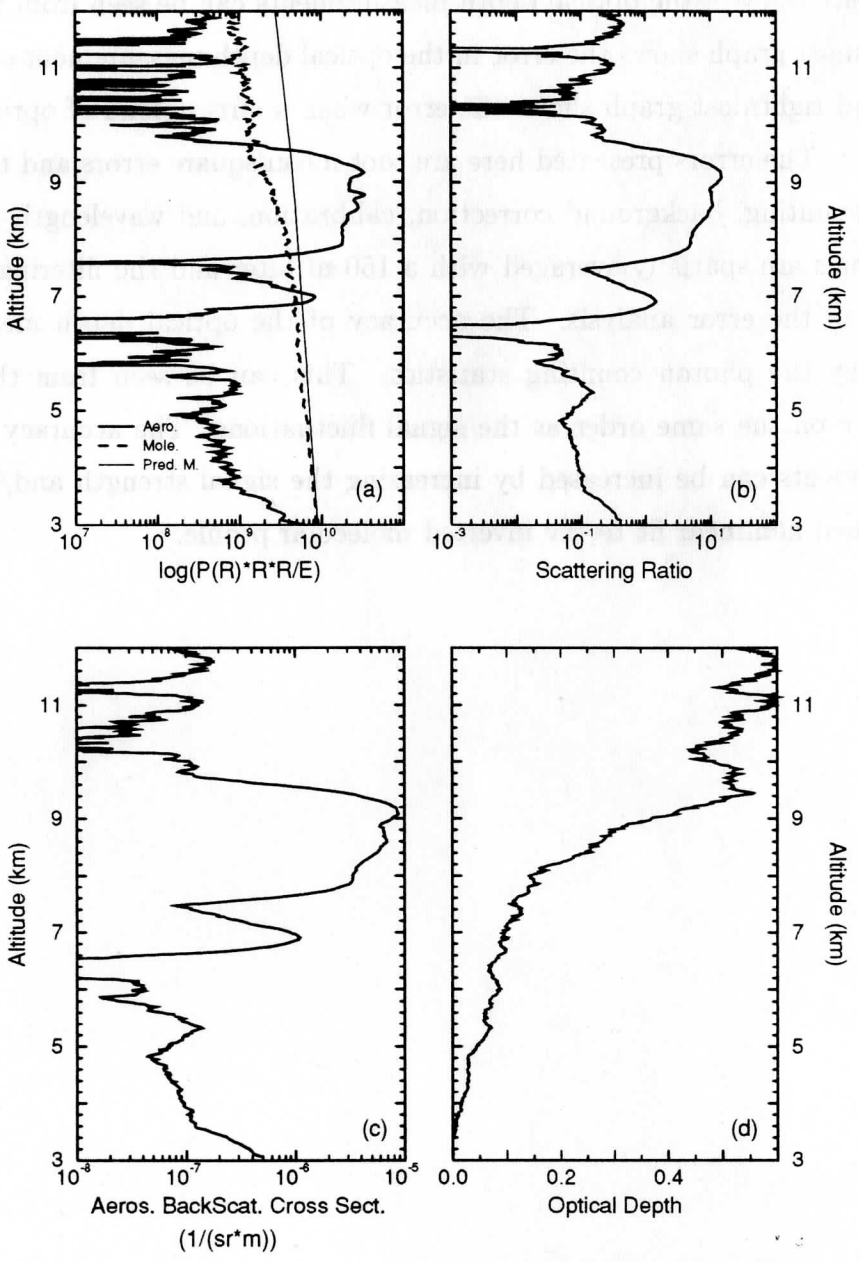

Figure 31. The measured scattering ratio, aerosol backscatter cross section and optical depth profiles of a thin cirrus cloud between 6.5 and 10 km (November 11, 1993 01:05-01:09 UT). (a) The inverted aerosol and molecular profiles along with a calculated molecular profile. The difference between the calculated and measured profiles shows the extinction. (b) The scattering ratio values are ranging from ~0.1 (clear air between 3 and 6.5 km) to 10 (cirrus cloud at 10 km). (c) The aerosol backscatter cross section of the cirrus cloud is $\sim 5{\cdot}10^{-6} m^{-1} sr^{-1}$ and $\sim$ for $10^{-7} m^{-1} sr^{-1}$ the clear air between altitudes 3 and 6.5 km. (d) The optical depth between 3 and 11 km is 0.55. The optical depth of the cirrus cloud is 0.4.

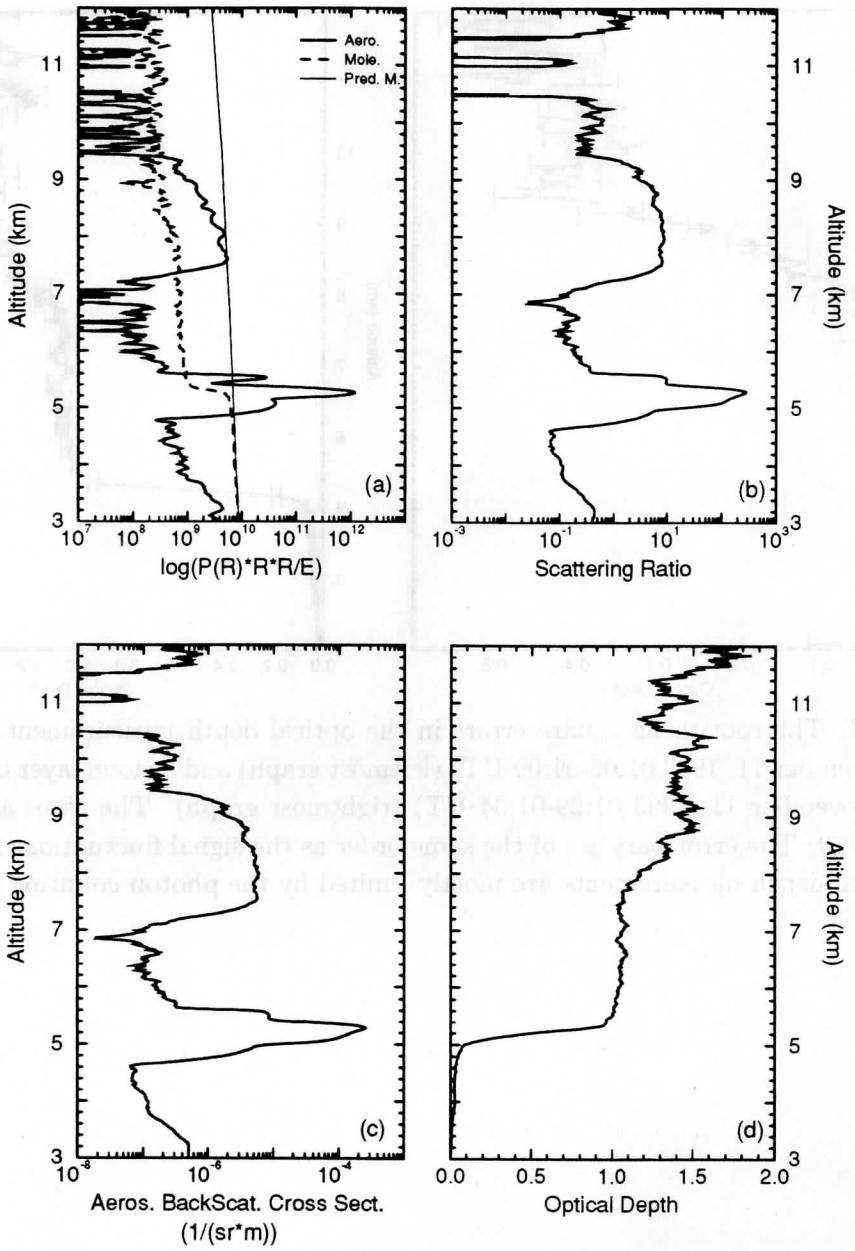

Figure 32. Scattering ratio, aerosol backscatter cross section and optical depth profiles of a thin cirrus cloud between 7 and 9.2 km and a water cloud with an ice crystal precipitation at 5.2 km (November 11, 1993 01:29-01:34 UT). (a) The inverted aerosol and molecular profiles along with the calculated molecular profile of the clear air. (b) Scattering ratio of the water cloud is $\sim$ 300 and 10 for the cirrus cloud. (c) The observed aerosol backscatter cross sections are ranging from $10^{-7} m^{-1} sr^{-1}$ for the clear air to $2{\cdot}10^{-4} m^{-1} sr^{-1}$ for the water cloud. (d) The optical depth is 1 for the water cloud and 0.4 for the cirrus.

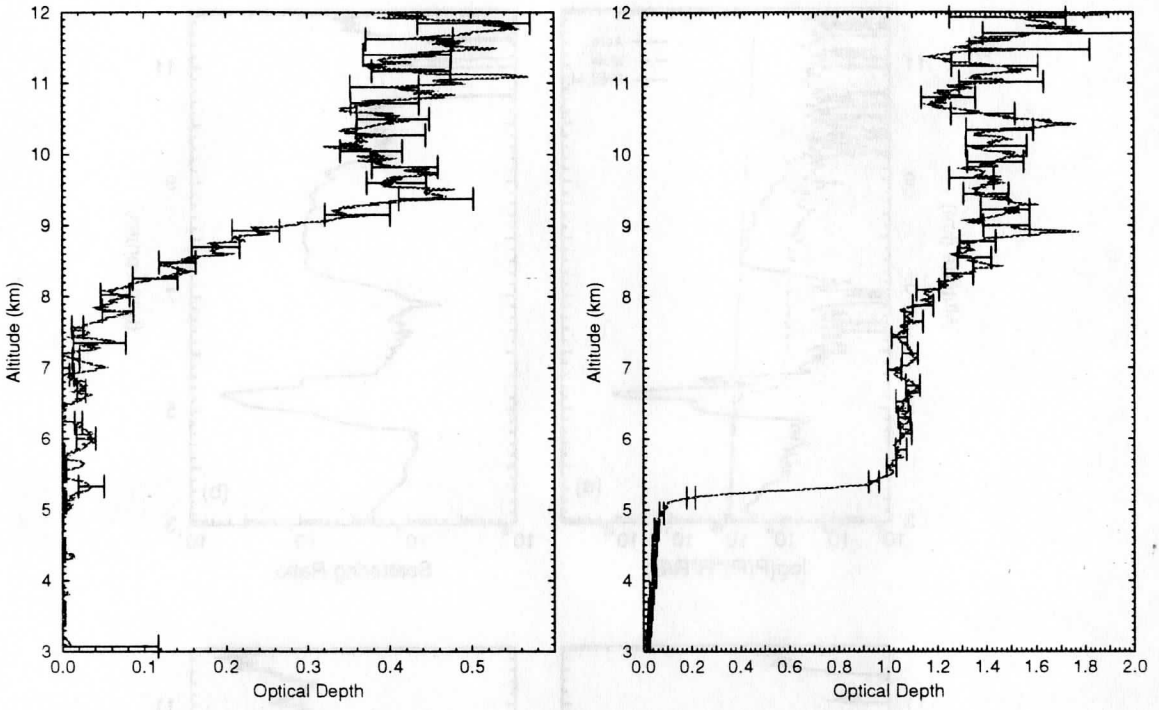

Figure 33. The root mean square errors in the optical depth measurement. A thin cirrus case (November 11, 1993 01:05-01:09 UT) (leftmost graph) and a cloud layer of optical depth of 1.4 (November 11, 1993 01:29-01:34 UT) (rightmost graph). The cases are the same as in Figure 29. The error bars are of the same order as the signal fluctuations indicating that the optical depth measurements are mostly limited by the photon counting statistics.

6.3 Measurements of atmospheric temperature

The temperature dependence of the Doppler-broadened molecular spectrum enables the measurements of the atmospheric temperature by a HSRL. The capability to measure the temperature would eliminate the possible errors due to the difference between the radiosonde reading and the current temperature over the lidar site. For this purpose, the temperature measurement capabilities of the University of Wisconsin HSRL were studied. The presence of clouds and strong layers of clear air aerosols will affect the shape of the molecular spectrum measured with the HSRL. The temperature measurement method presented in the following was used to test the capabilty of the HSRL to accurately measure the molecular spectrum width for layers with small aerosol content.

Lidars have been used for the measurements of the atmospheric temperature profile by many lidar groups. The technique proposed by Strauch *et al.*[44] and Cooney[45] allows calibrated temperature measurements by using the rotational Raman spectrum of nitrogen. With this technique about 1 °C temperature accuracy at low altitudes is achieved. Kalshoven *et al.*[46] demonstrated a differential absorption lidar method for temperature measurements. They used 2 laser wavelengths and O_2-absorption lines to measure atmospheric temperature up to 1 km altitude with 1 °C accuracy. Later Endemann and Byer[47] reported simultaneous measurements of atmospheric temperature and humidity with a continuously tunable IR-lidar. They used a three-wavelength differential absorption lidar technique and water vapor absorption lines. With this technique a 2.3 °C absolute accuracy was achieved. In addition to Raman and differential absorption lidar techniques, Keckhut *et al.*[48] used Rayleigh scattering lidar to measure atmospheric temperature for altitudes 30–70 km.

The temperature measurements made with a high resolution lidar have been reported by Alvarez *et al.*[16]. Their temperature measurement is based on the two barium absorption filters with different bandpasses. Because the strength of the signal received through an absorption cell is proportional to the width of the Doppler-broadened spectrum, the information of the signal strength together with a theoretical calculation for the Doppler-broadened Rayleigh-Brillouin spectrum can be used for the determination of the atmospheric temperature. Their latest measurements have

shown that only a 10 °C accuracy is achieved for profiles up to 5 km.

The preliminary measurements of the atmospheric temperature made with the University of Wisconsin HSRL have been based on one iodine absorption filter. For temperature measurements the system transmission spectrum is measured by scanning the laser wavelength over the iodine absorption spectrum, similarly as in the system calibration scan. For one temperature profile, data from 5 calibration scans were averaged. This was done to increase the signal to noise ratio of the measurement. The measured profile was calculated by averaging the signal over a 300 m range with 1 km steps.

The signal from atmosphere and detected through the iodine absorption cell is a convolution of the Doppler-broadened molecular spectrum and the iodine absorption spectrum. The Brillouin modified approximation for the Doppler-broadened spectrum was used to calculate the molecular line shapes at temperatures ranging from -70 to +30 °C with 1°C resolution. The calculated line shapes were convoluted with the measured iodine absorption spectrum. In order to define the atmospheric temperature at certain altitude, a least square fit was used to fit the measured profile to the calculated profile. The temperature that produced the best fit defined the temperature of that altitude. Figure 34 shows an example of the received signal from 8 km altitude observed through the iodine absorption cell normalized by the signal observed with the channel without iodine absorption filter. The iodine absorption spectrum is shown as a reference. The modeled molecular profile is shown for the temperature that produced the best fit. The best fit was found at -47°C temperature.

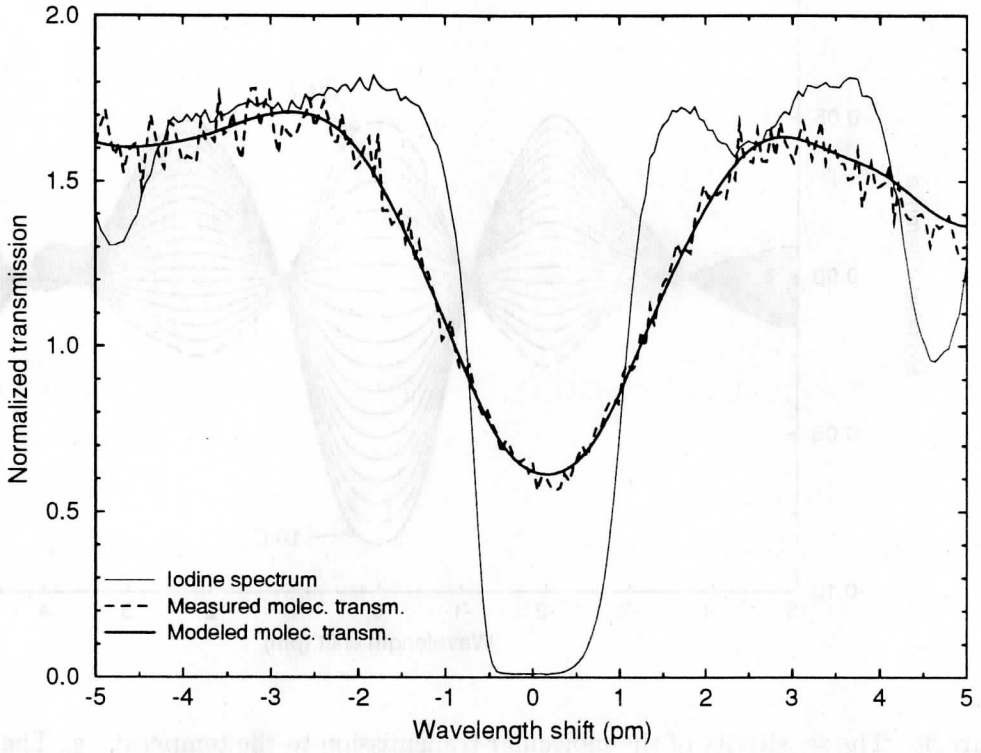

Figure 34. The HSRL signal from 8 km altitude observed through the iodine absorption filter normalized by the signal measured simultaneously without the iodine absorption filter. The iodine absorption spectrum is plotted for reference. The modeled molecular transmission is shown for the temperature that produced the best fit between measured and calculated molecular transmissions. The best fit was obtained at -47°C temperature.

The sensitivity of the molecular transmission of the iodine absorption filter to the width of the molecular spectrum is illustrated in Figure 35. The figure shows the effect of incorrect temperature to the fit. For this figure, the modeled molecular transmissions were subtracted from the modeled molecular transmission at -47 °C temperature. The temperature difference of 5 °C is displayed. The Figure 35 shows that a clear difference between temperatures is achieved, but because the differences are small, the accurate measurements of atmospheric temperature by the scanning technique are difficult to obtain.

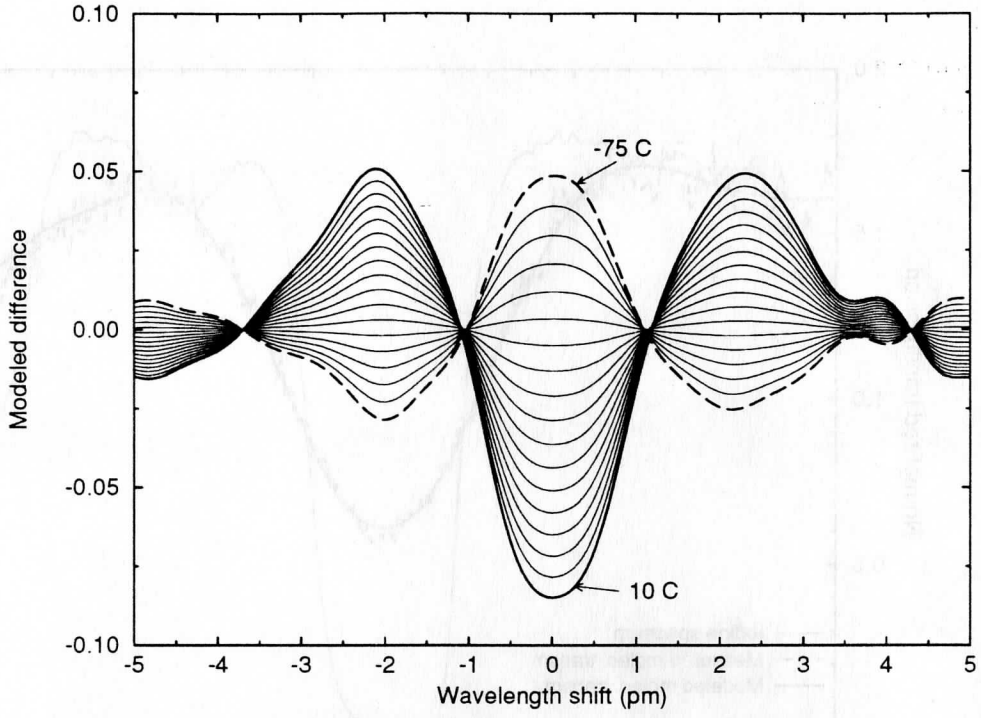

Figure 35. The sensitivity of the molecular transmission to the temperature. The difference in modeled molecular transmission to the molecular transmission at -47°C is shown with 5°C temperature steps.

A temperature profile measured on February 27, 1994, in Madison between 00:00 and 03:00 UT is presented in Figure 36. For the comparison the radiosonde temperature profiles from nearest weather stations are presented. The stations at Green Bay (WI, 180 km northeast from Madison), Peoria (IL, 350 km south from Madison), and St. Cloud (MN, 450 northwest from Madison) provided a radiosonde profile at 00:00 UT. The temperature values measured by the HSRL agree with the temperatures measured with the radiosondes. For the profile between 4 and 8 km the observed rms temperature differences are 2.97, 7.08, and 5.52 °C between HSRL and the weather stations. The rms difference between weather stations is 7.06 °C. For low altitudes, the largest difference between profiles is observed. This is expected because of the synoptic scale variations in weather conditions between different locations.

For altitudes between 6-8 km, a good agreement between HSRL measurement and the central Minnesota (St. Cloud) radiosonde profile is seen. These altitudes had a low aerosol content providing scattering ratio of ~ 0.02. The temperatures above 8 km show a big deviation from the radiosonde temparatures. This is due a strong aerosol layer, that disturbs the HSRL temperature measurement. The scattering ratio of the aerosol layer above 8 km was ~ 0.3. Also the measured temperature values for altitude between 2 and 3.5 km are colder than the radiosonde values. This is due to presence of a low level aerosol layer with scattering ratio of $\sim$0.1 The presence of aerosols deepens the measured spectrum and therefore a fit into this spectrum underestimates the temperature. Therefore, if the temperatures are going to be measured in the presence of aerosols, the effect of the aerosol signal has to be separated from the molecular contribution.

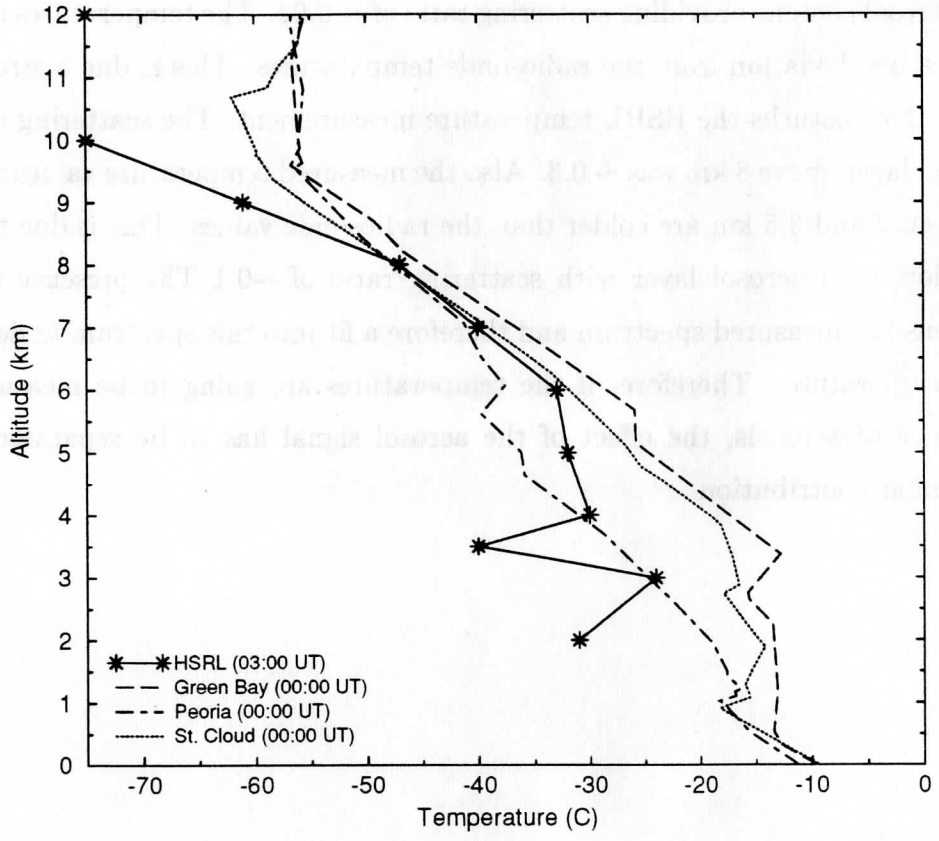

Figure 36. A temperature profile obtained with the HSRL on February 27, 1994. The temperature profile obtained with radiosondes show the atmospheric temperature measured at the closest weather stations. A good agreement between HSRL and radiosonde observations is observed between altitudes of 4 and 8 km. These are altitudes with a low aerosol backscatter content.

7 Error analysis

7.1 Error sources

The signal detected with a photon counting system is a combination of backscatter signal, background light, and internal noise in the photodetector. The lidar equation (Eq. (1)) shows that the amount of received signal is determined by the number of transmitted photons, scattering cross section, backscatter phase function, area of the telescope, transmission of the receiver optics, and the sensitivity of the detectors. On the other hand, the HSRL measurements are dependent on the system calibration coefficients (Eqs. (17) and (18)). The errors in the HSRL measurements can be divided into 5 main categories:

1. errors due to photon counting statistics
2. errors due to changes in system calibration coefficients
3. errors in the background subtraction
4. errors due to a multiple scattering contribution
5. errors in the atmospheric temperature profile used to compute the molecular density

The error in the photon counting process is proportional to the square root of the measured signal. The errors due to photon counting statistics that are induced to the calibration coefficients were discussed in Chapter 5.

The system detection efficiency is a combination of the system transmission and the photomultiplier quantum efficiency. The system detection efficiency affects the amount of detected signal and therefore, it is directly related to the photon counting statistics. A model to calculate the expected system transmission was developed. This model includes the spectral transmission of interference filters, etalons, and iodine absorption cell, transmissions and reflections of optical components (lenses, mirrors, cubes, etalon chamber windows) and photomultiplier quantum efficiencies.

The transmittance and reflectance values of different optical components were confirmed with measurements. The calculated transmission efficiencies were compared with the measured values. For this study, a clear air case was chosen. Because the properties of molecular scattering are well known, the lidar equation for molecular scattering (Eq. 3) can be solved for the number of photons expected for the pure molecular return.

In order to predict the expected molecular return, the calculated system transmission was convoluted with the calculated molecular spectrum at a 5 km reference altitude. The temperature for the Doppler-broadened molecular spectrum calculation was taken from a radiosonde profile. By calculating the ratio of measured to expected number of photons given by the lidar equation, the actual system transmission was estimated. The two way extinction between lidar and the backscatter volume was assumed to $\sim$ 1. The comparison between expected and measured detection efficiency values is given in Table 2. This comparison was made without using the low resolution etalons. Each etalon decreases the transmission by a factor of $\sim$ 2.

Table 2. HSRL detection efficiency

Channel	Calculated (%)	Measured (%)
Aerosol+Molecular	0.78	0.6
Molecular	0.44	0.36
WFOV	4.4	3.4

The transmission efficiency values show $\sim$ 25 % difference between calculated and measured values. A $\sim$ 10% error can be made by assuming the extinction between lidar to 1. Also the uncertainty on the transmission and reflectance values of optical components affect the calculation. The largest uncertainty is the quantum efficiency of the photomultipliers. The value 0.12 is taken from the manufacturers specification, but only a 0.03 change in the quantum efficiency would correct the difference. The transmissions and reflectances of the receiver components that affect to the detection efficiency are listed in Table 3. The transmission and reflection numbers of some components are confirmed with a measurement and rest of the values are obtained from the manufacturers specifications.

Table 3. Transmission / Reflection losses in HSRL components. The source for the transmission and reflection values is manufacturers specification (spec.) or a measurement (meas.).

Channel	Component	R or T (%)	Source	Total(%)
ALL				
	Telescope mirrors (2)	R = 90.0	meas.	R= 81.0
	Interference filter (1)	T= 50.0	meas.	T=50.0
	Polarizing cubes (2/channel)	T=99.0	spec.	T=99.0
		R=93.0	spec.	R=93.0
	PMT quantum efficiency	QE= 12.0	spec.	QE= 12.0
A+M, M				
	Etalon chamber windows (3)	T= 90.0	meas.	T= 73.0
	Mirrors (2 /channel)	T= 90.0	meas.	T= 81.0
	Lenses (3 / channel)	T=99.4	spec.	T=98.2
A+M				
	Beam splitter	T=30.0	meas.	T=30.0
M				
	Beam splitter	R=70.0	meas.	R=70.0
	Iodine absorption cell	T(cell)=80.0	meas.	T=80.0
		T(mol.)$\sim$30.0	calc.	T=30.0
WFOV				
	Lens	T=99.4	spec.	T = 99.4
Total eff.				
	Aerosol+Molecular Channel			0.78
	Molecular Channel			0.44
	WFOV Channel			4.4

The reflectivity of the telescope mirrors is limited by the reflectivity of the aluminum coating. The poor transmission values of the etalon chamber windows and the mirrors have a big effect on the detection efficiency, because they lose $\sim$ 41% of the received signal. These components are taken from the old system and they are not optimized for the current operating wavelength. In order to increase the system performance, these components are going to be replaced in near future.

The errors due to change in the system calibration coefficients are mainly caused by change in the transmission-receiver wavelength tuning and change in the system alignment. These errors can be calculated by a partial differentiation.

A change in atmospheric temperature and pressure affects the amount of detected molecular signal. Therefore, if the radiosonde profile is not valid for the measure-

ment conditions, an error is generated in the calculated molecular signal. The width of the Doppler-broadened spectrum directly affects the calibration coefficient C_{mm}. This affects to the amount of molecular signal subtracted from the signal detected with the combined aerosol+molecular channel. In Brillouin spectrum and molecular backscatter cross section calculations, the effects of changing atmospheric conditions are minimized by using the current radiosonde data from the nearest weather stations. By comparing temperature and pressure readings from the closest radiosonde stations, an $\sim$ 1-5 % difference between stations is observed. This due to the geographic separation between weather stations. Because the lidar is located between these stations, the error is expected to be smaller.

In addition to the atmospheric temperature and pressure changes, the effects of the wind on the measurement has to be considered because the high wind velocities can shift the Doppler-broadened spectrum with respect to the laser wavelength. A bulk shift in respect to the radiated spectrum is an indicator of wind, while the line broadening is associated with the random thermal motions of the molecules (and aerosols). If the line center of the Doppler-broadened spectrum is shifted in respect to the transmitted wavelength, the system calibration will be in error. The Doppler-shift for the backscatter signal can be calculated from

$$\frac{\Delta\nu}{2\nu_o} = \frac{v}{c}, \tag{24}$$

where

$\Delta\nu$ = wavenumber shift

$2\nu_o$ = wavenumber of the laser line center

v = molecular velocity

c = velocity of light

The wind velocities measured by a radiosonde can be used as an estimate for the horizontal wind. The maximum horizontal wind velocities are generally smaller than 70 m/s at cirrus cloud altitudes, and the maximum vertical winds are normally below 1 m/s in troposphere. Therefore, the maximum wind to the lidar pointing direction θ (θ = 4 degrees from the zenith) is $v_l = v_x sin\theta + v_y cos\theta$, which corresponds to a

velocity of 5.9 m/s. The shift in the spectrum is 19.8 fm, which is much smaller than the current 0.052 pm detection accuracy of the molecular spectrum. Also the horizontal wind speeds are generally much lower[49], and therefore, the effects due to wind to the HSRL measurements are negligible, but caution is required if larger zenith angles of the pointing direction are considered.

The uncertainty in transmitter-receiver peak transmission tuning can be seen as a shift in the transmitter wavelength in respect to the spectral transmission maximum of the receiver. This effects the amount of detected molecular signal, but if the drift is large, a change in the amount of detected aerosol is observed. The drift also affects the system transmission. In the current HSRL, the effects of a drift between transmitter and receiver wavelengths are minimized by locking the transmitter laser wavelength to the iodine absorption peak (see Chapter 5.2). The effects of the wavelength locking to the measured signal were also discussed in Chapter 5.2.

In addition to the previous errors, the system calibration is affected by all misalignments of the system. The error due to a system misalignment can be divided into three different categories:

1. alignment error in the receiver optics

2. alignment error between transmitter and receiver pointing direction

3. an error in the compensation for the beamsplitter polarization dependence

A small alignment error (off focus, off axis or misalignment in system pointing direction) can lead situations, where part of the backscattered light is lost in the optics, detector, or atmosphere. This can easily lead into a range dependence of the received signal. This affects the inversion and furthermore, the measured optical depth. A misalignment also affects the total system transmittance and the signal to noise ratio of the measured signal. System pointing instabilities make the overlap correction of the received signal difficult. The overlap region is the close distance range where the overlap of the receiver field of view and the transmitted beam is incomplete. The effect of misalignment between transmitter end receiver pointing directions is largest for the overlap region. The effects vary daily depending from

the accuracy of the alignment between transmitter and receiver pointing direction. Large receiver field of views are less critical for the alignment errors. The signal measured with the large field of views of the WFOV channel can be used to align the small field of view channels. In the HSRL, the alignment between transmitter and receiver pointing directions is performed as follows. A corner cube is used to direct the outgoing laser beam to the receiver. The beam is aligned to the center of the receiver aperture by adjusting the turning mirror on the top of the telescope secondary mirror. Then the corner cube is removed and the signal from the atmosphere is used to verify the alignment. The signal of the large field of view of the WFOV-channel is compared to signal of the combined channel. If the channels are properly aligned and if the transmitter and receiver pointing directions are the same, the slopes of the signals are similar for the altitudes above the overlap region and therefore, the ratio between WFOV-channel signal to the spectrometer channel signal is constant. The alignment of the smallest WFOV channel aperture can be verified similarly by comparing the signal from the larger aperture to the signal from the smallest WFOV aperture. The effects of alignment errors on the system measurement accuracy are not included to the error analysis, because with a careful alignment the errors can be minimized.

The accuracy of the background correction is mostly affected by the photon counting statistics. The effects of photon counting on the measured background are decreased by summing at least 66 range bins together. The background correction method used in HSRL measurements was described earlier in Chapter 3.2.2. In addition to the photon counting statistics, the accuracy of the background correction is affected by the slight tendency to overestimate the number of background counts for altitudes close to 33 km. Eventhough atmospheric density, and therefore the amount of Rayleigh scattering, decreases rapidly with the range, some of the signal that is measured into the upper range bins of the HSRL can still be due to Rayleigh scattering. Therefore, when those range bins are used to calculate the number of background counts, the background is slightly overestimated due to the Rayleigh signal.

The effects of the multiple scattering on the received lidar signal are usually neglected and the received signal is assumed to be single scattered. A lidar return from

water and thick cirrus clouds usually encounters large optical depths within a short distance of the cloud boundary and therefore, many of the received photons are likely to be from multiple scattering. The effect of multiple scattering to the lidar signal is dependent from the receiver field of view, cloud particle size, range from the lidar, and the optical depth of the cloud. The effect of multiple scattering can be seen in the lidar profile as a reduction in the rate of attenuation of the signal. In depolarization, the effect of multiple scattering will show up as an increase in the depolarization ratio towards the cloud top. The HSRL measurements have shown, that the effect of multiple scattering on the smallest field of view signals is small, because the depolarization ratio values observed for the water clouds are low.

The current HSRL profiles are not corrected for multiple scattering contributions. An inversion program that accounts multiple scattering effects is currently in progress. The magnitude of the error caused by assuming the signal to be originated from single scattering depends from the field of view of the receiver, optical thickness of the cloud, size of the cloud particles, and penetration depth. The clear air aerosols and thin cirrus layers have a small or no multiple scattering effect. Because of the large particle size of ice crystals, the signal from thick cirrus clouds contains a multiple scattering contribution even for the small field of views. The multiple scattering from water cloud droplets is distributed to the larger field of views. The amount of multiple scattering on the measured signal can be estimated from the paper by Eloranta and Shipley[27].

7.2 Effects of different errors on the measured optical parameters

The effects of different errors on the inverted aerosol and molecular return and to the measured optical parameters were calculated by partially differentiating Equations (19), (20), and (4)–(13). The error analysis is made for the data obtained on November 11, 1993. A section of the data for a thin two-layer cirrus cloud structure is analyzed. The case is the same as shown in Figure 31. The thin cirrus cloud case is chosen for this study for two reasons. First, the backscatter signal from thin high altitude cirrus is small. Therefore, an error analysis made for the thin cirrus tests the measurement sensitivity of the system. Second, if accurate measurements of thin cirrus clouds can be made within short averaging time, then the HSRL can be considered for studies of contrail formed cirrus. The short averaging time is important for the contrail studies, because they drift rapidly with the wind and only a limited number of samples from one contrail can be obtained.

Information from cloud optical properties can be obtained by comparing the HSRL measurements with satellite observations. Thus, the averaging time of the HSRL data has to be close to the time resolution of a satellite image. The use of the short averaging times also prevents the smoothing of the the lidar signal so that the rapid changes in cloud structure in both time and altitude remain in the data. For this study, the 3 min averaging time was chosen to study the errors in the inverted aerosol and molecular returns, inverted aerosol and molecular depolarization ratios, backscatter ratio, optical depth, and aerosol backscatter cross section. Because the measurement of the backscatter phase function is difficult due to uncertainty in the extinction cross section determination, the 6 min averaging time was used for error analysis of the phase function measurement.

The error analysis presented here shows the total errors together with the partial errors. All errors are calculated as mean square errors (see Equations 26-35) and presented as fractional root mean square errors (see Figures 37- 44). The partial errors in Figures 37- 44 present the effects of errors on the photon counting of the combined channel and the molecular channel, error in the molecular backscatter cross section per unit volume due to the uncertainty in temperature and pressure profiles,

and errors in the calibration coefficient determination. The error estimate calculations include the photon counting error, error in the background correction, error due to the uncertainty in the temperature and pressure profiles measured with a radiosonde, and errors due to the tuning of the laser wavelength. The errors due to system alignment and the error due to multiple scattering effects are not included to this error analysis. Also the error in the determination of the range R is negligible.

The errors in background correction are assumed to be from photon counting statistics. The uncertainty of 2 % for the temperature profiles is used. The error in pressure profile is estimated to 1 mbar of the radiosonde pressure reading at each altitude. The error is due to the geographic separation between closest weather stations. This is estimated from the radiosonde measurements from the closest weather stations. The uncertainty on the molecular spectrum calculation is estimated with the 2% uncertainty on the atmospheric temperature. The error on the calibration coefficient C_{mm} determination is a combination of the photon counting error, uncertainty of the molecular spectrum, and the error caused by tuning of the laser wavelength. The accuracy of the calibration coefficient C_{am} determination is limited by the photon counting statistics. The error in the molecular backscatter cross section per unit volume measurement depends on the errors in the atmospheric temperature and pressure.

The error in the molecular profile can be given as

$$
\begin{aligned}
(\Delta N_m(R))^2 = \; & \left(\frac{\partial N_m(R)}{\partial S_m(R)}\right)^2 (\Delta S_m(R))^2 + \left(\frac{\partial N_m(R)}{\partial S_{a+m}(R)}\right)^2 (\Delta S_{a+m}(R))^2 + \\
& \left(\frac{\partial N_m(R)}{\partial C_{mm}(R)}\right)^2 (\Delta C_{mm}(R))^2 + \left(\frac{\partial N_m(R)}{\partial C_{am}}\right)^2 (\Delta C_{am})^2 + \\
& \left(\frac{\partial N_m(R)}{\partial B_{a+m}}\right)^2 (\Delta B_{a+m})^2 + \left(\frac{\partial N_m(R)}{\partial B_m}\right)^2 (\Delta B_m)^2, \qquad (25)
\end{aligned}
$$

which leads to equation

$$\left(\frac{\Delta N_m(R)}{N_m(R)}\right)^2 = \frac{C_{am}(R)^2 \Delta S_{a+m}(R)^2}{\left(S_m(R) - B_m(R) - C_{am}(R)\left(S_{a+m}(R) - B_{a+m}(R)\right)\right)^2} + \frac{\Delta S_m(R)^2}{\left(S_m(R) - B_m(R) - C_{am}(R)\left(S_{a+m}(R) - B_{a+m}(R)\right)\right)^2} + \frac{\Delta C_{am}(R)^2}{\left(C_{mm}(R) - C_{am}(R)\right)^2} + \frac{\Delta C_{mm}(R)^2}{\left(C_{mm}(R) - C_{am}(R)\right)^2} + \frac{C_{am}(R)^2 \Delta B_{a+m}(R)^2}{\left(S_m(R) - B_m(R) - C_{am}(R)\left(S_{a+m}(R) - B_{a+m}(R)\right)\right)^2} + \frac{\Delta B_m(R)^2}{\left(S_m(R) - B_m(R) - C_{am}(R)\left(S_{a+m}(R) - B_{a+m}(R)\right)\right)^2} \quad (26)$$

$\Delta S_m(R)$ and $\Delta S_{a+m}(R)$ are the photon counting errors. $\Delta C_{am}(R)$ and $\Delta C_{mm}(R)$ the errors in the calibration coefficient determination. The background correction errors are given by $\Delta B_m(R)$ and $\Delta B_{a+m}(R)$. The error analysis made for the calibration coefficients show that C_{mm} can be determined with better than 5 % accuracy and C_{am} with a better than 2 % accuracy.

The effects of different errors on the inverted molecular return are shown in Figure 37. The errors in inverted molecular return are dominated by the photon counting statistics and the determination of the calibration coefficient C_{mm}. The error due to the measurement accuracy of the aerosol signal is negligible. The errors in the C_{am} determination have only a small effect on the inverted molecular return.

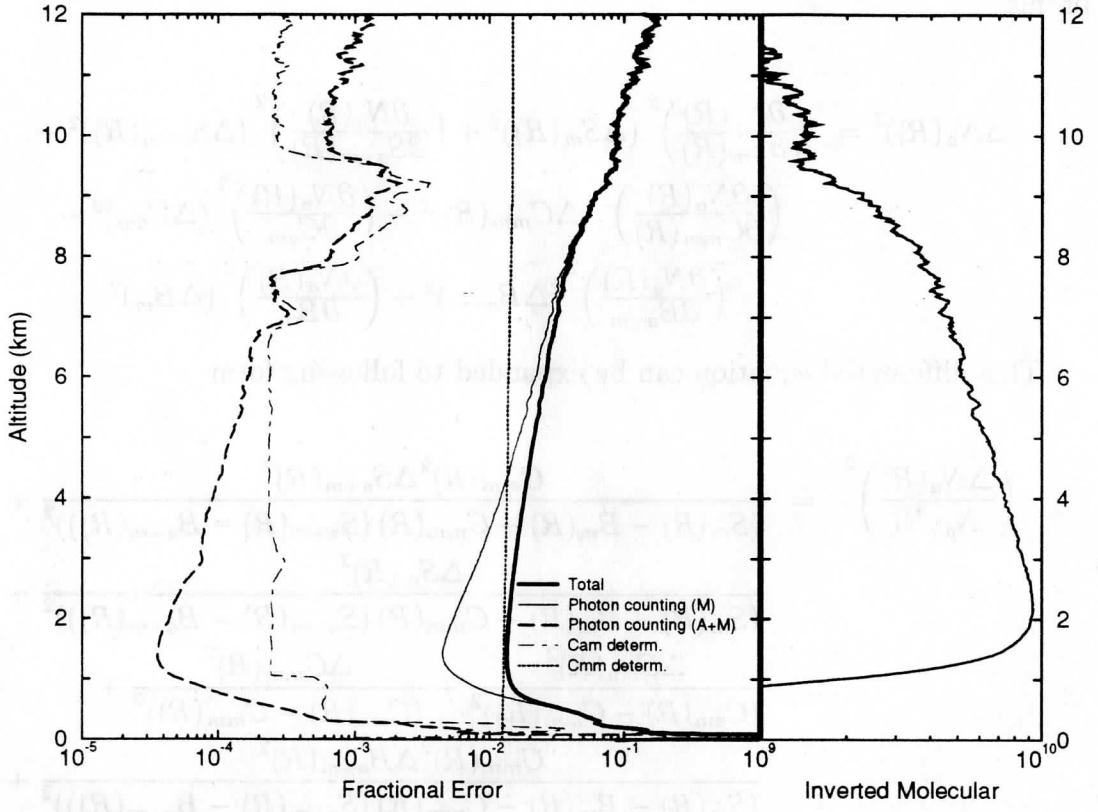

Figure 37. The effects of different errors on the inverted molecular profile (November 11, 1993, 01:05-01:08 UT). Data from a thin cirrus cloud is analyzed by using a 3 min. averaging time. The measured molecular profile (rightmost graph) presents the signal variations as a function of altitude. The extinction due to the thin cirrus cloud is observed between 6.5 and 10 km. The accuracy of the inverted molecular return determination is mostly limited by the photon counting statistics and the determination accuracy of the calibration coefficient C_{mm} (leftmost graph). The large errors shown in the overlap region below 2 km are due to a focus error and incomplete overlap of the receiver field of view and transmitted laser beam.

The error in the measured aerosol profile can derived similarly to the molecular profile

$$
\begin{aligned}
(\Delta N_a(R))^2 = & \left(\frac{\partial N_a(R)}{\partial S_m(R)}\right)^2 (\Delta S_m(R))^2 + \left(\frac{\partial N_a(R)}{\partial S_{a+m}(R)}\right)^2 (\Delta S_{a+m}(R))^2 + \\
& \left(\frac{\partial N_a(R)}{\partial C_{mm}(R)}\right)^2 (\Delta C_{mm}(R))^2 + \left(\frac{\partial N_a(R)}{\partial C_{am}}\right)^2 (\Delta C_{am})^2 + \\
& \left(\frac{\partial N_a(R)}{\partial B_{a+m}}\right)^2 (\Delta B_{a+m})^2 + \left(\frac{\partial N_a(R)}{\partial B_m}\right)^2 (\Delta B_m)^2
\end{aligned} \tag{27}
$$

This differential equation can be expanded to following form

$$
\begin{aligned}
\left(\frac{\Delta N_a(R)}{N_a(R)}\right)^2 = & \frac{C_{mm}(R)^2 \Delta S_{a+m}(R)^2}{\left(S_m(R) - B_m(R) - C_{mm}(R)\left(S_{a+m}(R) - B_{a+m}(R)\right)\right)^2} + \\
& \frac{\Delta S_m(R)^2}{\left(S_m(R) - B_m(R) - C_{mm}(R)\left(S_{a+m}(R) - B_{a+m}(R)\right)\right)^2} + \\
& \frac{\Delta C_{am}(R)^2}{\left(C_{am}(R) - C_{mm}(R)\right)^2} + \frac{\Delta C_{mm}(R)^2}{\left(C_{am}(R) - C_{mm}(R)\right)^2} + \\
& \frac{C_{mm}(R)^2 \Delta B_{a+m}(R)^2}{\left(S_m(R) - B_m(R) - C_{mm}(R)\left(S_{a+m}(R) - B_{a+m}(R)\right)\right)^2} + \\
& \frac{\Delta B_m(R)^2}{\left(S_m(R) - B_m(R) - C_{mm}(R)\left(S_{a+m}(R) - B_{a+m}(R)\right)\right)^2}
\end{aligned} \tag{28}
$$

The accuracy of the inverted aerosol return is mostly affected by the determination accuracy of the inverted molecular return (photon counting statistics and C_{mm} determination accuracy) and the photon counting statistics of the combined aerosol and molecular channel (see Figure 38). For the cases of small aerosol backscatter content, large errors in the determination of the aerosol return are made when short averaging times are used. The errors are caused by subtracting a large amount of molecular signal from the combined channel signal that contains the strong molecular signal together with a small aerosol contribution. Therefore, the statistics of the molecular signal dominates the aerosol backscatter signal determination. The determination of clear air aerosols requires longer averaging times in order to achieve reliable results. On the other hand, the measurements of cloud aerosols can be done with $\sim$ 1.0% accuracy (7-10 km).

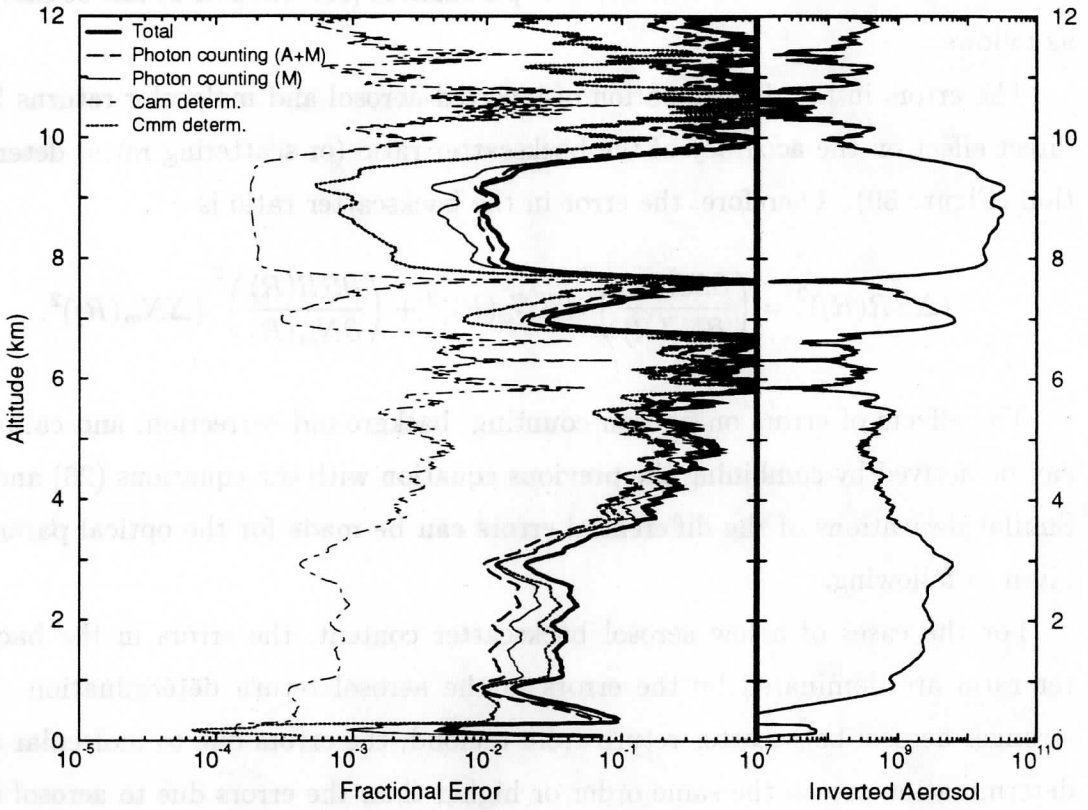

Figure 38. The effects of different errors on the inverted aerosol profile in case of a thin cirrus cloud (November 11, 1993, 01:05-01:08 UT). Averaging time of the data is 3 min. The measured aerosol profile (rightmost graph) shows the signal variation as function of altitude. The thin cirrus layer is observed between 6.5 and 10 km and a strong aerosol layer is seen between 0 and 3.5 km. The measurements of the aerosols are limited by the accuracy of the molecular profile measurements (leftmost graph). The 3 min averaging time provides 1-5% accuracy for thin cirrus cloud and strong aerosol layer measurements, but a longer averaging time is required for the measurements of the clear air aerosols.

Using the calculated errors for the measured aerosol and molecular profiles, the errors in the determination of the optical parameters (see Chapter 2) can be calculated as follows.

The errors in the determination of inverted aerosol and molecular returns have a direct effect on the accuracy of the backscatter ratio (or scattering ratio) determination (Figure 39). Therefore, the error in the backscatter ratio is

$$(\Delta SR(R))^2 = \left(\frac{\partial SR(R)}{\partial N_a(R)}\right)^2 (\Delta N_a(R))^2 + \left(\frac{\partial SR(R)}{\partial N_m(R)}\right)^2 (\Delta N_m(R))^2, \qquad (29)$$

The effects of errors on photon counting, background correction, and calibration can be derived by combining the previous equation with the equations (26) and (28). Similar derivations of the differential errors can be made for the optical parameters given in following.

For the cases of a low aerosol backscatter content, the errors in the backscatter ratio are dominated by the errors in the aerosol return determination. For a stronger aerosol backscatter return from a cloud, the errors due to molecular return determination are on the same order or higher than the errors due to aerosol return determination. The backscatter ratios of the thin cirrus and strong aerosol layers can be determined with better than 10% accuracy, but measurements of the clear air require longer averaging times.

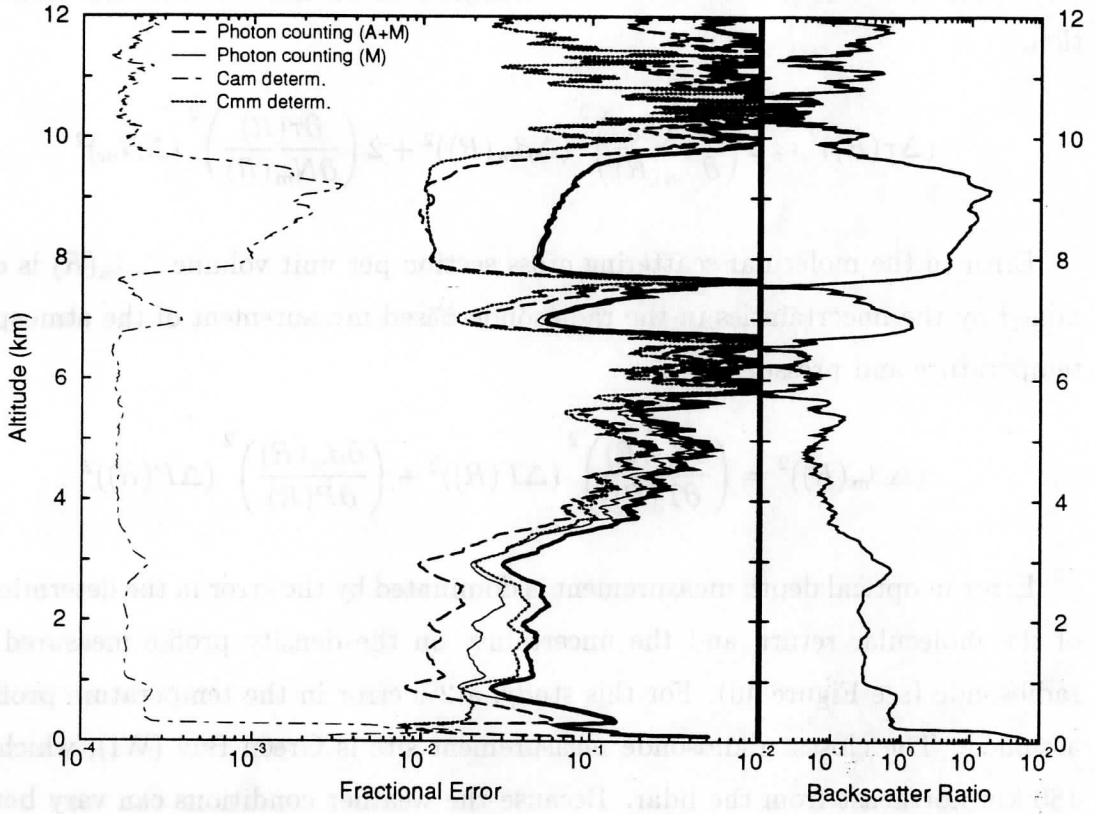

Figure 39. The effects of different errors on the backscatter ratio in case of a thin cirrus cloud (November 11, 1993, 01:05-01:08 UT). Averaging time of the data is 3 min. The backscatter ratio profile (rightmost graph) shows the ratio of the aerosol return to the molecular return as a function of altitude. Backscatter ratios ~0.1 to 20 are observed. The errors in the backscatter ratio measurement (leftmost graph) are determined by the accuracy of the aerosol and molecular return measurements. For the altitudes with a low aerosol content, the error in backscatter ratio is limited by the accuracy of the aerosol backscatter return measurement. For the cirrus cloud the accuracy depends on the goodness of the molecular backscatter profile measurement.

The error in optical depth can be approximated as sum of error in the molecular scattering cross section per unit volume and error in the molecular return determination.

$$(\Delta\tau(R))^2 \approx 2\left(\frac{\partial\tau(R)}{\partial\beta_m(R)}\right)^2(\Delta\beta_m(R))^2 + 2\left(\frac{\partial\tau(R)}{\partial N_m(R)}\right)^2(\Delta N_m)^2 \tag{30}$$

Error in the molecular scattering cross section per unit volume $\Delta\beta_m(R)$ is determined by the uncertainties in the radiosonde based measurement of the atmospheric temperature and pressure.

$$(\Delta\beta_m(R))^2 = \left(\frac{\partial\beta_m(R)}{\partial T(R)}\right)^2(\Delta T(R))^2 + \left(\frac{\partial\beta_m(R)}{\partial P(R)}\right)^2(\Delta P(R))^2 \tag{31}$$

Error in optical depth measurement is dominated by the error in the determination of the molecular return and the uncertainty on the density profile measured by a radiosonde (see Figure 40). For this study, a 2% error in the temperature profiles is assumed. The closest radiosonde measurement site is Green Bay (WI), which is $\sim$ 180 km northeast from the lidar. Because the weather conditions can vary between the lidar site and the closest weather station, larger errors in the temperature profile are possible. The effects of errors on the atmospheric density profile can be minimized by making radiosonde measurements on the lidar site.

The figure shows, that with 3 min averaging time the cloud optical depths can be detected with $\sim$ 10 % accuracy. This accuracy is sufficient when clouds with optical depths greater than 1 are measured. For situations where optical depth is less than 1, a longer averaging time is required.

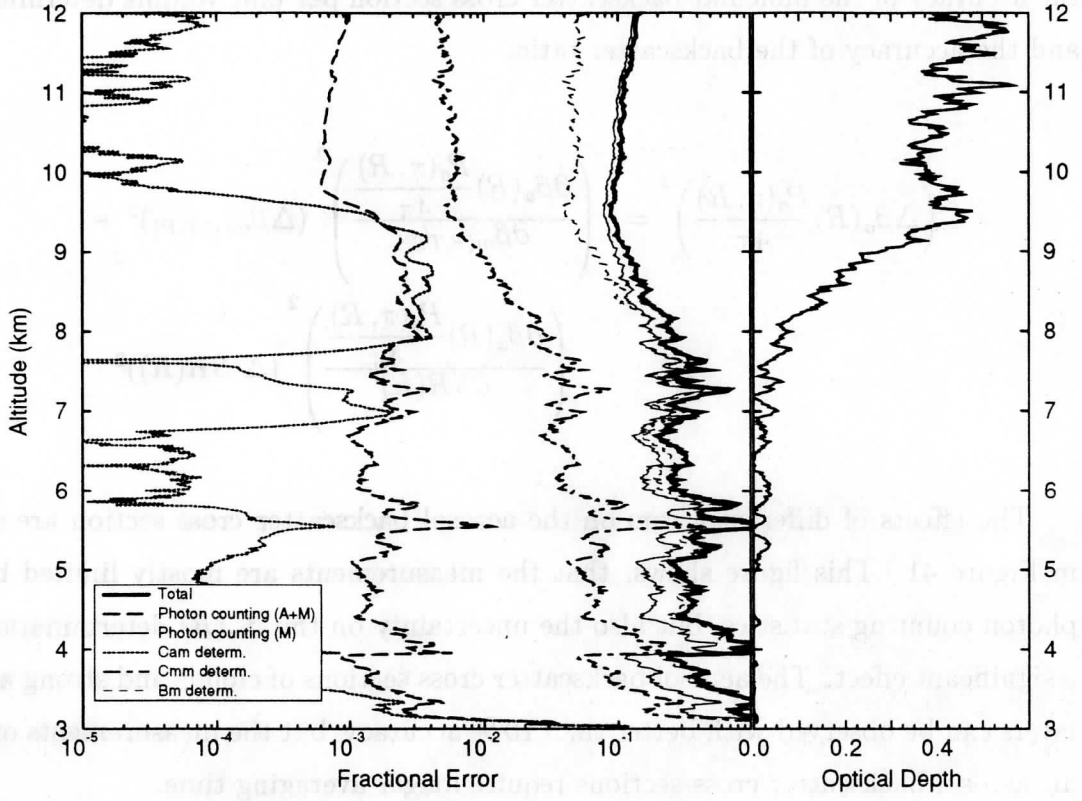

Figure 40. The effects of different errors to the optical depth in case of a thin cirrus cloud (November 11, 1993, 01:05-01:08 UT). Averaging time of the data is 3 min. The optical depth profile (rightmost graph) shows the variation of the optical depth as a function of altitude. Optical depth of 0.5 is measuered for the range from 3 to 12 km and optical depth of 0.4 is observed for the cirrus cloud between 6.5 and 10 km. The errors in the measurement of the optical depth below 6.5 km are dominated by the inaccuracy of the radiosonde profile (leftmost graph) and the photon counting statistics of the molecular channel. The error in the calibration coefficient C_{mm} determination also has a significant effect on the total error. The optical depth of the thin cirrus cloud can be measured with $\sim$ 10% accuracy.

The accuracy of the aerosol backscatter cross section measurement is limited by the accuracy of the molcular backscatter cross section per unit volume determination and the accuracy of the backscatter ratio.

$$\left(\Delta\beta_a(R)\frac{P_a(\pi,R)}{4\pi}\right)^2 = \left(\frac{\partial\beta_a(R)\frac{P_a(\pi,R)}{4\pi}}{\partial\beta_{m(R,T,P)}}\right)^2 (\Delta\beta_{m(R,T,P)})^2 + \left(\frac{\partial\beta_a(R)\frac{P_a(\pi,R)}{4\pi}}{\partial SR(R)}\right)^2 (\Delta\ SR(R))^2 \qquad (32)$$

The effects of different errors on the aerosol backscatter cross section are shown in Figure 41. This figure shows, that the measurements are mostly limited by the photon counting statistics, but also the uncertainty on the $\beta_m(R)$ determination has a significant effect. The aerosol backscatter cross sections of clouds and strong aerosol layers can be observed with better than 10 % accuracy, but the measurements of clear air aerosol backscatter cross sections require longer averaging time.

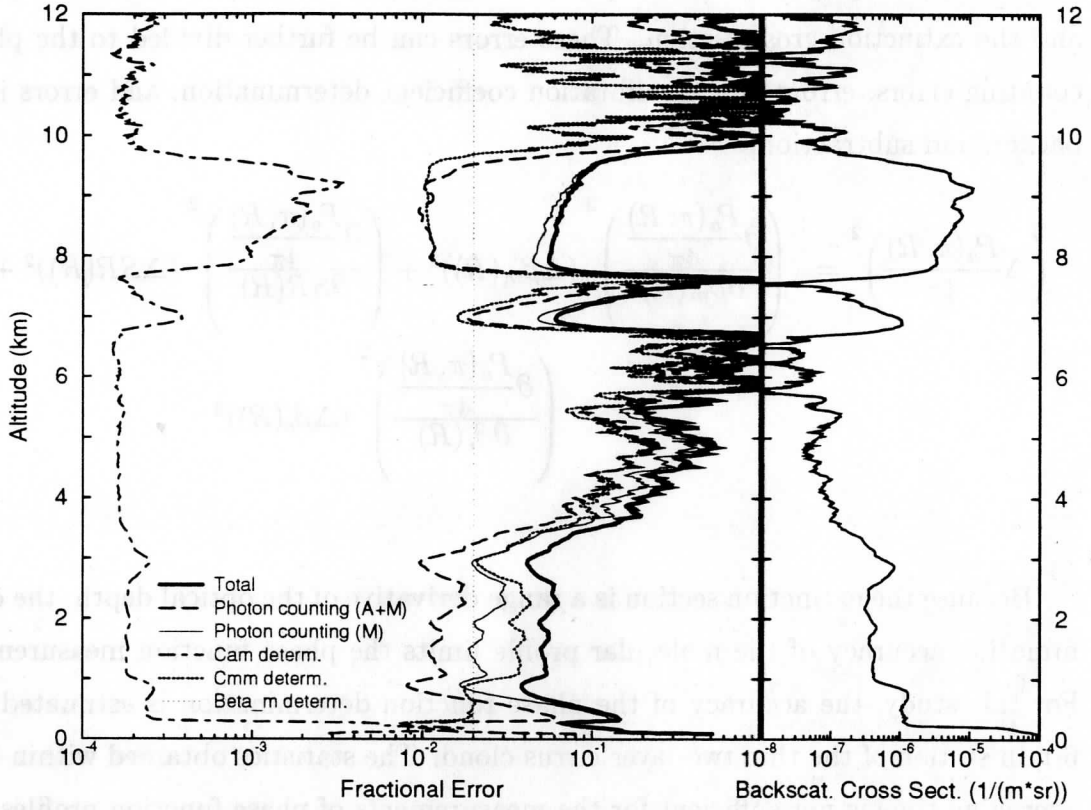

Figure 41. The effects of different errors to the aerosol backscatter cross section in case of a thin cirrus cloud (November 11, 1993, 01:05-01:08 UT). Averaging time of the data is 3 min. The aerosol backscatter profile is presented as a function of altitude (rightmost graph) and the backscatter cross section values range from $\sim 10^{-7}$ to $10^{-5} 1/m$. The aerosol backscatter cross section of the cirrus cloud (6-10 km) and the strong aerosol layer between 1 and 3.7 km can be determined with 4-10 % accuracy, but the measurements of the aerosol backscatter cross section of the clear air require a longer averaging time (leftmost graph).

The error in the phase function is affected by the errors on determinations of the molecular scattering cross section per unit volume, the aerosol and molecular profile, and the extinction cross section. These errors can be further divided to the photon counting errors, errors in the calibration coefficient determination, and errors in the background subtraction.

$$\left(\Delta\frac{P_a(\pi,R)}{4\pi}\right)^2 = \left(\frac{\partial\frac{P_a(\pi,R)}{4\pi}}{\partial\beta_m(R)}\right)^2 (\Delta\beta_m(R))^2 + \left(\frac{\partial\frac{P_a(\pi,R)}{4\pi}}{\partial SR(R)}\right)^2 (\Delta SR(R))^2 + \left(\frac{\partial\frac{P_a(\pi,R)}{4\pi}}{\partial\beta_\epsilon(R)}\right)^2 (\Delta\beta_\epsilon(R))^2 \quad (33)$$

Because the extinction section is a range derivative of the optical depth, the determination accuracy of the molecular profile limits the phase function measurements. For this study, the accuracy of the phase function determination is estimated for a 6 min section of the thin two-layer cirrus cloud. The statistics obtained within 3 min averaging time is not sufficient for the measurements of phase function profiles.

The accuracy of the phase function value determination can be seen from Figure 42. The cloud phase function can be observed with 10-20% accuracy when 6 min averaging time is used. By increasing the averaging time or the signal strength, accurate measurements of cloud phase function profiles can be made.

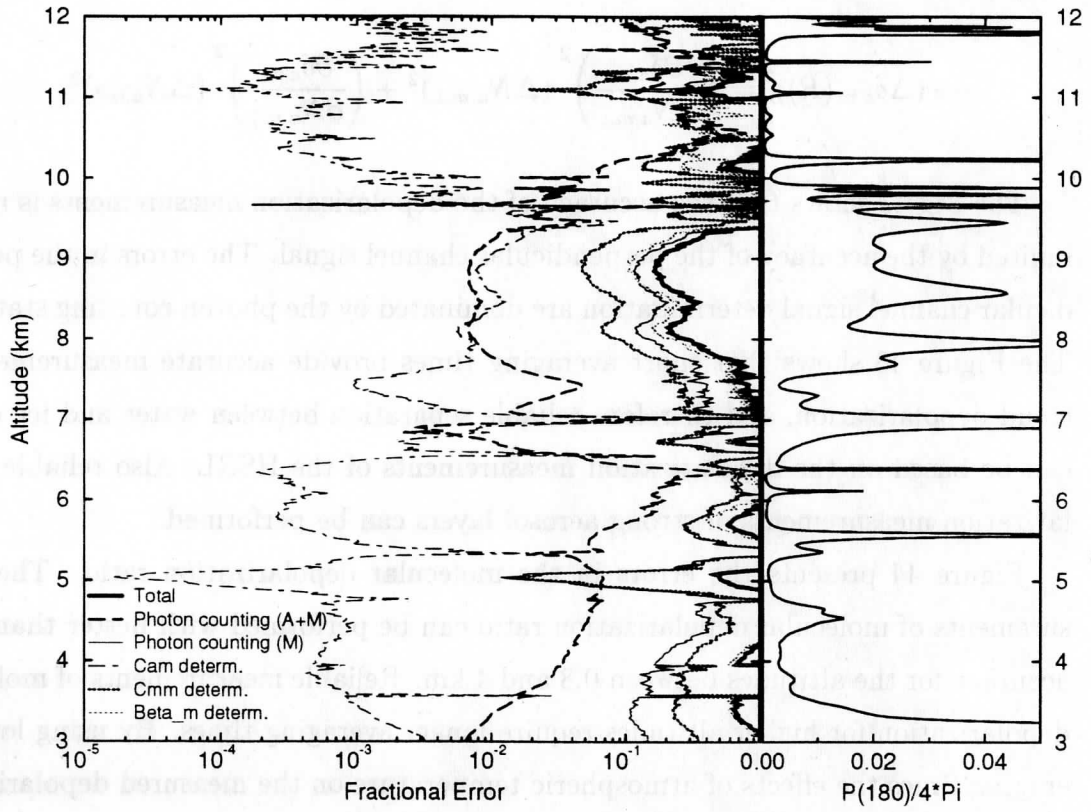

Figure 42. The effects of different errors on the phase function in case of a thin cirrus cloud (November 11, 1993, 01:05-01:11 UT). The 6 min averaging time is used. The phase function profile is presented as a function of altitude and the average phase function of the cirrus cloud layer between 7.5 and 10 km is 0.02 (rightmost graph). The accuracy of the phase function measurements is determined by the photon counting statistics, determination accuracy of the calibration coefficients, and accuracy of the molecular scattering cross section per unit volume (leftmost graph). The accuracy achieved within 6 min averaging provides phase function measurements with $\sim$ 20% accuracy for the cloud layer.

Error in the inverted depolarization ratio can be presented as a sum of errors in the parallel channel and the perpendicular channel signals.

$$(\Delta\delta_{a,m}(R))^2 = \left(\frac{\partial\delta_{a,m}}{\partial N_{a,m\perp}}\right)^2 (\Delta N_{a,m\perp})^2 + \left(\frac{\partial\delta_{a,m}}{\partial N_{a,m\parallel}}\right)^2 (\Delta N_{a,m\parallel})^2 \qquad (34)$$

The Fig 43 shows that the accuracy of the depolarization measurements is mostly limited by the accuracy of the perpendicular channel signal. The errors in the perpendicular channel signal determination are dominated by the photon counting statistics. The Figure 43 shows that short averaging times provide accurate measurements of cloud depolarization, and therefore reliable separation between water and ice clouds can be based on the depolarization measurements of the HSRL. Also reliable depolarization measurements of strong aerosol layers can be performed.

Figure 44 presents the errors in the molecular depolarization ratio. The measurements of molecular depolarization ratio can be performed with better than 10 % accuracy for the altitudes between 0.8 and 4 km. Reliable measurements of molecular depolarization for higher altitudes require longer averaging times. By using long averaging times the effects of atmospheric temperature on the measured depolarization can be studied.

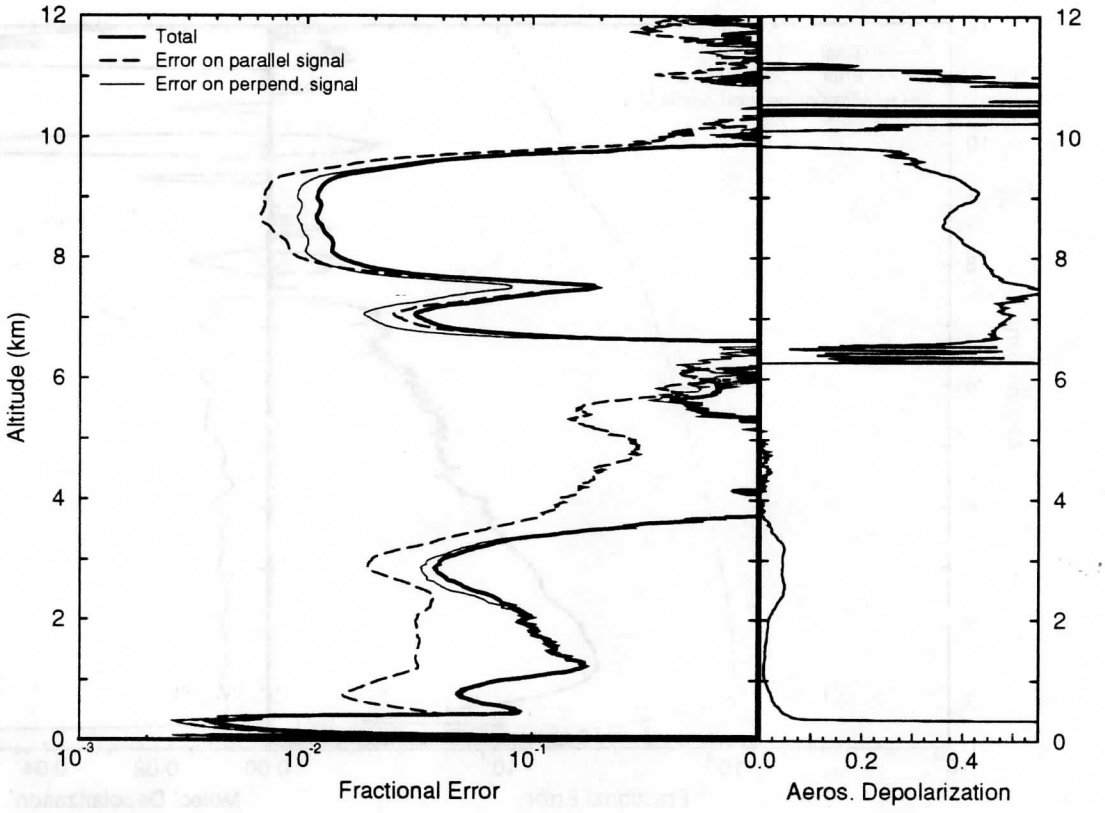

Figure 43. The effects of different errors to the inverted aerosol depolarization ratio in case of a thin cirrus cloud (November 11, 1993, 01:05-01:08 UT). Averaging time of the data is 3 min. The depolarization profile shows the variations of the inverted aerosol depolarization as a function of altitude (rightmost graph). A $\sim$ 40% cirrus cloud depolarization is observed (6.5 - 10 km) and the depolarization of the strong aerosol layer is $\sim$ 5%. The measurements of the inverted aerosol depolarization ratio are limited by the accuracy of the perpendicular signal (leftmost graph). The depolarizations of clouds can be measured with $\sim$1 % accuracy. The depolarizations of strong aerosol layers are obtained with better than 10% accuracy.

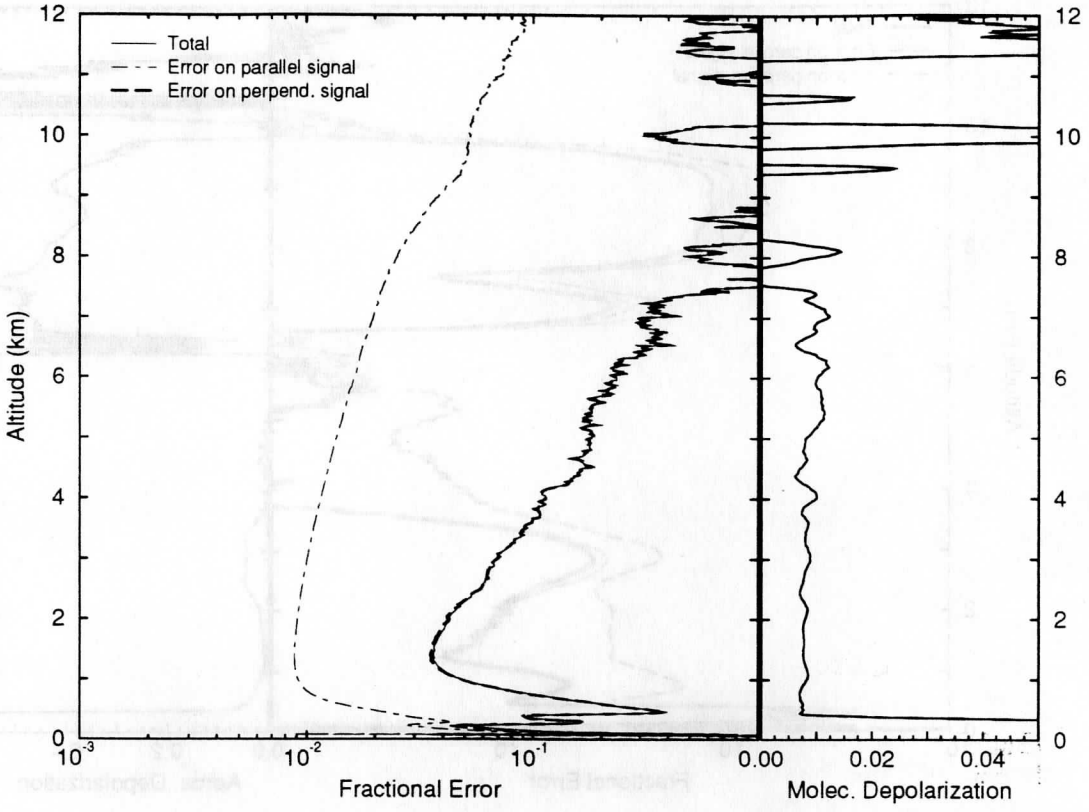

Figure 44. The effects of different errors on the inverted molecular depolarization ratio in case of a thin cirrus cloud (November 11, 1993, 01:05-01:08 UT). Averaging time of the data is 3 min. The depolarization profile shows the variations of the inverted molecular depolarization as a function of altitude (rightmost graph). A 0.8 % depolarization is observed from 0.5 to 7 km. The measurements of the molecular depolarization are limited by the accuracy of the perpendicular signal measurement (leftmost graph). For altitude between 0.8 and 4 km better than 10% accuracy is achieved. Measurements molecular depolarization for the higher altitudes require longer averaging times.

8 Conclusions

The work presented in this thesis has shown that the installation of the iodine absorption filter has substantially improved the performance of the University of Wisconsin-Madison High Spectral Resolution lidar (HSRL). The new system design that includes the iodine absorption filter, polarization, and multiple scattering measurement capabilities is shown. The high resolution etalon, that was used in the earlier system to separate between aerosol and molecular scattering, provided only 1:2 separation for the aerosol backscatter signal between channels. The iodine absorption filter has been shown to suppress the aerosol backscatter signal on molecular channel down to 0.08% and therefore the aerosol cross talk signal on the molecular signal can be easily removed even for optically thick clouds. In the etalon based system, the determination of the system calibration terms was sufficient to provide accurate inversions only for the clear air aerosols and thin cirrus clouds. The use of the iodine absorption filter has also improved the robustness of the HSRL, reduced the complexity of the system, and increased the optical transmission of the system, so that accurate measurements of the optical depth, backscatter cross section and phase function can be made. Also the simultaneous measurements of depolarization and multiple scattering are performed. The HSRL implementation shows a depolarization measurement technique that uses the one transmitter laser and one detector to measure both polarization components. Therefore, no calibration of the receiver is required. The multiple scattering measurements are realized with a separate channel that allows measurements of signal strength variations as function of field of view simultaneously with the measurements of the narrow field of view channels.

The iodine absorption filter provides an absolute wavelength reference for the HSRL measurements. The iodine absorption line observed through a cell with 50% transmission on the line center is used for the wavelength locking of the HSRL transmitter laser. This provides stable operation over a long period of time without a need for frequent calibrations. Measurements have shown that the laser wavelength is maintained within $\pm$ 0.052 pm.

The stability and reliability of the system have been tested by operating the iodine absorption based HSRL at the University of Wisconsin-Madison campus. Start-

ing from July 1993, the HSRL has been routinely operated and data from different atmospheric conditions have been recorded. This dataset contains $\sim$ 30 cirrus cloud cases. The measurements show that accurate measurements of optical properties of the atmosphere can be performed. The improved measurement accuracy has made possible to measure optical depth profiles inside the clouds. The current HSRL can be used to probe clouds that have optical depths up to $\sim$ 3. This means that most of the cirrus cloud cases can be fully observed and the bases of thick water clouds can be measured up to 300–500 m inside the cloud. This has been achieved by using the iodine absorption filter, high laser pulse repetition rate, small pulse energy per laser pulse, and very fast photon counting data system. The measurement accuracy of the HSRL is high enough to provide accurate measurements of optical parameters of clouds and strong clear air aerosol layers within 3 min averaging time, but the accurate measurements of clear air optical parameters require longer averaging times. The clear air optical parameters can be measured up to 35 km. The error analysis shows that accuracy of the HSRL measurements is mostly limited by the photon counting statistics. The system performance can be increased by increasing the system detection efficiency or/and increasing the transmitted laser power. The greatest improvement would be a photodetector with higher quantum efficiency and faster count rate capability.

The depolarization data obtained by the HSRL shows the ability of the HSRL to distinguish between water and ice clouds. It is shown, that the 160μrad field of view of the spectrometer channels effectively suppresses the multiple scattering effects on the measured depolarization ratio. Therefore, a reliable separation between water and ice clouds is possible. The HSRL measurements have shown, that traditional systems with 1–5 mrad field of views cannot reliably separate between water and ice, because the depolarization observed with a 1 mrad field of view is comparable to the ice depolarization within a small penetration depth from the water cloud base due to the multiple scattering. The error analysis shows, that the depolarization of the clear air aerosol layers can be observed with better than 10 % accuracy. The accuracy of the cloud depolarization measurements is better than 1 %. The measurements of depolarizations of weak aerosol layers and molecular backscatterer are limited by the

photon counting statistics.

The study of the cloud depolarizations between August 2 and November 11, 1993 shows that in 45 % of cirrus cloud cases simultaneous observations of supercooled water at cirrus cloud altitudes were made. The average cirrus cloud depolarization is shown to increase from 33% at -5°C temperature to 41% at -60°C. The observed behavior is different than observed by Platt *et al.*[43]. The depolarization observed by Platt *et al.* ranged from ~15% to ~40% between temperatures from -10 to -60 °C. The largest difference between the HSRL measurements and Platt's measurements is observed for the temperature range from -30 to -10 °C, where Platt observed low cirrus cloud depolarizations. The low values of depolarization in Platt's measurement are most probably caused by multiple scattering from supercooled water droplets, because the system used for this measurement had a 2.5 mrad field of view. The HSRL measurements show that supercooled water clouds have been found at temperatures as low as -40°C and pure water clouds have been found at temperatures above 0°C. No water has been found at temperatures below -40°C and the presence of cirrus disappears at temperatures above 0°C. In the HSRL measurements, the cirrus cloud depolarization ratios for all temperatures are close to the values observed for the temperatures without supercooled water clouds. The small difference in the observed depolarization as a function of temperature may be a result of different shapes, sizes, and orientations of the ice crystals at different temperatures.

The depolarization of the molecular backscatter is ~0.7–0.8%, when measured without the low resolution etalons. When the low resolution etalons are used, a ~0.55–0.6% depolarization is measured. The depolarization measured for the signal from the Cabannes line and the rotational Raman lines is 1.5 % without any spectral filters. The measured molecular depolarization value is larger than the expected 0.4 % depolarization of Cabannes line. The system filter bandpass admits a small fraction of the rotational Raman lines and blocks part of the Cabannes line and therefore an increase on the depolarization ratio is observed due to the presence of the highly depolarized rotational Raman lines. The model calculation for the depolarization transmission of the system show, that a 0.56 –0.62 % depolarization is expected for the case where no low resolution etalons were used. A 0.402 –0.425 % depolarization

is expected, when one or two etalon are used. The depolarization observed with the HSRL are larger than the expected values. The cause of the small difference between expected and measured depolarization values is currently unknown. The further analysis of the depolarization measurement accuracy of the HSRL requires an advanced study of effects of the iodine spectrum and rotational Raman lines to the depolarization.

The HSRL measurements require a knowledge of the atmospheric temperature profile. The atmospheric temperature profile measured with the HSRL shows that the HSRL can be used to measure temperature with a high enough accuracy so that the measured temperature profiles can be used for the analysis of the HSRL data. Therefore, the requirement for radiosonde measurements of atmospheric temperature could be eliminated. Before the temperature measurements with the HSRL can be routinely performed, the effects of aerosol backscatter signal to the molecular transmission of the iodine absorption filter have to be removed.

This study has provided an instrument basis for a design of a simple and robust lidar for the measurements of the optical properties of the atmosphere. The University of Wisconsin HSRL provides a unique instrument for the measurements of the cloud optical properties and the data measured with the HSRL provides useful information that can be used for the climate models that study the effects of clouds to the earths atmosphere.

References

[1] Stephens, G. L. and P. J. Webster, "Clouds and climate: Sensitivity of simple systems," *J. Atm. Sci.*, **39**, 235–247, 1981.

[2] Liou, K.-N., "Influence of cirrus clouds on weather and climate processes: A global perspective," Monthly Weather Review, **114**, 1167–1192, 1986.

[3] Ansmann, A., U. Wandinger, M. Riebesell, C. Weitkamp, and W. Michaelis, "Independent measurements of extinction and backscatter profiles in cirrus clouds by using a combined Raman elastic-backscatter lidar," *Appl. Opt.* , **31**, 7113–7131, 1992.

[4] Whiteman, D. N., S. H. Melfi, and R. A. Ferrare, "Raman lidar system for the measurements of water vapor and aerosols in the Earth's atmosphere," *Appl. Opt.* , **31**, 3068–3082, 1992.

[5] Fiocco, G. and J. B. DeWolf, "Frequency spectrum of laser echoes from atmospheric constituents and determination of aerosol content of air," *J. Atm. Sci.*, **25**, 488–496, 1968.

[6] Schwiesow, R. L. and L. Lading, "Temperature profiling by Rayleigh-scattering lidar," *Appl. Opt.* , **20**, 1972–1979, 1972.

[7] Shipley, S. T., J. H. Joseph, J. T. Trauger, P. J. Guetter, E. W. Eloranta, J. E. Lawler, W. J. Wiscombe, A. P. Odell, F. L. Roesler, J. A. Weinman, "The evaluation of a shuttle borne lidar experiment to measure the global distribution of aerosols and their effect on the atmospheric heat budget," Final report on NASA grant NSG 1057, 1975 pp. 150.

[8] Shipley, S. T., D.H. Tracy, E. W. Eloranta, J. T. Trauger, J. T. Sroga, F. L. Roesler, and J. A.Weinman, "High resolution lidar to measure optical scattering properties of atmospheric aerosols. 1: Theory and instrumentation," *Appl. Opt.* **22**, 3716–3724, 1983.

[9] Sroga, J. T., E. W. Eloranta, S. T. Shipley, "F. L. Roesler, and P. J. Tryon, High spectral resolution lidar to measure optical scattering properties of atmospheric aerosols. 2: Calibration and data analysis," *Appl. Opt.* , 22, 3725–3732, 1983.

[10] Grund, C. J., "Measurement of cirrus cloud optical properties by high spectral resolution lidar," Ph.D. Thesis, Department of Meteorology, University of Wisconsin-Madison, 1987.

[11] Grund, C. J., E. W. Eloranta, "Fiber-optics scrambler reduses the bandpass range dependence of Fabry-Perot etalons used for spectral analysis of lidar backscatterer," *Appl. Opt.* **30**, 2668, 1991.

[12] Grund, C. J. and E. W.Eloranta, "University of Wisconsin High Spectral Resolution Lidar," *Optical Engineering*, **30**, 6–12, 1991.

[13] Eloranta, E. W. and P. K. Piironen, "Adaptation of the University of Wisconsin High Resolution Lidar for polarization and multiple scattering measurements," Sixteenth International Laser Radar Conference, Cambridge, Massachusetts, July 20-24, 1992, NASA Conference Publication 3158, 353–356, 1992.

[14] Shimizu, H., S. A. Lee, and C. Y. She, "High spectral resolution lidar system with atomic blocking filters for measuring atmospheric parameters," *Appl. Opt.* **22**, 1373–1391, 1983.

[15] She, C. Y., R. J. Alvarez II, L. M. Caldwell, and D. A. Krueger, "High-spectral-resolution Rayleigh-Mie lidar measurements of aerosol and atmospheric profiles," Opt. Lett. **17**, 541–543, 1992.

[16] Alvarez, R. J. II, L. M. Caldwell, P. G. Wolyn, D. A. Krueger, T. B. McKee, and C. Y. She, "Profiling temperature, pressure, and aerosol properties using a high spectral resolution lidar employing atomic blocking filters," *J. Atm. Ocean. Techn.* **10**, 546–556, 1993.

[17] Krueger, D. A., L. M. Caldwell, R. J. Alvarez II, and C. Y She, "Self-consistent method of determining vertical profiles of aerosol and atmospheric properties using a high spectral resolution Rayleigh-Mie lidar," *J. Atm. Ocean. Techn.* **10**, 533–545, 1993.

[18] Gerstenkorn, S. and P. Luc, *Atlas du spectre d'absorption de la molecule d'iode* (Centre National de la Recherche Scientifigue, Paris, 1978).

[19] Harrison, J. A., M. Zahedi, and J. W. Nibler, "Use of seeded Nd:YAG lasers for high-resolution spectroscopy," Opt. Lett. **18**, 149–151, 1993.

[20] Liao, K. H. and R. Gupta, "I_2 vapor cell as narrow band optical filter," *Rev. Sci. Instr.*, **49**, 867–869, 1978.

[21] Miles, R. B., J. N. Forkey, and W. R. Lempert, "Filtered Rayleigh Scattering measurements of supersonic/hypersonic facilities," AIAA 17th Aerospace Ground Testing Conference, July 6-8, 1992, Nashville, TN (USA).

[22] Piironen, P. and E. W. Eloranta, "Demonstration of a high spectral resolution lidar based on an iodine absorption filter," Opt. Lett. bf 19, 234–236, 1994.

[23] Klett, J. D., "Stable analytical inversion solution for processing lidar returns," *Appl. Opt.* **20**, 211–220, 1981.

[24] Hinkley, E. D. (editor), "Laser Monitoring of the Atmosphere," Springer-Verlag, New York, 1976.

[25] Eloranta, E. W. "Calculation of doubly scattered lidar returns," Ph. D. Thesis, Department of Meteorology, University of Wisconsin, 1972.

[26] Eloranta, E. W., "A practical model for the calculation of multiply scattered lidar returns," Optical Society of America, Remote Sensing of the Atmosphere, Topical Meeting, Salt Lake City, Utah, March 8-12, 1993, pp. ThE20-1.

[27] Eloranta, E. W. and S. T. Shipley, "A solution for multiple scattering," *in Atmospheric Aerosols: Their Formation, Optical Properties, and Effects*, Spectrum Press, Hampton, Virginia, 1982.

[28] *Model S100 Injection Seeding System*, Lightwave Electronics Corporation, California, USA, 1989.

[29] Grund, C. J., F. L. Roesler, and E. W. Eloranta, "Thermally induced spectral drift cancellation in pressure-tuned Fabry-Perot etalons," *Appl. Opt.* , **27**, 662–663, 1988.

[30] Sroga, J. F., "Remote measurerements of aerosol scattering properties by an airborne high spectral resolution lidar," Ph. D. Thesis, University of Wisconsin-Madison, 1983.

[31] *How to perform photon counting using photomultiplier tubes*, Hamamatsu, Technical Information, No. ET-06/Feb 1990.

[32] *TRC thermodynamic tables (Non-hydrocarbons)*, (College Station, Tex. : Thermodynamics Research Center, Texas A & M University, 1986), pp. k-190, ka-190.

[33] Arie, A. and R. L. Byer, "Laser heterodyne spectroscopy of $^{127}I_2$ hyperfine structure near 532 nm," *J. Opt. Soc. Am. B.*, **10**, 1990–1997, 1993.

[34] Yip, S. and M. Nelking, "Application of kinetic model to time-dependent density correlations in fluids," *Physical Review*, **135**, A1241–A1247, 1964.

[35] Arie, A. and R. L. Byer, "Frequency stabilization of the 1064-nm Nd:YAG lasers to Doppler-broadened lines of iodine," *Appl. Opt.* , **32**, 7382–7386, 1993.

[36] Scotland, R. M., K. Sassen, and R. Stone, "Observations by lidar of linear depolarizations of hydrometeors," *J. Appl. Meteor.*, **10**, 1011–1017, 1971.

[37] Sassen, K. "The polarization lidar technique for cloud research: a review and current assessment," *Bull. Am. Meteor. Soc.*, **72**, 1848–1866, 1991.

[38] Pal, S. R. and A. I. Carswell, "Polarization properties of lidar backscattering from clouds," *Appl. Opt.* , **12**, 1530–1535, 1973.

[39] Rowell, R. L. and G. M. Aval, "Rayleigh-Raman depolarization of laser light scattered by gases," *J. Chem. Phys.*, **54**, 1960–1964, 1971.

[40] Young, A. T., "Rayleigh scattering," *Physics Today*, January 1982, 42–48, 1982.

[41] Liou, K.-N. and H. Lahore, "Laser sensing of cloud composition: a backscatter depolarization technique," *J. Appl. Meteor.*, **13** 257–263, 1974.

[42] Kumai, M., "Formation of ice crystals and dissipation of supercooled fog by artificial nucleation, and variations of crystal habit at early growth stages," *J. Appl. Meteor.*, **21**, 579–587, 1982.

[43] Platt, C. M. R., J. C. Scott, and A. C. Dilley, "Remote sensing of high clouds. Part VI: Optical properties of midlatitude and tropical cirrus," *J. Atm. Sci.* **44**, 729–747, 1987.

[44] Strauch, R. G., V. E. Derr, and R. E. Cupp, "Atmospheric temperature measurement using Raman backscatter," *Appl. Opt.* , **10**, 2665–2669, 1971.

[45] Cooney, J., "Measurements of atmospheric temperature profiles by Raman backscatter" *J. of Appl. Meteor.*, **11**, 108–112, 1972.

[46] Kalshoven, J. E., Jr., C. L. Korb, G. K. Schemmer, and M. Dombrowski, "Laser remote sensing of atmospheric temperature by observing resonant absorption of oxygen," *Appl. Opt.* , **20**, 1967–1971, 1981.

[47] Endemann, M. and R. L. Byer, "Simultaneous measurements of atmospheric temperature and humidity using a continously tunable IR lidar," *Appl. Opt.* , **20**, 3211–3217, 1981.

[48] P. Keckhut, A. Hauchecorne, and M. L. Chanin, "A critical review of the database acquired for the long-term surveillance of the middle atmosphere of the French Rayleigh lidars," *J. Atm. Ocean. Techn.*, **10**, 850–867, 1993.

[49] Heymsfield, A. J., "Precipitation development in statiform ice clouds: A microphysical and dynamical study," *J. Atm. Sci.*, **34**, 367–381, 1977.